12-2014

Nonequilibrium transport of ionic liquids in electrified nanosystems

Xikai Jiang
Clemson University, jxk28@msn.com

Recommended Citation

NONEQUILIBRIUM TRANSPORT OF IONIC LIQUIDS IN
ELECTRIFIED NANOSYSTEMS

A Dissertation
Presented to
the Graduate School of
Clemson University

In Partial Fulfillment
of the Requirements for the Degree
Doctor of Philosophy
Mechanical Engineering

by
Xikai Jiang
December 2014

Accepted by:
Dr. Richard Miller, Committee Chair
Dr. Rui Qiao, Co-chair
Dr. Gang Li
Dr. Pingshan Wang

ABSTRACT

Room-temperature ionic liquids (RTILs) are a promising class of electrolyte that are composed entirely of ions but are liquid at room temperature. Their remarkable properties such as wide electrochemical window make them ideal electrolytes in many electrochemical systems. Because the non-equilibrium transport of RTILs often determines the performance of these systems, a fundamental understanding of such transport is needed. Here, using molecular dynamic (MD) and continuum simulations, we investigated the non-equilibrium transport of RTILs in three scenarios relevant to the application of RTILs in electrochemical systems: the electroosmotic flow (EOF) of RTILs through nanochannels, the electrokinetic transport of RTILs through nanopores, and the charging kinetics of the double layers near planar electrodes.

For EOFs of RTILs through nanochannels, we discovered that their strength greatly exceeds that predicted by the classical hydrodynamic theories. We traced the unexpected flow strength to the short-wavelength nature of the EOFs in RTILs, which requires the generalized hydrodynamics (i.e., nonlocal law for the shear stress-strain rate relation) for describing such flows. The EOF in RTILs is thus a rare example in which short-wavelength hydrodynamics profoundly affects flow measurables.

For the electrokinetic transport of RTILs through nanopores, we discovered that, in pores wetted by RTILs a gradual dewetting transition occurs upon increasing the applied voltage, which is accompanied by a sharp increase in ionic current. These phenomena originate from the solvent-free nature of RTILs and are in stark contrast with

ii

the transport of conventional electrolytes through nanopores. Amplification of these phenomena is possible by controlling the properties of the pore and RTILs, and we showed that it is especially pronounced in charged nanopores.

For the charging kinetics of the double layers near planar electrodes, we found that, the potential across the double layers can oscillate during charging when the charging current is large. Such oscillation originates from the sequential growth of the ionic space charge layers near the electrode surface. This allows the evolution of double layers in RTILs with time, an atomistic process difficult to visualize experimentally, to be studied by analyzing the cell potential under constant current charging conditions.

DEDICATION

This dissertation is dedicated to my wife, parents, and grandparents.

ACKNOWLEDGEMENTS

TABLE OF CONTENTS

LIST OF FIGURES

LIST OF FIGURES (CONTINUED)

LIST OF FIGURES (CONTINUED)

LIST OF FIGURES (CONTINUED)

CHAPTER 1

Introduction

1.1 Overview

The increasing global demands for green energy require novel energy solutions. Such growing demands triggered tremendous developments of energy technologies in the recent decades. At present, solar[1], wind[2] and ocean wave[3] energies are harvested at very large scales and converted to electricity[4]. Since these renewable energy sources are often intermittent, effectively using these energy sources often demands reliable energy storage technologies. A large variety of electrical energy storage systems, e.g., fuel cells[5], lithium-ion batteries[6], lithium-air batteries[7] and supercapacitors[8] have been developed to meet this requirement[9]. For example, Figure 1.1 shows the schematics of a supercapacitor, which is capable of delivering large amount of energy in very short time and thus can be used for load regulation (e.g., power "shaving") in power grids.

The performance of electrochemical energy storage systems often depends strongly on the transport characteristics of their electrolytes. The transport characteristics of conventional electrolytes, such as aqueous solutions of KCl, NaCl and $CaCl_2$ have been studied extensively and are relatively well understood[10,11]. Recently, room-temperature ionic liquids (RTILs) have received significant attention as a new class of electrolyte for electrochemical energy storage devices[12,13]. RTILs are low temperature molten salts composed entirely of ions. Because ions in RTILs are usually bulky and their charges are de-localized (see Figure 1.2), the electrostatic interactions between ions are not as strong compared to that in conventional electrolytes. This, along with the fact that the complex shape of ions makes highly ordered packing of ions difficult,

allows RTILs to be in the liquid state at close to room-temperature. RTILs are considered designer molecules because it is relatively easy to tailor their properties by modifying their chemical structures. Because RTILs have remarkable properties such as wide electrochemical window, low vapor pressure, and excellent thermal stability, they are well-suited for electrochemical energy storage devices such as batteries and supercapacitors. For example, the wide electrochemical window of RTILs enables supercapacitors to operate at voltages (~4-5V) much higher than that of conventional electrolytes (1-3V), which helps greatly increase supercapacitors' energy density.
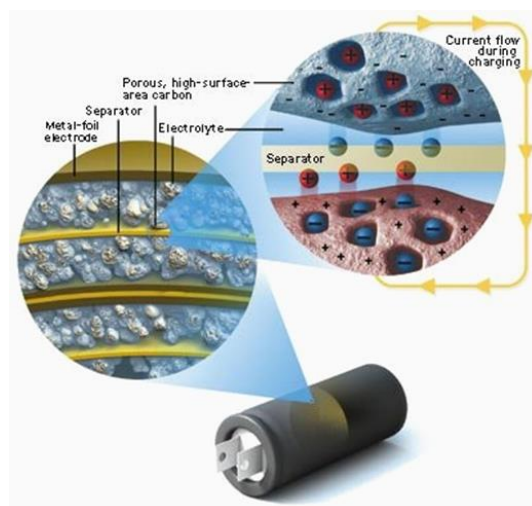
Figure 1.1. Schematics of a supercapacitor and its key components (porous electrodes, electrolytes, and separator)[14]. The structure/size of the nanopores, the interaction between ions and pore walls, and the operating voltage together determine the maximal energy density of the supercapacitors; the transport of ions in the bulk electrolytes and in the nanoporous electrode determine the power density of the supercapacitor.

In this dissertation, we are most interested in the non-equilibrium transport of RTILs in electrochemical systems, such as ionic transport in nanochannels and nanopores, because the performance of these systems is often determined by the non-equilibrium ion transport at

Figure 1.2. Room-temperature ionic liquids (RTILs). Ions in RTILs are often bulky, have complex shape, and feature de-localized charge. Because there exists many types of cations and anions capable of forming RTILs and these ions can be further modified by functionalization, RTILs are considered designer molecules. Left panel: the molecular structure and charge distribution of a popular RTIL 1-Butyl-3-methylimidazolium hexafluorophosphate (BMIM-PF$_6$)[15]. Right panel: different types of RTILs showing different colors[16].

nanoscale[17]. For example, the transport of ions through nanopores within the porous electrode of supercapacitors determines the dynamics of charging/discharging of these nanopores, and ultimately the power density of the supercapacitors[18]. In the following sections, we review the basic theories and prior works on transport of ions and electrolytes in nanoscale systems, with a focus on the non-equilibrium transport. Since the electrical double layers (EDLs) play an essential role in the ionic transport in nanoscale systems, we will first introduce the concept of EDLs.

1.2 Electrical double layers

Electrical double layers (EDLs) are ubiquitous in electrochemical systems. They usually emerge when electrified surfaces come into contact with another phase featuring mobile charge

carriers[1]. Because of their importance in diverse applications including electrode kinetics, colloidal stability, and manipulation of fluids/particulates in micro/nanofluidic systems, numerous models have been developed to describe EDLs (see Figure 1.3). In this dissertation, we are interested in the EDLs formed at the interface of an electrified solid surface and electrolytes in the liquid state. The Helmholtz model is the simplest model for such EDLs. In this model, the electrical charges on the solid surface are assumed to be balanced by a single layer of counter-ions adsorbed on the solid surface (see Figure 1.3a). While such a model can explain some experimental data (e.g., those related to electrode kinetics), it fails to explain most of the electrokinetic experimental data. A key reason for this is that, at finite temperature, not all counter-ions are adsorbed on the charged surface due to thermal fluctuations. As such, the counter-ions do not form a single static layer but rather occupy a finite space near the charged surface, usually referred to as the diffuse layer (see Figure 1.3b). This picture of the EDLs was originally proposed by Gouy and Chapman, and had since become the cornerstone of electrokinetic theories.

The picture of the EDLs proposed by Gouy and Chapman can be described quantitatively using the Poisson-Boltzmann (PB) equation. The PB equation is a mean-field theory, in which the free energy of an ion i at position r is taken as the product of the mean electrical potential at that position and the charge of the ion. Since the distribution of ions in liquid state is governed by Boltzmann statistics, it follows that the density of ion i at position r is given by

---

[1] A surface can become electrified due to polarization by external voltages (as in the case of electrodes) or by other electrochemical means, e.g., due to deprotonation of surface groups or specific adsorption of ions onto surfaces. The mobile charge carriers can be ions, electrons, or holes, depending on the nature of the phase they exist. In this dissertation, the mobile charge carriers are ions.

$$n_i(r) = n_{i,\infty} e^{-e\phi(r)z_i/k_B T} \tag{1.1}$$

where $n_{i,\infty}$ is the density of ion i in bulk electrolyte (where the electrical potential is taken as zero), $\phi(r)$ is the mean-field electrical potential at position r, z_i is the valency of ion i, e is the electron charge, k_B is the Boltzmann constant, and T is the temperature. By combining Equation 1.1 with the Poisson equation for the electrical potential distribution, we arrive at the classical PB equation

$$\nabla^2 \phi = -\frac{e}{\epsilon} \sum_{i=1}^{N} z_i n_{i,\infty} e^{-z_i \phi e/k_B T} \tag{1.2}$$

where ϵ is the dielectric permittivity inside the EDLs. Solving the PB equation can provide all details of the EDLs, e.g., the distribution of the electrical potential and ion densities across the EDLs. In the above derivation, ions are taken as point charges, and thus they can approach
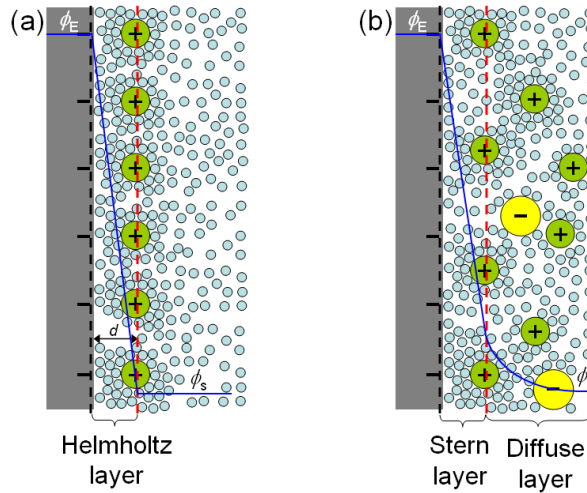
Figure 1.3. Classical models of electrical double layers. (a) The Helmholtz model. In this model, the charge on the surface is screened by one layer of counter-ions, and the electrical potential drops linearly within the EDLs. (b) The Gouy-Chapman-Stern model. In this model, the ions can approach to the electrified surface to a finite distance. The charge on the surface is screened by adsorbed ions and ions within the diffuse layer. The electrical potential drops linearly within the ion-free Stern layer and nonlinearly within the diffuse layer. Figures are reproduced from Ref. 19.

infinitely close to the charged surface. Near surface with large surface charge densities (or high potential), the PB equation often predicts unphysically high ion density (e.g., ion density far exceeds the close packing limits defined by ion sizes). This issue can be resolved by setting the closest approach of ions to the surface to a finite value (typically equal to the diameter of an ion or a hydrated ion). Since this idea was first articulated by Stern, the ion-free layer adjacent to the charged surface is usually called the Stern layer.

It can be shown that the thickness of the diffuse layer in the EDLs is closely related to the so-called Debye length

$$\lambda_D = \sqrt{\frac{\varepsilon k_B T}{\sum_i n_{i,\infty} z_i^2 e^2}} \qquad (1.3)$$

Since the Debye length depends on the concentration of the bulk electrolyte, it can be considered as an intrinsic length of the electrolyte. Physically, it characterizes the distance over which the charges on electrode surface are screened by ions near them. Near surface with potential smaller than the thermal voltage ($\phi_{thermal} = k_B T / e \approx 26 mV$ at room temperature), the electrical potential drop follows $(z) = \phi(0)e^{-z/\lambda_D}$. Clearly, the Debye length dictates how fast the potential drops and it quantitatively characterizes the EDLs thickness. While the Debye length does not characterize the thickness of EDLs when the potential drop inside the diffuse layer is much larger than the thermal voltage, it can still serve as a useful indication of the extension of the EDLs.

Although the PB equation has numerous limitations (e.g., it neglects the finite size of ions, ion-ion correlations, and non-electrostatic ion-ion and ion-wall interactions), it has been used successfully to interpret experimental phenomena related to electrokinetics, interactions

between colloidal particles and electrode kinetics. Despite these successes, we must emphasize that the PB equation and most of its extensions are essentially based on dilute solution theories and they are rigorously valid only when the electrical potential drop across EDLs is not much larger than the thermal voltage. We must be cautious when attempting to use them in situations with high electrolyte densities or large potential drop across EDLs.
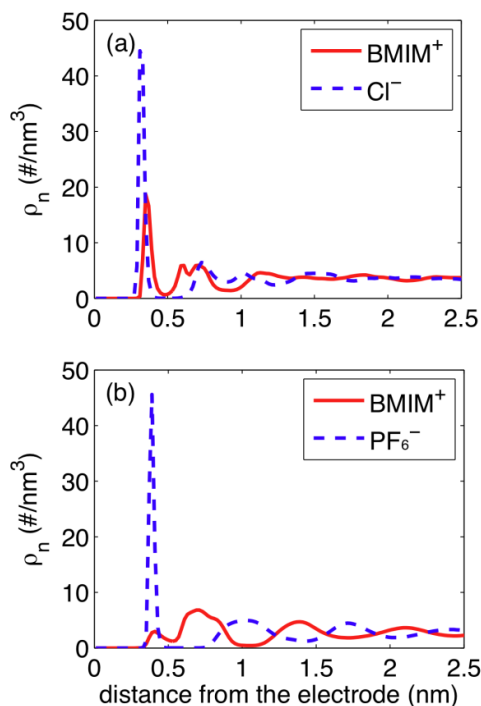
Figure 1.4. Structure of EDLs in RTILs revealed by MD simulations. Distribution of cations and anions near a planar electrode with a surface charge density of 0.112 C/m^2. The RTIL is [BMIM][Cl] in panel a and [BMIM][PF$_6$] in panel b. Figures are reproduced from Reference 20.

RTILs are solvent-free electrolytes and ions in them are in close contact. Clearly, the foundation of the PB equation breaks down for the EDLs in RTILs. Because of this, there has been tremendous interest in delineating the structure of the EDLs in RTILs in the past six years. Research in this direction is, in large part, triggered by a highly influential paper published by Professor Alexei Kornyshev (Imperial College London) titled "Double-Layer in Ionic Liquids:

Paradigm Change?"[21] While earlier experimental data suggested that EDLs in RTILs can be described well by the Helmholtz model, such a simplistic picture seems to be inadequate based on recent experimental, theoretical and simulation works. Specifically, numerous simulations and experimental measurements showed that EDLs in RTILs are characterized by an alternating layering of counter-ions and co-ions near the charged surface (see Figure 1.4) and such layering can extend a few nanometers from the charged surface.[22,23,24,25,26,27,28,29,30,31,32,33,34,35,36]
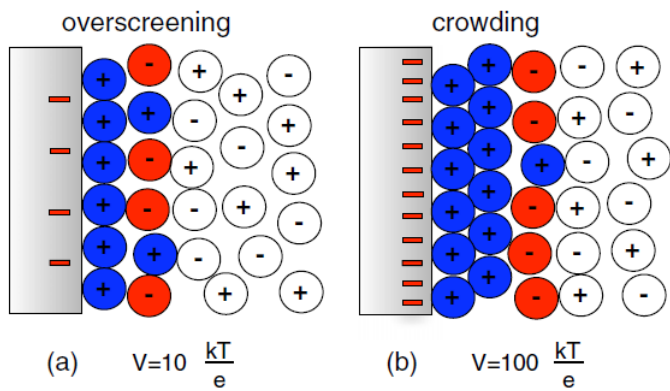
Figure 1.5. Structure of EDLs in RTILs at different surface potentials. Overscreening (a) is observed at low surface potential, while crowding is observed at very high surface potentials (b).

A key feature of the EDLs in RTILs is the so-called overscreening phenomenon. In the classical PB equation and its variants, the charge on the surface is screened monotonically as one moves away from the surface, i.e., at any position inside EDLs, the net ionic space charge between the surface and this position is always smaller (or at best equal) to the net charge on surface. If the overscreening phenomenon occurs, the net ionic space charge density at a finite distance away from the surface exceeds the total charge on the surface (see Figure 1.5a). It has been found that the overscreening phenomenon is more distinct at low surface charge densities (or low surface potentials) and becomes weaker as the surface becomes more polarized[37].
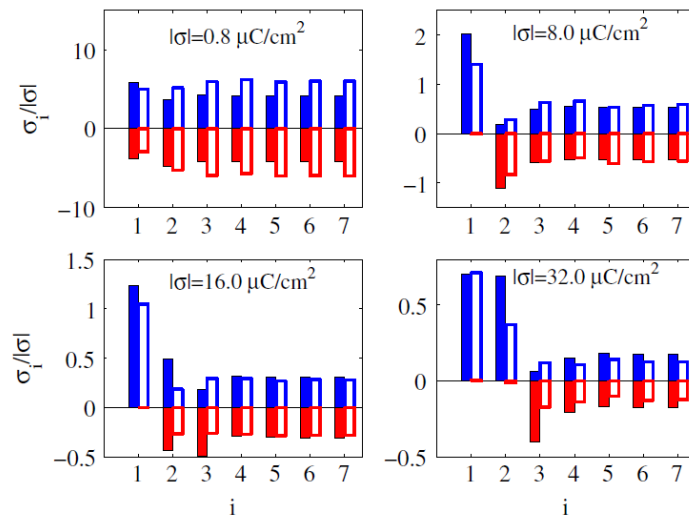
Figure 1.6. Structure of EDLs computed using MD simulations (solid bars) and the BSK model (open bars). The RTIL has counter-ions and co-ions with the same size (ion diameters ~1.0nm). Distributions of cations (top panels) and anions (bottom panels) are plotted in monolayer bins $i =1; \ 2; \ . . .$ for different surface charge densities. Figures are reproduced from Ref. 39.

Another interesting feature of the EDLs in RTIL is the crowding (also called lattice satuation[21]) phenomenon. This phenomenon occurs when the net charge on the surface is so high that the first counter-ion layer adsorbed on the surface cannot fully screen these charges. This phenomenon can occur because the ions in RTILs are often bulky. For example, for a counter-ion diameter of ~0.8nm (similar to the size of a BMIM+ ion), the maximal charge screened by a single layer of counter-ions near the surface is ~0.35 C/m^2. Since the charge density of surfaces in electrochemical systems can often exceed this value, crowding is indeed expected. It is worth noting that overscreening can still occur when crowding occurs, although these two phenomena are often treated as if they are mutually exclusive (e.g., the terminology of transition from over-screening to crowding that is frequently used in the literature). For example, the bottom right panel of Figure 1.6 shows that, at a surface charge density of 0.32C/m^2, the first layer of counter-ions (diameter: ~1.0nm) adjacent to the electrode cannot fully screen the charge on the surface,

9

i.e., crowding appears. However, the net charge in the first and second ionic layers exceeds that on the electrode surface. Since there is no co-ion in the first two ionic layers, it is clear that overscreening occurs in the second ionic layer.

Many models have been developed to predict the structure and thermodynamic properties of the EDLs in RTILs. Most of these models are mean-field models, and they can be considered as extensions of the PB model, usually by taking into account the finite size of the ions and the compressibility of the RTILs[21]. While these models can predict some aspects of the EDLs, in particular how the capacitance of EDLs depends on the voltage, they have inherent limitations, e.g., none of them can predict key features such as the overscreening phenomenon. Most recently, however, a non-mean field model that differ qualitatively from these models have been developed by Professors Bazant (MIT), Storey (Olin College), and Kornyshev (Imperial College) [37]. The key idea is to account for the ion-ion correlations by introducing a wavelength-dependent dielectric constant. For equilibrium EDLs, the electrical potential distribution inside the EDL is given by

$$\left(1 - \delta_c^2 \widetilde{\nabla}^2\right) \widetilde{\nabla}^2 \tilde{\phi} = \frac{\sinh \tilde{\phi}}{1 + 2\gamma \sinh^2(\tilde{\phi}/2)} \tag{1.4}$$

where dimensionless correlation length is $\delta_c = l_c/\lambda_D$, l_c is electrostatic correlation length, γ is the ratio of ion density in the bulk to the maximum possible density. Dimensionless length is $\tilde{x} = x/\lambda_D$, dimensionless gradient is $\widetilde{\nabla} = \lambda_D \nabla$ and dimensionless potential is $\tilde{\phi} = ze\phi/k_BT$. This fourth order differential equation is complemented by the following boundary conditions:

$$\tilde{\phi}'''(0) = 0, and \ \tilde{\phi}(0) = zeV/k_BT \tag{1.5}$$
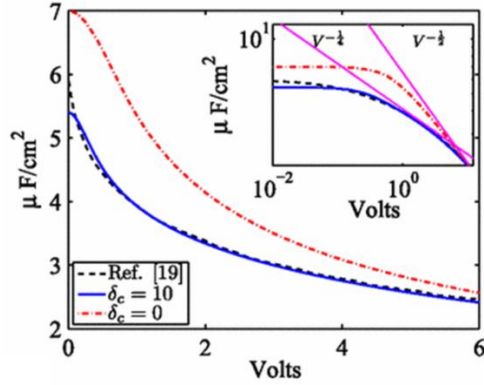
Figure 1.7. Differential capacitance of EDLs in RTILs predicted by the BSK model (solid line), the mean-field model[21], and MD simulations[38]. The inset shows the asymptotic scaling of the differential capacitance with respect to the electrical potential drop across EDLs. Figure is reproduced from Ref. 39.

where V is the potential at the surface relative to the bulk. Equations 1.4 and 1.5 are hereafter termed as the BSK model. The BSK model may be considered as the most significant breakthrough of the EDLs theories in the last five decade because, by going beyond the conventional mean field theories, it enables essential feature of EDLs in electrolytes with strong ion-ion correlations to be predicted with reasonable accuracy. Figure 1.6 compares the structure of EDLs near electrodes with various surface charge densities, and we observe that both overscreening and crowding are predicted quite well. The BSK theory can also predict the differential capacitance of EDLs quite well (see Figure 1.7). While the BSK model has been shown to predict the equilibrium characteristics of EDLs quite well, its performance for predicting the dynamics of EDLs formation has not been established yet and this open question will be addressed in this dissertation.

1.3 Non-equilibrium transport of ions and electrolytes

The non-equilibrium transport of ions and electrolytes has been investigated in various contexts such as microfluidic pumping, biochemical sensing, and charging of supercapacitors. Of

particular importance for electrochemical devices is the electrically-driven transport in nanoscale systems featuring nanopores and nanochannels. When the research reported in this dissertation was performed, there was little work on the non-equilibrium transport of RTILs in nanoscale systems. Here we summarize the key insights from the prior works on non-equilibrium transport of convention electrolytes in nanosystems. While there exists many ways to classify these works, we found it useful to classify them depending on whether and how the EDLs in the nanosystems are perturbed in the transport process because the physics of non-equilibrium transport often differ qualitatively.

1.3.1 Electroosmotic flows in nanosystems

Figure 1.3 shows that, at the liquid side of the EDLs, there is a net excess of counter-ions. If an electrical field exists in the tangential direction of the electrified surface[1], a net force will be generated within the liquid phase (see Figure 1.8). If the electrified surface is stationary, such a net force will lead to a net transport of fluids adjacent to the surface, and this flow is termed the electroosmotic flow (EOF)[40,41]. If the tangential electrical field is applied directly, the induced fluid flow is called the classical EOF. In the Classical EOF, the structure of EDLs is not perturbed except near surfaces with heterogeneous charge densities[42].

The classical theory for describing EOF is based on the Navier-Stokes equation and the PB equation. Without loss of generality, we shall focus on the EOF within a slit channel with a width of W. Assuming that the channel is long and there are no other driving forces for the flow, the fluid velocity is governed by

---

[1] Such a tangential electrical field can either be imposed directly (as in the classical electroosmotic flow) or be induced within the system indirectly (as in induced-charge electroosmotic flow[41]).
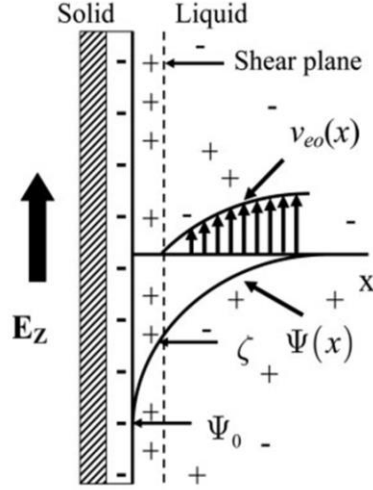
Figure 1.8. Basic concept of electroosmotic flow (EOF). An electrical field in the tangential direction of a stationary, charged solid surface generates a body force within the liquid to drive the EOF. In classical EOF theory, the fluid velocity is assumed to be zero at a "shear plane" adjacent to the surface. The electrostatic potential on the shear plane is termed the ζ–potential. The figure is reproduced from Ref. 43.

$$\frac{d}{dz}\left(\mu\frac{du(z)}{dz}\right) + \sum_{i=1}^{N} ez_i n_i(z)E_x = 0 \qquad (1.6)$$

where μ is dynamic viscosity of the fluid, u is velocity, z is the coordinate perpendicular to channel walls, N is total number of ions and E_x is the electric field tangential to the walls. The density of ions in Equation 1.6 is typically solved using the PB equation (Equations 1.1 and 1.2). Prior works showed that the above theories can predict the EOF with reasonable accuracy only if the no-slip boundary condition is applied at the so-called shear plane, which is located at a short distance (typically one to a few molecular diameters) from the physical surface (see Figure 1.8). The location of the shear plane is usually taken as a fitting parameter in EOF theories. Such a treatment is equivalent to assume that the viscosity of fluids within the shear plane is infinitely high. While this clearly represent an oversimplification of the reality, the idea that the viscosity of fluids adjacent to a charged surface can be much higher than that of bulk liquids is supported by MD simulations (see Figure 1.9). While a number of theories have been
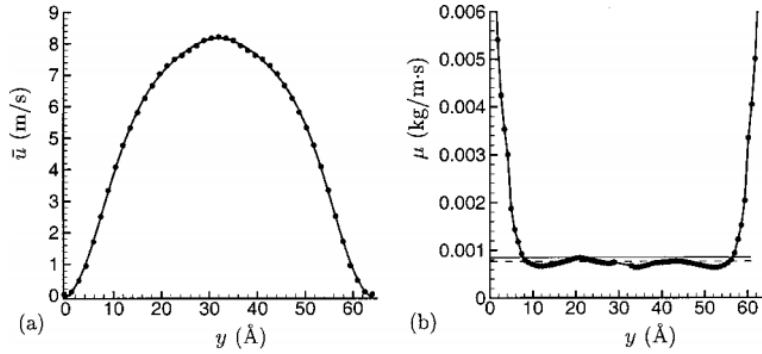
Figure 1.9. Electroosmotic flow through 6.53nm-wide slit nanochannels. (a) the velocity profile computed using MD simulations; (b) the effective viscosity of liquid water extracted from Equation 1.6 using the velocity and ion densities computed from MD simulations as inputs. The thin dashed line denote the viscosity of bulk water. Figures are reproduced from Ref. 44.

proposed to explain the enhanced viscosity of interfacial fluids, recent studies showed that a key reason is the electro-friction between counter-ions and charged surfaces. Specifically, such electro-friction leads to an effective loss of driving force for the fluid. If one uses the Navier-Stokes equation, in which this effect is not taken into account, to interpret the EOF, one must increase the viscosity of interfacial fluids (since the viscosity of interfacial fluids is the only fitting parameter in the EOF model if the ion densities are obtained from first-principle calculations) so that the prediction of the Navier-Stokes equation can agree with that measured in experiments or MD simulations[45].

An interesting observation from previous MD simulations of the EOF in nanochannels is that, apart from the fact that the viscosity of interfacial fluids must be adjusted to values different from bulk fluids, Navier-Stokes equation can quantitatively predict the EOF inside channels as narrow as five molecular diameters. In fact, all anomalies of the EOFs discovered so far, e.g., enhanced viscosity of interfacial fluids and even reversal of EOF direction[46], can be attributed to the failure of the classical theories to take into account atomistic processes (e.g., electro-friction

14

between ions and walls) within a few molecular diameters away from the charged surface. In another word, the classical Navier-Stokes equation is surprising robust down to nanometer scales and can accurately predict the EOF of conventional electrolytes at positions a few molecular diameters away from the charged surface[47].

1.3.2 Ionic transport through nanopores
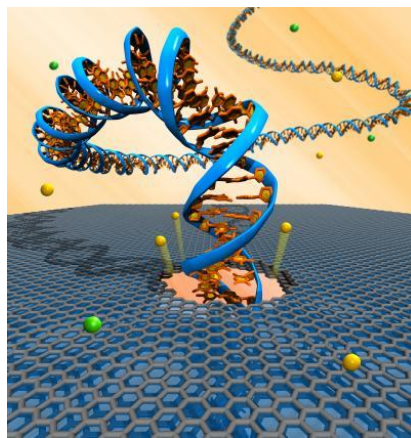
Figure 1.10. Schematic for DNA sequencing using nanopores. Electrical potential difference is applied between two ends of a nanopore, which is immersed in electrolyte solutions. The ionic current through the nanopore is sensitive to pore shape, size and materials passing through them. The sequence of nucleotides on the DNA can be identified by detecting the changes of the ionic current through the nanopore. The figure is reproduced from Ref. 48.

The recent surge in interest in ionic transport through nanopores is, to a large extent, driven by the need to develop ultra-sensitive biochemical analysis systems. For example, Figure 1.10 shows a conceptual sketch of DNA sequencing based on nanopores. The essential idea is to drive DNA through a nanopore with diameter comparable to its diameter using electrical fields, and by detecting the change of ionic current (or, in some designs, the change of voltage on embedded microelectronic components), one can differentiate different base pairs on the DNA strand and accomplish sequencing.

Many intriguing phenomena have been discovered for electrically-driven ionic transport through nanopores. For example, for conical nanopores, the ionic current is found to depend on the polarity of the voltage applied across the pore (this phenomenon is usually termed as current rectification in charged conical nanopores[49,50], see Figure 1.11). These unusual phenomena have been studied extensively, and the underlying mechanisms are now understood reasonably well within the framework of the Poisson-Nernst-Planck (PNP) equations[52]. In this framework, the ionic flux is given by

$$J_i = -D_i \nabla c_i - D_i \frac{z_i e}{k_B T} c_i \nabla \phi + c_i u \qquad (1.6)$$

where D_i is the diffusion coefficient of ith ionic species and u is the local fluid velocity. The first term on the right hand side is the contribution from diffusion, the second term is the contribution from electro-migration, and the third term is the contribution from convection. The mechanism explained in this framework is that current rectification is due to different transference numbers
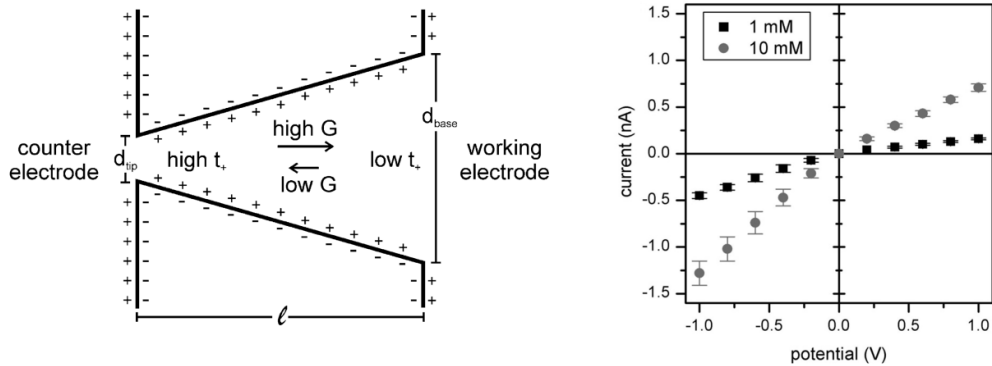
Figure 1.11. A schematic for the cross section of a negatively charged conical pore (left panel) and current-voltage curve showing ion current rectification by a pore with tip length of 85nm filled with 1 mM and 10 mM phosphate buffers (pH 6.7). In the left panel, potential difference is applied between the working electrode and the counter electrode. Regions of high and low cation transference number (t_+) are marked, and arrows show the direction of cation flux in high and low conductance (G) states. The figures are reproduced from Ref. 51.

16
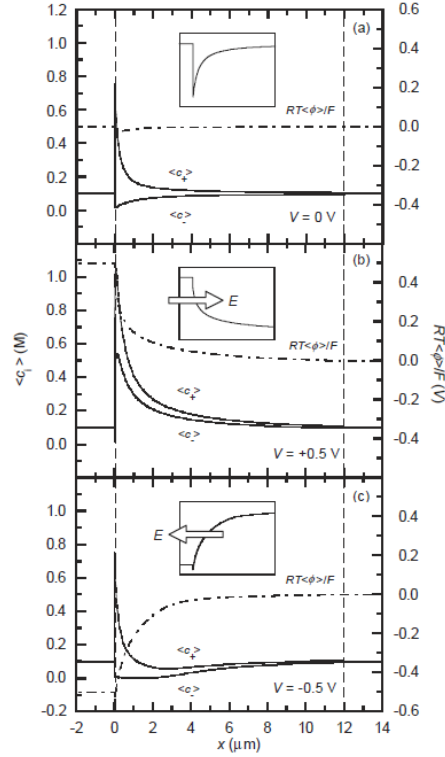
Figure 1.12. Average ion concentration and electrical potential profiles across the system at (a) $V = 0$V; (b) $V = 0.5$V (high conductance state); (c) $V = -0.5$V (low conductance state) when the surface charge density of conical pore is 0.16 C/m². The inset shows the magnified tip region. This figure is reproduced from Ref. 52.

in and around the tip of the conical pore. When cations transport from tip to base ($V = 0.5$V, Figure 1.12b), they are transported from a region with higher transference number to a region with lower transference number, which results in the increase of ion concentration in the pore and a higher conductance; when the cations transported from base to tip ($V = -0.5$V, Figure 1.12c), they are transported from a region with lower transference number to a region with higher transference number, which results in the decrease of ion concentration in pore and a lower conductance. While PNP equations have been proven successful for understanding the ionic transport through nanopores with characteristic dimension much larger than the ion diameter, they may not provide accurate predictions in pores with diameters comparable to the

size of ions or fluid molecules. In such situations, molecular level understanding of the ionic transport is essential. For example, using MD simulations, it has been predicted that, in narrow hydrophobic pores that are initially unwetted by aqueous electrolytes, an abrupt wetting transition can be triggered by the application of strong electric fields that will consequently cause ionic current to jump from zero to a finite value.[53,54] This theoretical prediction has recently been demonstrated experimentally (see Figure 1.13).
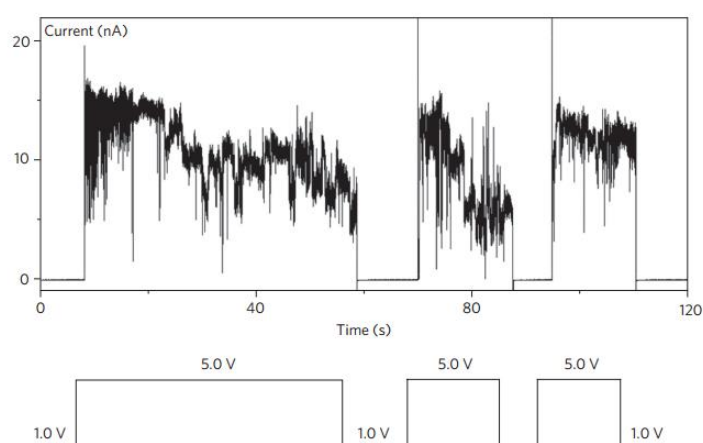
Figure 1.13. Ionic current through a single hydrophobic nanopore. At a voltage difference of 5V between the two sides of the nanopore, the pore is wetted by electrolytes and significant current is observed. At a voltage difference of 1.0V, the nanopore is in the "dry" state and no ionic current is observed.

Most prior research on ionic transport in nanopores is limited to nanopores connected to aqueous electrolyte reservoirs. Ionic transport in nanopores filled with non-aqueous electrolytes has received much less attention despite that non-aqueous electrolytes are widely used in electrochemical systems, whose performance is often controlled by their transport in nanopores. Of the available studies on transport of RTILs in nanopores, most were devoted to the self-diffusion of the ions. For example, the self-diffusion of ions near a graphite surface (see Figure 1.14) with different charge densities has been carefully analyzed and it was found that the self-diffusion of ions is strongly heterogeneous. Under high surface charge densities, the lateral

18
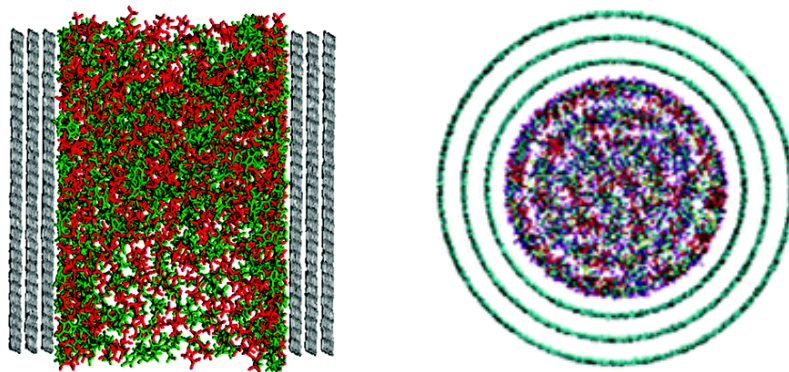
Figure 1.14. Equilibrium transport study for self-diffusion of RTILs in nanopores. The figure on the left is the MD system for studying diffusion of RTILs confined between two parallel plates. The figure on the right is the MD system used for studying diffusion of RTILs in multiwall carbon nanotubes. The figures are reproduced from Refs. 55**Error! Bookmark not defined.** and 56**Error! Bookmark not defined.**.

diffusion of ions in the first counter-ion layer is actually faster than that in bulk RTILs. More systematic studies revealed that diffusion can be hindered or enhanced compared to that in bulk RTILs depending on the size of nanopores and the molecular structure of ions[56,57,58,59]. Studies of electrically-driven transport of RTILs through nanopores are relatively rare. Nonetheless, the Siwy group has studied the electrically-driven transport of RTILs through conical nanopores, and weak rectification of ionic current was observed (see Figure 1.15).
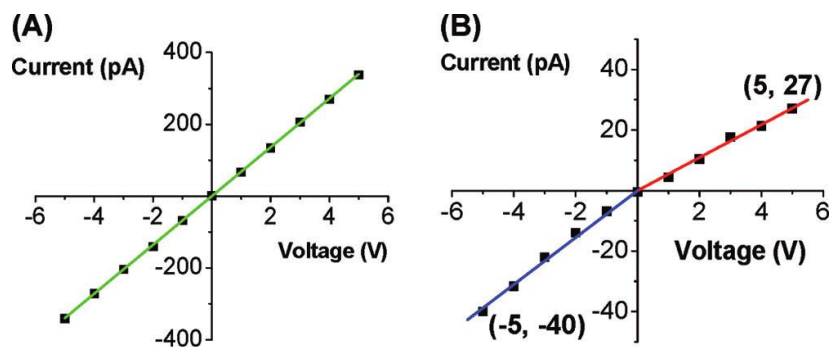
Figure 1.15. Ionic current through nanopores filled with [BMIM][CH3SO4]. Current-voltage curves in a single cylindrical nanopore with a diameter of 90 nm (A) and in a single conical nanopore with the narrow opening of 5 nm in diameter and the big opening of 525 nm (B). Weak current rectification is observed in the conical pore. The figures are reproduced from Ref. 60.

A key finding of the existing research on ionic transport through nanopores is that the macroscopic behavior of ionic transport through nanopores, often characterized by a current-voltage (I-V) curve, strongly depends on the thermodynamic states of the ions such as ion concentration and solvation in nanopores. While thermodynamic states of ions in nanopores are typically controlled by the properties of pore walls such as charge density and wetting behavior, they can also be modulated by applying electric field if the nanopore-electrolyte systems (e.g., charged conical pores immersed in dilute electrolytes) are driven far from equilibrium by the applied field. For conventional electrolytes (especially dilute, fully dissociated electrolytes), the non-equilibrium state of ions within nanopores and its dependence on the applied electric field is relatively well-understood. However, research on non-equilibrium transport of RTILs is still far more limited and merit systematic investigation.

1.3.3 Dynamics of double layer formation

In the ionic transport discussed above, the charge density on the surface does not change with time. Therefore, unless the voltage variation induced by the externally applied voltage is large, the EDLs are either not perturbed (e.g., in EOFs) or only weakly perturbed from their equilibrium state. These situations are in sharp contrast with that encountered in the charging of supercapacitors in which the EDLs near the electrodes are entirely driven by the applied voltages or imposed currents. The formation and relaxation of EDLs have been studied mostly using atomistic simulations, PNP models or its variants, and equivalent circuit models.

In one of the earliest non-equilibrium dynamics studies[61], the dynamics of EDLs formation in molten salts was explored by reversing the sign of the charges on the wall atoms and following the subsequent evolution of the potential across the cell with time. It was found
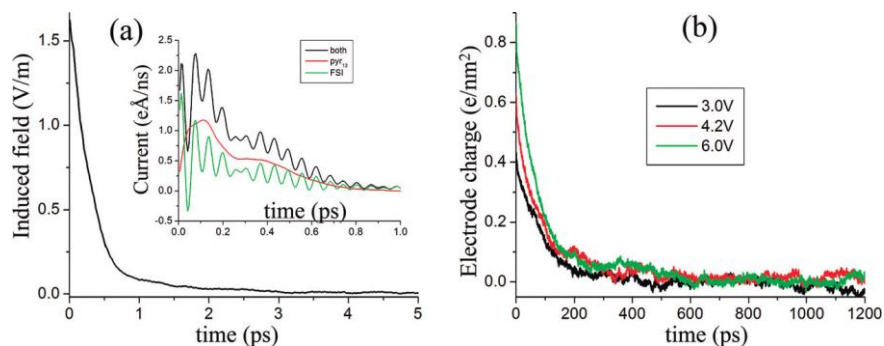
Figure 1.16. (a) Temporal evolutions of induced electric field and electric current contributed from cations and anions. The simulation was performed in a constant-charge setting and the charge on the wall is switched to zero instantaneously in the beginning of the simulation. (b) Relaxation of electrode charge during constant-potential discharging process. These figures are reproduced from Ref. 63.

that the charge relaxation near the wall is very rapid due to the small-scale translation of ions and the large driving force from strong local electric field. In a related work[62], the polarization relaxation of RTILs confined between two oppositely electrified walls was studied by switching off the external electric field and then monitoring the decay of potential in the electrolyte with time. It was discovered that the EDL relaxation consists of a fast process with a time scale of < 0.2 ps that accounts for 80% of the potential drop and a slower process with a characteristic time of ~8 ps; it was also shown that ion diffusion, which occurs on a much longer time scale, is not involved in the EDL relaxation process. More recently, the relaxation of EDLs at an RTIL-graphite interface was studied using two different approaches[63]. In both approaches, the EDLs are equilibrated initially before the studies of dynamics. The difference is that at the beginning of the simulations, the charges on the electrode surface are removed instantly in the first approach, while the electrical potential on the two electrodes was switched to the same value in the second approach. The EDL relaxation probed by the first approach is found to be a fast process occurring over a time scale of picoseconds (see Figure 1.16a). In comparison, the EDL relaxation

21

probed by the second approach is found to occur over a time scale of hundreds of picoseconds (see Figure 1.16b), largely due to the slow ion diffusion involved during the EDL reorganization.

Since RTILs are solvent-free electrolytes and the classical PNP equations, which neglect steric effects and ion-ion correlations, cannot accurately describe the dynamics of EDLs in concentrated electrolytes[21,37,64], the above non-equilibrium studies on the formation and relaxation of EDLs are all based on MD simulations. However, because of the recent breakthrough in the development of continuum models for EDLs in RTILs, continuum simulations of EDL formation in RTILs have become possible. For example, modified PNP equations, which take into account steric effects, have been developed and used to study the ion dynamics in electrochemical cells[64]. Most recently, using the BSK model, the step charging of a parallel electrochemical cell was recently simulated[65], and the results indicated that the essential behavior of charging (i.e., formation of the EDLs) is closely controlled by a new length scale $\sqrt{\lambda_D l_c}$, where λ_D is the Debye length and l_c is the correlation length in RTILs, and a time scale $\lambda_D^{3/2} L/(D l_c^{1/2})$, where D is the ion diffusion coefficient and L is the width of the electrochemical cell. The time scale is consistent with that inferred from the classical resistor-capacitor (RC) circuit model.
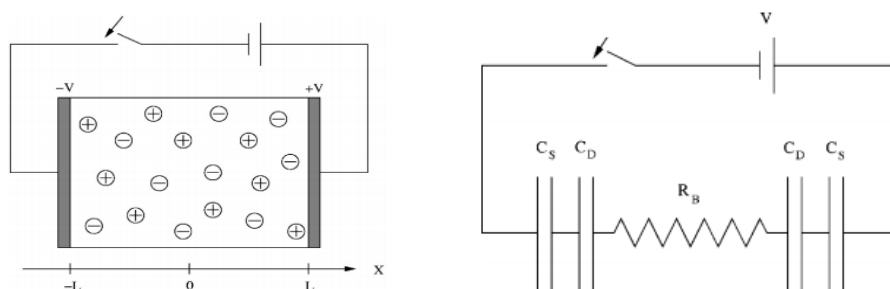
Figure 1.17. A prototype electrochemical cell (left panel) and its equivalent electrical circuit (right panel). The electrochemical cell consists of a slab of electrolyte sandwiched between two electrodes. These figures are reproduced from Ref. 66.

While both MD and continuum simulations help understand the formation and relaxation of EDLs driven by external voltages (or currents), these methods are relatively complicated and are only begun to be used in research. In practice, the EDL dynamics is widely studied using equivalent electrical circuits because of their simplicity and ability to capture some essential features of EDL dynamics. Figure 1.17 shows a prototype electrochemical cell and its equivalent RC circuit. The resistance of the bulk electrolyte is given by

$$R_b = \frac{2L}{\sigma} \tag{1.7}$$

where $2L$ is the thickness of the bulk electrolytes. σ is the electrical conductivity of the bulk electrolyte given by

$$\sigma = F \sum_i c_{i,\infty} |z_i| \mu_i \tag{1.8}$$

where F is the Faraday constant, $c_{i,\infty}$ is the concentration of ith species in the bulk, and μ_i is the mobility of ith ion species. The EDLs near each electrode is modeled as two capacitors (one corresponds to the Stern layer and one corresponds to the diffuse layer, cf. Figure 1.3) in serial. The capacitance of the Stern layer is given by

$$C_S = \frac{\epsilon_s}{l_s} \tag{1.9}$$

where ϵ_s and l_s are the dielectric permittivity and the thickness of the Stern layer, respectively. The capacitance of the diffuse layer is given by

$$C_D = \frac{\epsilon}{\lambda_D} \cosh(e\phi_d/2k_BT) \tag{1.10}$$

where ϕ_d is the potential drop across the diffuse layer of EDLs.

The previous studies on dynamics of EDLs in RTILs have provided fundamental insights into the formation and relaxation of EDLs, but many issues remain to be explored. Some of these issues are critically relevant to the practical applications of EDLs. First, the majority of the prior studies focused on the macroscopic behavior of EDL formation/relaxation by examining the variation of the electrical potential drop across EDLs, but relatively few works provided detailed characterizations for the evolution of EDL structures. Second, most of the existing works dealt with the limiting case of EDL formation or relaxation, i.e., when a step change of the charged state is enforced on the electrode surface. Such a limiting case corresponds to an infinitely large electronic current in the external electric circuit, which is not always realistic. Finally, although the recently developed BSK model[39] can reproduce many EDL properties under equilibrium condition, it is not yet clear whether they can predict the dynamics of EDL formation with accuracy.

1.4 The scope of this dissertation

A thorough understanding of the ion transport in electrochemical devices using RTILs as working electrolyte is essential for exploiting the potential of RTILs in these applications to the fullest extent. The ionic transport in these systems have different features depending on whether and how the EDLs in them are perturbed during the operation. In this dissertation, we study the non-equilibrium transport of RTILs under three different scenarios in which the EDLs are perturbed in very different ways:

(1)   We study the EOF inside slit-shaped nanochannels filled with RTILs using MD simulations. The nanochannels are periodical in the axial direction to mimic a long nanopore. In this case, the EDLs near the nanopore-RTIL interface are barely

perturbed. We will study the ion number densities and EOF velocity distributions across the system. The essential question to address is whether the classical EOF theories developed for conventional electrolytes can predict the EOF in RTILs. In particular, we are interested in whether new features of EOF may emerge due to the strong ion-ion correlations in this new class of electrolytes.

(2) We study the ionic transport through cylindrical nanopores connected with RTILs reservoirs. In this case, the EDLs inside the nanopore can be perturbed strongly in the pore length direction when the voltage drop applied across the pore is large enough. The essential question to address is how the structure of the EDLs inside the nanopore evolves as the applied voltage increases and how this structure evolution ultimately determines the ionic current through the nanopore. We are particularly interested if new features of ionic transport can be observed due to the fact that RTILs are solvent-free. Most of the simulations will be performed using MD method but we will also study the problem using modified PNP equations.

(3) We study the dynamics of EDL formation in an electrochemical cell featuring a pair of planar electrodes separated by RTILs under constant-current charging conditions, a scenario frequently encountered in galvanostatic electrochemical experiments. In this case, the EDLs form dynamically in response to the applied current, i.e., the EDLs are perturbed in the direction normal to the electrode. The essential question to answer is how the electrical potential across the cell evolves during the charging process, and how such response is governed by the transport of ions. We will determine the spatial and temporal evolution of the ion densities across the cell. We will also examine

whether the ion transport model proposed by Professors Bazant, Storey and Kornyshev can predict the dynamics of EDL formation.

The rest of this dissertation is organized as follows. In Chapter 2, we present the study of the EOF of RTILs in nanochannels. In Chapter 3, we present the study of the electrically-driven transport of RTILs through cylindrical nanopores connected with large electrolyte reservoirs. In Chapter 4, we present MD and continuum simulations of the charging dynamics of EDLs in an electrochemical cell under the constant-current charging condition. Finally, conclusions will be presented in Chapter 5.

CHAPTER 2

Electrokinetic Transport of RTILs in Nanochannels

Electrokinetic transport in RTILs plays an important role in their applications, but is only begun to be understood. In this chapter we present the atomistic simulation of EOF in RTILs. We find that, although the EOF is suppressed by the ion-wall electrofriction, its strength greatly exceeds that predicted by classical hydrodynamic theories if correct ion distribution is used and electrofriction effects are effectively accounted for. We trace the unexpected flow strength to the short-wavelength nature of EOF in RTILs. We show that the EOF in RTILs is a rare example in which short-wavelength hydrodynamics profoundly affects flow measureables in macroscopic systems, and thus is a good test bed for developing improved theories for generalized hydrodynamics.

2.1 Models, simulation system and methods

We simulated the EOFs in slit-shaped nanopores. Since we are interested in the generic features of EOFs in RTILs rather than their electrolyte specificity, RTILs were modeled as charged spheres interacting via a potential given by

$$\phi_{ij} = 4\varepsilon_{ij}\frac{\sigma_{ij}^{12}}{r_{ij}^{12}} + \frac{z_i z_j e^2}{4\pi\varepsilon_0\varepsilon_r}\frac{1}{r_{ij}} \tag{2.1}$$

where σ_{ij} and ε_{ij} are Lennard-Jones (LJ) parameters, r_{ij} is the distance between ions i and j, z_i is the valence of ion i, e is the unit charge, ε_0 is the vacuum permittivity, and $\varepsilon_r = 2$ is a dielectric screening constant accounting for the electronic polarizability of ions not explicitly

27

modeled here. This model captures essential features of the electrical double layers (EDLs) in RTILs such as charge over-screening well[29,67]. It has also been established that coarse-grained models can capture key features of EOFs in conventional electrolytes very well.[68,69] As will be
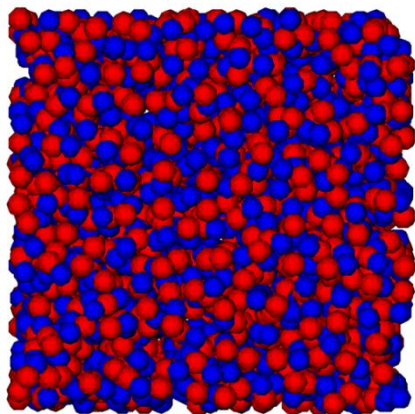
Figure 2.1. A snapshot for bulk model RTILs in MD simulation visualized by VMD[70]. MD simulation is performed in an NPT ensemble to calculate radial distribution function (RDF) and density at atmosphere pressure.
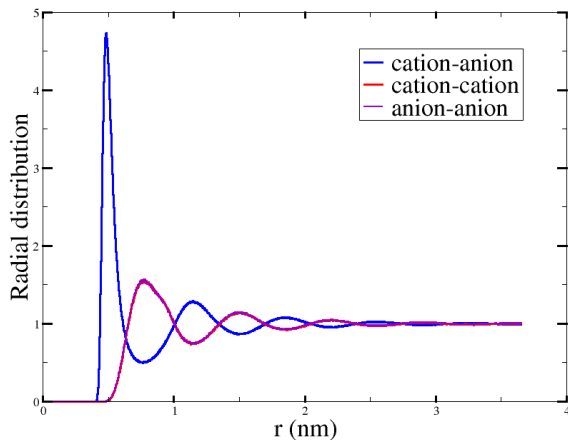
Figure 2.2. RDFs for model RTILs used in our work. The size and mass are the same for both cation and anion. The peak for cation-anion RDF is at r=0.5nm, which indicate σ of the ions. The RDFs indicate the model RTILs is in liquid state.

shown below, this model also captures the key features of the hydrodynamics in RTILs down to molecular scale. In this work, cations and anions are monovalent ions, and all atoms have the

28

same σ and mass m. In the following, all physical quantities will be given in the reduced units, e.g., mass, length, and charge are measured by m, σ and the charge of cation; time, velocity and electrical field are measured $(m\sigma^2/\varepsilon)^{0.5}$, $(\varepsilon/m)^{0.5}$ and $\varepsilon/(\sigma e)$, respectively.
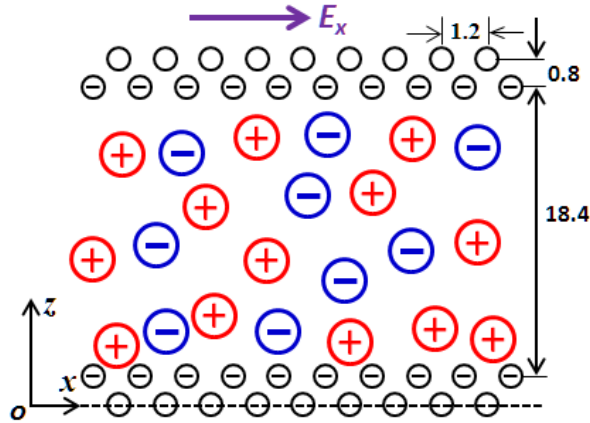
Figure 2.3. A schematic of the simulation system. There are 1200 cations and 1108 anions inside the channel.

The simulation system consists of a slab of RTILs sandwiched between two fixed walls (see Figure 2.3). Each wall is made of two staggered layers of atoms ($\sigma_{wall} = 0.627\sigma_{ion}$) arranged in square lattices. The wall structure was designed so that no significant slip is observed near the wall in our coarse-grained simulations, which allows us to focus on the EOF in the interior of the pore. The atom layers in contact with the RTILs were assigned partial charges so that the surface charge density of each pore wall is -0.188 e/σ^2 (for $\sigma = 0.5$ nm, which is quite typical for ions in RTILs, this corresponds to a charge density of -0.12 C/m^2). The pore width is 18.4. The number of ions inside the pore was chosen such that the entire system is electrically neutral and bulk-like RTILs with cation/anion number density of 0.26 exist in the pore center. The temperature of RTILs was set to 1.0. Similar parameters have been used successfully in

prior modeling of EDL capacitance in RTILs[29], and we confirmed that RTILs described using these parameters are dense liquids by examining the ion-ion pair correlation functions.

Simulations were performed using a modified MD code Gromacs in the NVT ensemble[71]. Periodic boundary conditions were used in all three directions. The cutoff method was used to compute the non-electrostatic interactions, and the Lorentz-Berthelot rule was used to compute the LJ parameters for wall-ion interactions. To remove the periodicity in the direction normal to the pore walls, the simulation box length in this direction was set to be three times of the pore width, and the slab-PME method was used to compute the electrostatic interactions[72]. An external electrical field E = 1.03 was applied in the *x*-direction to drive the EOF. A Nose-Hoover thermostat was used to maintain the RTIL temperature at T = 1.0. To avoid biasing the velocity profile, only the velocity components in the directions orthogonal to the flow were thermostated. The system was first run 2 million steps to reach a steady state (time step: 0.004), which was followed by a production run of 14 million steps.

2.2 Results and discussions

Figure 2.4a shows the density distribution of the cations and anions across the pore. We observe that, near the negatively charged pore walls, alternating layers of cations and anions form and this pattern persists to a position ~8 molecular diameters (i.e., 8 σ) from the surface. To measure how the wall charges are screened by the ions, we computed a charge screening factor C_f[46]

$$C_f(z) = \int_0^z (n_- - n_+) dz / \sigma_s \tag{2.2}$$
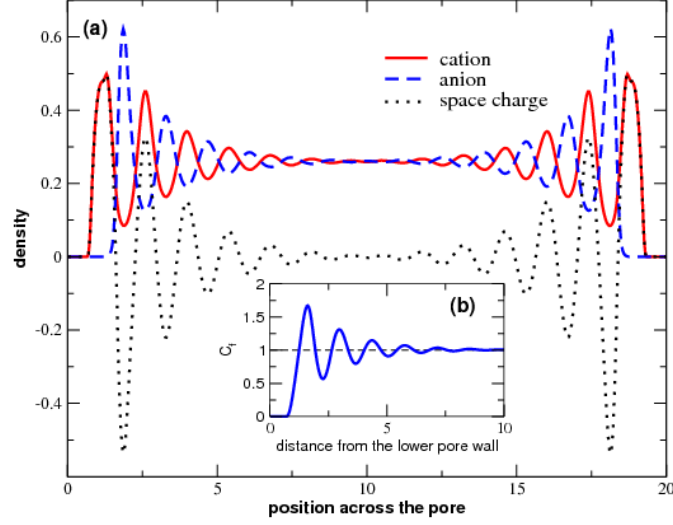
Figure 2.4. (a) Distribution of cation density, anion density and space charge density across the pore. (b) Distribution of the screening factor $C_f(z)$ defined in Equation 2.2 near the lower pore wall.

where σ_s is the surface charge density, and n_+ and n_- are the number density of cation and anions, respectively. $C_f(z) = 1.0$ corresponds to a complete screening of the electrode charge at position z, and $C_f(z) > 1.0$ corresponds to an over-screening of the electrode charge. Figure 2.4b shows that the surface charge starts to be overscreened at $z = 1.21$. At larger distance, the degree of screening oscillates and C_f approaches 1.0 only at $z \approx 7$. These EDL features revealed in Figure 2.4, e.g., alternating and persistent layering of ions and surface charge over-screening, are consistent with that observed in prior coarse-grained and fully-detailed modeling of EDLs in RTILs, and are mainly caused by the strong ion-ion correlations inside RTILs[29,33]. These results confirm that the model and simulation methods used here are adequate for studying EDL phenomena in RTILs.

We next study the EOF inside the pore. Since the EOF stands for the collective (convective) transport of fluids (here, our fluid is an ionic mixture), the EOF velocity at an arbitrary position z in the pore can be defined as $u(z) = (n_+(z)u_+(z)+n_-(z)u_-(z))/(n_+(z)+n_-(z))$,

31
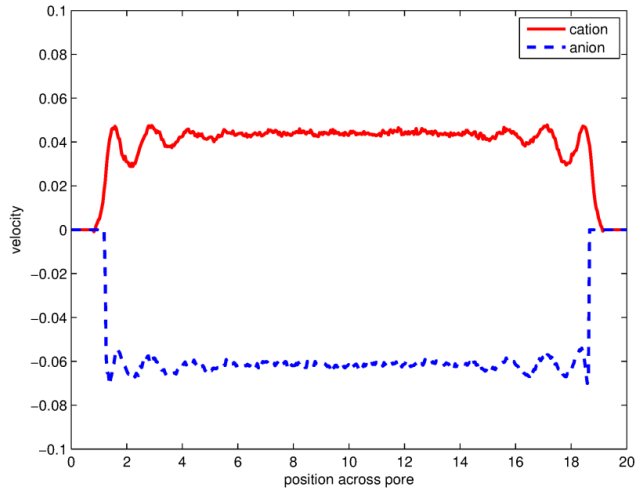
Figure 2.5 Distribution of velocities of cation $u_+(z)$ and anion $u_-(z)$ across the pore.

where n_+ (n_-) and u_+ (u_-) are the density and velocity of the cation (anion).[73] Figure 2.6 shows the

distribution of EOF velocity across the pore. We observe that (1) the EOF velocity oscillates

significantly near the charged wall, and (2) the EOF direction in the pore center is in the negative

direction, while the classical electrokinetic theories predict the flow to be in the positive

direction at position away from the pore wall. The first observation is caused by the oscillatory

driving force in the pore (cf. the space charge distribution in Figure 2.4a), which is in turn caused

by the alternating layering of cations and anions near the wall. The second observation is caused

by electro-friction and charge over-screening. Specifically, because of the strong electrofriction

between the cations adsorbed on pore wall and the wall atoms, these cations do not effectively

render driving force to the flow. The anion layer immediately adjacent to the contact-adsorbed

cations, however, can render driving force effectively, and this leads to a reversal of flow

compared that expected from the classical theories in which these effects are neglected[46]. Since

similar phenomenon has been observed in conventional concentrated electrolytes exhibiting

strong ion-ion correlations[46], and RTILs are characterized by strong ion-ion correlations, the

32

present finding is not surprising – in fact, it is an indication that our simulation can capture key features of EOFs in electrolytes with strong ion-ion correlations.
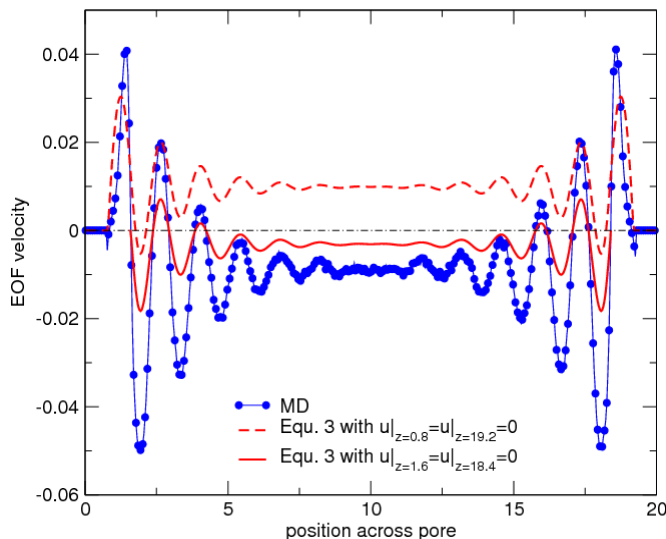
Figure 2.6. Distribution of EOF velocity across the pore obtained from MD simulations and from solving Equation 2.3 using a constant viscosity of 1.39 across the pore.

The EOF velocity profile shown in Figure 2.6 seems to be consistent with the understanding of EOF obtained from molecular simulations of concentrated electrolytes[74,75]. However, significant difference exists. Specifically, extensive MD simulations of EOF in the past decade suggest that, while the classical electrokinetic theories cannot quantitatively describe the EOF in a region very close to the charged surface due to atomistic effects such as electro-friction, slip, anomalous interfacial fluid structure, *etc*,[68,75,76] (general models capable of accounting for these effects are still lacking at present), EOFs at positions ~ 1-2 ion or solvent diameters away from the charged surfaces can typically be described *quantitatively* by classical theories[77,78]. In another word, if the EOF velocity u at any given position 2 ion (or solvent) diameters away from a charged surface is known, u at locations further away from this position can be predicted

$$\mu \frac{\partial^2 u}{\partial z^2} + e(n_+ - n_-)E_{ext} = 0 \tag{2.3}$$

quantitatively by solving using the velocity at the given position as boundary condition. Here μ is

the viscosity of the bulk fluids and E_{ext} is the electrical field parallel to the charged surface.

Such a conclusion, however, fails for the EOFs in RTILs. To demonstrate this, we first compute

the viscosity of RTILs in our pore. Specifically, we set up a box of homogeneous RTILs (box

size: 14.7× 14.7×18.5) with the same density and temperature as the RTILs in center of our pore.

Following the Sinusoidal Transverse Force (STF) method[79] (also called periodic perturbation

method[80]) we applied a body force on all ions in the form of a cosine wave across the z-direction

of the simulation box, and obtained a viscosity of 1.39±0.02 by measuring the generated fluid

flow. Alternatively, we applied a uniform acceleration on all ions inside the pore and retrieved

the viscosity by fitting the generated Poiseuille flow to that predicted by the Navier-Stokes

equations. The width of channel is divided into several bins and we assume the viscosity is

constant in each bin. The equation for pressure-driven flow and the formula for viscosity

calculation in each bin are shown below

$$\rho_i g_x + \frac{\partial}{\partial z}\left(\mu_i \left(\frac{\partial u_x}{\partial z}\right)\right) = 0 \tag{2.4}$$

$$\mu_{x_i} = \frac{-g_x \int_{x_i}^{x_{i+1}}\left(\int_0^{x_i} \rho_i dx\right)dx}{u_{x_{i+1}} - u_{x_i}} \tag{2.5}$$

Using Equation 2.5, the viscosity was found to decrease from 1.47±0.10 at z = 10 (i.e., pore

center) to 1.33±0.12 at z=1.5, indicating that the fluid viscosity probed by a Poiseuille flow is

rather uniform across the pore. We next solved Equation 2.3 using the MD velocities at $z = 1.6$
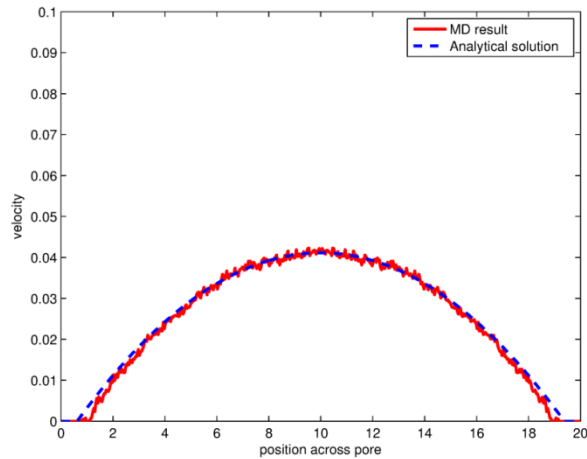
Figure 2.7. Velocity profiles for pressure-driven flow in nanochannels from MD simulation and analytical solution.

and 18.4 as boundary conditions and a viscosity of 1.39. We chose to let the velocities at $z = 1.6$ and 18.4 to be given *a priori* when solving Equation 2.3 for two reasons. First, these two points are sufficiently away from the pore wall so that atomistic effects (e.g., ion-wall electrofriction) neglected in Equation 2.3 will not significantly affect the prediction of EOF by Equation 2.3. Second, such a choice is convenient because the velocity is zero at these points. One can choose any other positions $1.6 < z < 18.4$ at which the velocities are given *a priori* and the same conclusion will be arrived. Figure 2.6 compares the velocity predicted by Equation 2.3 with that obtained from MD simulations, and poor agreement is found. In fact, the EOF velocity at the pore center obtained from MD simulation is three times of that predicted by Equation 2.3, i.e., the classical electrokinetic theory significantly under-estimate the EOF even if the velocity at position ~2 molecular diameter from the wall is known in advance. To the best of our knowledge, such an observation has not been reported previously for EOFs.
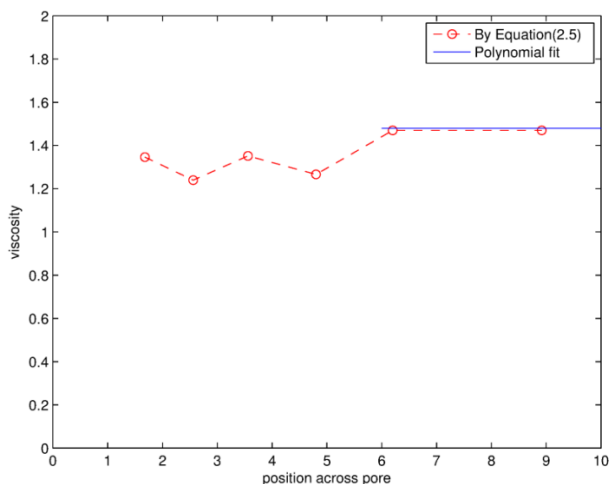
Figure 2.8. Variation of dynamical viscosity calculated from velocity profile in a pressure-driven flow in nanochannels obtained from MD simulations. The viscosity is calculated by both polynomial fitting to the central portion of velocity profile and using equation 2.5.

We hypothesize that the underestimation of EOF by the classical electrokinetic theory (or, equivalently, the apparent amplification of EOF compared to the prediction by classical theories) is caused by the short-wavelength nature of the EOF in RTILs. As shown earlier, the very strong ion-ion correlations in RTILs lead to alternating layering of cations and anions near the charged wall, which in turn leads to driving forces and shearing forces that oscillate rapidly near the wall. Under the action of these rapidly oscillating shearing forces, the EOF velocity then oscillates rapidly and the flow will feature significant short-wavelength components. To see this clearly, we transform the real space EOF velocity distribution to the k-space. Figure 2.9 shows the spectrum of the EOF velocity. We observe that three flow components with wavenumbers k = 2.99, 4.30 and 5.22 (the corresponding wavelengths $\lambda = 2\pi/k$ are 2.10, 1.46, and 1.12, respectively) contribute significantly to the total EOF. Since the wavelengths of these flow components are comparable to the size of RTIL molecules, the shearing behavior of RTILs in

36

such flows can differ significantly from that in flows featuring only very large wavelengths. Indeed, the generalized hydrodynamics theories show that the generalized viscosity of bulk
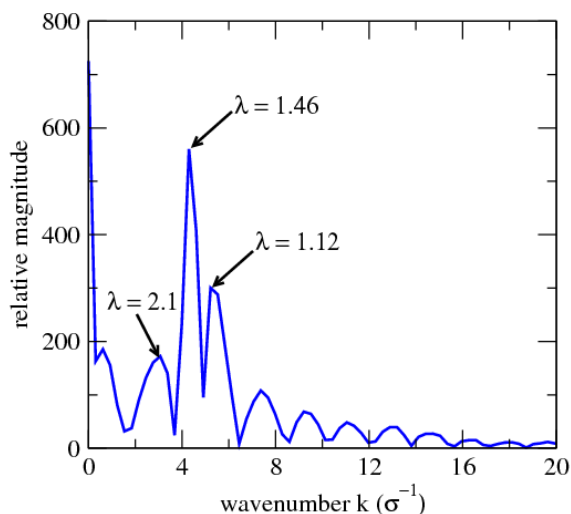
Figure 2.9. Spectrum of the EOF velocity profile obtained from MD simulations (*cf.* Figure 2.6). The wavelength λ is related to the wavenumber by $\lambda = 2\pi/k$.

fluids decreases as the wavenumber (*wavelength*) of flow increases (*decreases*), and it approaches the viscosity in classical hydrodynamics only in the limit of zero wavenumber or infinite wavelength[81,82,83,84]. We computed the wavenumber-dependent viscosity of bulk RTILs at the same thermodynamic state as the RTILs in the central portion of our slit pore using the STF method, and the results are shown in Figure 2.11. We observe that the generalized viscosity of our RTILs decreases rapidly as the wavenumber increases. At $k = 3.00$ and 7.14 (or $\lambda = 2.09$ and 0.88 molecular diameters), it reaches 50% and 10% of its value at $k = 0$. Since the EOF shown in Figure 2.6 is dominated by flow components with wavenumber of 3-7 (or wavelength 0.9-2.1 times of the ion diameter), the generalized viscosity experienced by these flow components is expected to be 50%-90% smaller than the viscosity at infinite wavelength, i.e., the viscosity used in the classical electrokinetic model (Equation 2.3), hence explaining why the EOF predicted using Equation 2.3 is much weaker than that observed in MD simulations. As a side note, we
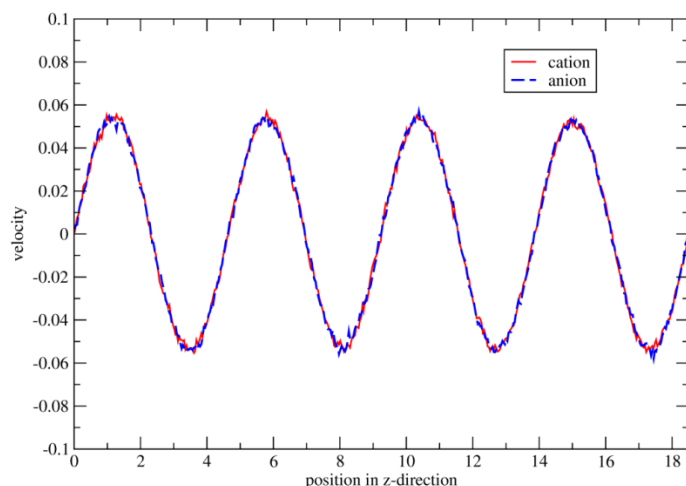
Figure 2.10. A typical distribrution of cation and anion velocities in z-direction across bulk RITLs using STF method. In this case, the wave number *k* is 1.36.

note that the trends of generalized viscosity shown in Figure 2.11 agree quite well with that obtained in more sophisticated simulations of RTILs. Specifically, using polarizable all-atom force fields, Yan *et al.* found that the generalized viscosity of 1-ethyl-3-methylimidazolium nitrate (EMI-NO$_3$) is reduced to 50% and 10% of its hydrodynamic limit value at a wavelength of ~0.96 and ~0.37 nm (or 2.4 and 0.93 ion diameter since the diameter of EMI$^+$ and NO$_3^-$ ions are ~0.4 nm)[85], while the generalized viscosity of our RTILs reduces to 50% and 10% of its large wavelength limit value at wave-lengths of 2.09 and 0.88 ion diameters. The reasonable agreement between the scaling of the generalized viscosities obtained from our coarse-grained simulations and from fully-detailed simulations indicates that the coarse-grained model can reasonably capture the hydrodynamic behavior of the RTILs down to molecular scale.

To further ascertain that the inaccurate prediction of EOF at position away from the pore wall by the classical electrokinetic theories is caused by their failure to account for wavelength-dependent transport, we extracted the shear stress across pore from the MD velocity profile shown in Figure 2.6 using two methods. Firstly, we computed the shear stress using

38
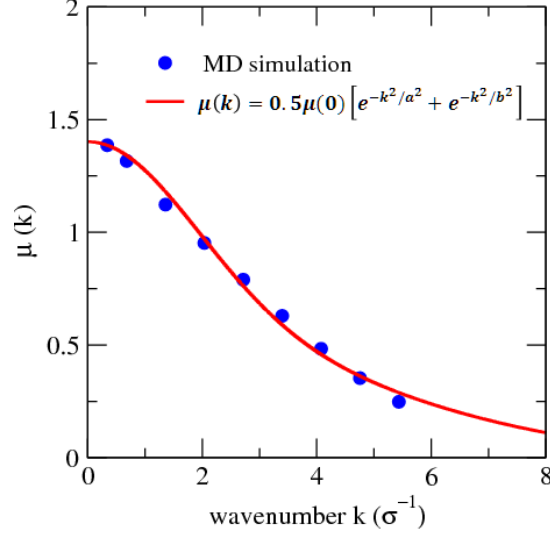
Figure 2.11. Variaion of the generalized viscosity of the model RTILs as a function of wavenumber. Solid line is a fitting of the MD data to the Gaussian form of generalized viscosity proposed in Ref. 86. The fitting parameters are $\mu(0) = 1.39$, a= 5.134, and b= 12.228.

$$\tau_{zx}(z) = \mu\dot{\gamma}(z) \tag{2.4}$$

where μ is the fluid viscosity at the hydrodynamic limit, $\dot{\gamma}(z) = du/dz$ is the local strain rate at position z. In this calculation, the shear stress is assumed to depend only on local strain rate, which is a basic premise of all classical electrokinetic theories. Secondly, we computed the shear stress using generalized hydrodynamics that account for the wavelength-dependent nature of fluid transport, i.e.,[86,85,87]

$$\tau_{zx}(z) = \int_{-\infty}^{\infty} \mu(z - z')\dot{\gamma}(z')dz' \tag{2.5}$$

where $\mu(z - z')$ is the viscosity kernel, which is also the real-space transformation of the generalized viscosity $\mu(k)$. Implementing Equation 2.4 requires the local strain rate $\dot{\gamma}(z)$ to be computed, which is difficult since the MD velocity data contains noise. To circumvent this, we computed $\dot{\gamma}(z)$ by first fitting the MD velocity profile to piecewise polynomials and then analytically differentiating the polynomials. The viscosity of the fluids was taken as 1.39. In
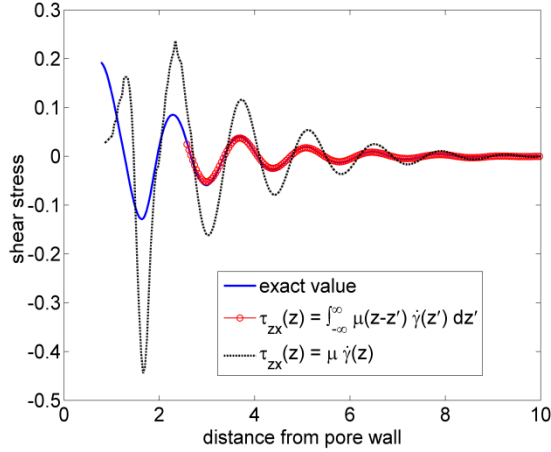
Figure 2.12. Distribution of fluid shear stress in half of the pore computed from Equations (2.4) and (2.5), and by integrating the electrical body force acting on the fluids.

implementing Equation 2.5, we used the fact that the viscosity kernel has a finite width, and reduced Equation 2.5 to $\tau_{zx}(z) = -\int_{-\infty}^{\infty} \mu'(z - z')u(z')dz'$ where μ' is the derivative of viscosity kernel. Since an effective way to compute the inhomogeneous viscosity kernel in confined dense liquids is yet to emerge[88], the viscosity kernel of the fluids confined inside the pore was taken as that of homogeneous fluids at the same temperature and density in this work. Specifically, the viscosity kernel was obtained by first fitting the generalized viscosity $\mu(k)$ to the Gaussian form suggested in Ref. 86 and then by transforming the fitted $\mu(k)$ to the real space. The half-width of the real-space viscosity kernel was taken as 1.6 when performing the integration shown in Equation 2.5. Since the MD fluid velocity is defined only in region $0.8 < z$ < 19.2 and the generalized hydrodynamic theories for interfacial and confined fluids are not yet available, we computed the shear stress only in the region $2.4 < z < 17.6$. Figure 2.12 compares the shear stress computed using Equations 2.4 and 2.5 with the exact value obtained by integrating the electrical body force acting on the fluids. We observe that Equation 2.4 significantly overestimates the shear stress throughout the pore. Although the shear stress can

only be computed in the middle portion of the pore when Equation 2.5 is used, the computed stress agrees very well with the exact value. These results confirm that generalized hydrodynamics are necessary and *sufficient* to accurately predict the fluid shear stress (and thus the EOF) at position away from the pore wall, and the classical hydrodynamics neglecting the short-wavelength nature of the EOF fails quantitatively. We note that the conclusion that generalized hydrodynamics can predict fluid flows with strong short-wavelength components has been reported in a prior study[89], although the fluids are homogeneous and under the action of hypothetical sinusoidal body forces in that prior study. The above results confirm that this conclusion also holds at least at positions away from the pore wall for confined fluids. A more difficult question, i.e., how to compute the stress of interfacial fluids, remains open and merits further study.

In the above simulations, we showed that short wavelength hydrodynamics tend to amplify EOFs in RTILs near walls with a moderate surface charge density. We expect this conclusion to hold for other surface charge densities too. This is because the short wavelength hydrodynamics originates from the fact that EOFs in RTILs features significant short wavelength components (as evident in Figure 2.9), which is in turn caused by the strong ion-ion correlations in RTILs. Since ion-ion correlations do not depend strongly on the surface charge density (except when the surface charge density is so high that lattice saturation occurs in the first interfacial ion layer[37]. Even under such a condition, the ion-ion correlations are still important at positions beyond the lattice-saturated layers), EOFs in RTILs will always feature short wavelength components, and hence the amplification phenomenon observed here will be important regardless of the magnitude of the surface charge density. We also performed simulations using [BMIM][PF$_6$] as working electrolytes (the RTIL was modeled using the semi-

coarse grained force field proposed in Ref. 90), and similar amplification phenomenon was observed. It is worth noting that EOF can also be affected by various interfacial effects such as charge-induced thickening[41], which tend to weaken the EOF. These interfacial effects are nearly always limited within the first ion or solvent layer (<1nm), and they can counteract with the effects of short wavelength hydrodynamics at those positions. However, short wavelength hydrodynamics persist much deeper from the wall toward the fluids (several ion layers or a few nanometers), and thus at these positions, the amplification effects of short wavelength hydrodynamics will always be important.

The foundations of generalized hydrodynamics theories that can account for wavelength-dependent transport have been developed more than four decades ago[81,82,83,84]. Since then, both the application and advancement of these theories have been relatively limited, at least when compared to other branches of fluid dynamics. This is likely caused by the fact that there are few practical systems in which classical hydrodynamics are inadequate and thus the non-local stress-strain rate relation or the small-wavelength nature of flow *must* be taken into account. The emergence of nanofluidics[91], i.e., transport of fluids in nanometer wide pores and channels, brings renewed interest in these theories. However, a majority of nanofluidic studies suggest that, except at position in close vicinity of the wall, the classical hydrodynamic theories are robust enough to predict flows in pores down to five to ten molecular diameter with good accuracy[92,93]. In fact, there are few practical nanofluidic examples in which the error caused by neglecting the non-localness of stress-strain relation (or equivalently, the small-wavelength nature of flow) will lead to an error ~100% in flow prediction. Identifying such problems is not only important for gaining fundamental insights into the problems themselves, but also for developing and testing improved generalized hydrodynamics theories. The results above suggest that EOF in RTILs is

one of such problems. The uniqueness of EOF lies in that the strength of the flow does not depend on the size of the charged pore providing that the EDLs near opposing pore walls do not overlap. Therefore, although short-wavelength hydrodynamics *directly* affects the flow only within the EDLs (in RTILs, the EDL thickness is often one to several nanometers[29,94,95]), its effects can be measured at position far away from the surface. In addition, since the EOF strength does not vary outside of the EDLs, the amplification of EOFs by short-wavelength hydrodynamics can be assessed in micrometer-wide pores rather than only in nanopores, which facilitates experimental study.

2.3 Conclusions

The electrokinetic transport in a slit-shaped nanopore filled with RTILs has been investigated using MD simulations. Due to the strong ion-ion correlations, alternating layers of anions and cations form near the charged pore wall and this pattern extends about eight molecular diameters deep into the bulk electrolyte. Under the action of a tangential electrical field, an oscillatory body force varying over molecular distances induces EOF with significant short-wavelength components. Due to the short-wavelength nature of the flow, EOF is significantly amplified compared to that predicted by the classical hydrodynamic theories if the electrofriction effects are taken into account effectively. We suggest that EOF in RTILs is a rare example in which short-wavelength hydrodynamics, or equivalently the non-localness of stress-strain rate relation, significantly affects the macroscopic characteristics of a flow even if the flow occurs in micrometer-wide pores. We envision that EOF in RTILs to be a good test problem for developing and testing improved generalized hydrodynamics theories.

CHAPTER 3

Transport of RTILs in Cylindrical Nanopores

In this chapter, electrically driven ionic transport of RTILs through nanopores is studied using atomistic simulations. The results show that, in nanopores wetted by RTILs, a gradual *dewetting* transition occurs upon increasing the applied voltage, which is accompanied by a sharp *increase* of ionic current. These phenomena originate from the solvent-free nature of RTILs and are in stark contrast with the transport of conventional electrolytes through nanopores. Amplification is possible by controlling the properties of the nanopore and RTILs, and we show that it is especially pronounced in charged nanopores. The results highlight the unique physics of non-equilibrium transport of RTILs in confined geometries and point to potential experimental approaches for manipulating ionic transport in nanopores, which can benefit diverse techniques including nanofluidic circuitry and nanopore analytics.

3.1 MD systems and methods

3.1.1 Single-nanopore and single-reservoir system

Here, we use atomistic MD simulations to study the ionic transport of RTILs through a nanopore driven by an electric field. Figure 3.1 shows a schematic of the simulated system, which consists of a nanopore with two ends connected to a reservoir filled with [BMIM][PF$_6$], an immidazolium-based RTIL. A (32, 0) single wall carbon nanotube with a center-to-center diameter of 2.51 nm was used as the nanopore. Taking a diameter of 0.34 nm for the carbon atoms, the access diameter of the nanopore is 2.17 nm. Hereafter, the access diameter is used to

compute the average RTIL density and conductivity in nanopore. Carbon nanotubes were used as nanopores due to their well-defined geometry.
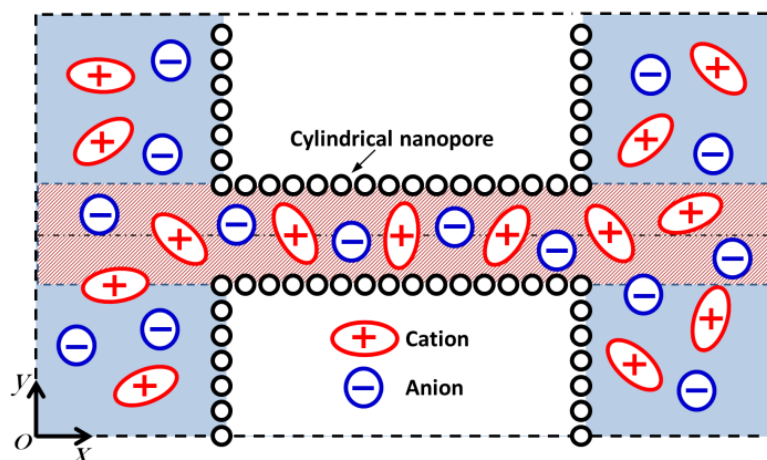
Figure 3.1. A schematic of the MD system for studying ionic transport of RTILs through a nanopore driven by electric fields. The system consists of a nanopore and a RTIL reservoir. Dashed lines denote the periodic simulation box, which measures 20.0 nm, 12.3 nm and 12.3 nm in x-, y- and z-directions, respectively.

MD simulations were performed in the NVT ensemble using the Gromacs package[71]. The length of the nanopore and the RTIL reservoir were both 10 nm. Periodic boundary conditions were applied in all three directions. The RTILs were modeled using the force field developed in Ref. 90, and carbon nanotube was modeled using the force field described in Ref. 96. The vertical walls were modeled as carbon atoms with the same Lennard-Jones parameters as those for the nanopore. The Lennard-Jones parameters for interactions between atoms of RTILs, nanotube and the vertical walls were obtained using the Lorentz-Berthelot combination rule. The number of ions inside the system was adjusted so that the system is neutral and the ion density at the center of RTIL reservoir matches that of a bulk [BMIM][PF$_6$] at 400 K and 1 atm (2.68#/nm^3). The vertical wall atoms and two ends of the nanopore were fixed during simulations. The temperature of RTILs and vibrating CNT atoms were maintained at 400 K

using the velocity rescaling method with a time constants of 1 ps for ions and 0.25 ps for vibrating CNT atoms. The smaller time constant for carbon nanotube atom is necessary to ensure that the heat generated during ionic transport is effectively dissipated. Electrostatic interactions were calculated using PME method (real space cutoff: 1.6 nm; FFT spacing: 0.12 nm). Non-electrostatic interactions were computed using the cutoff method (cutoff radius: 1.6 nm). The neighbor list was updated each time step (2 fs). Bond lengths for RTIL ions were constrained using the LINCS algorithm during the simulations[97].

Each simulation consisted of a trial run of 5 ns to reach a steady state and a production run of 25 ns. Five independent cases were studied to estimate the error bars. To determine the ionic currents, we used the method detailed in Ref. 99. This requires computing the displacement of the effective charge center of the entire system

$$\mathrm{DC_c}(t) = \langle 1/L_x \sum_{i=1}^{N} q_i [x_i(t) - x_i(0)] \rangle \tag{3.1}$$

where q_i and $x_i(t \text{ or } 0)$ are the charge and x-position of each atom i inside the system, and $\langle \cdots \rangle$ denotes the ensemble average. During simulation, the position of each atom was recorded every 0.2 ps to compute the drift of effective charge center $C_c(t)$. Next, the ionic current was obtained through a linear regression of $C_c(t)$. Such a method for computing current is used in both the nanopore + RTIL system, in periodic nanopores, and in bulk RTILs. To compute the conductivity of RTILs confined in periodic nanopores, we computed the current I through nanopore at different electric field E_x and the conductivity is evaluated by $\sigma = \frac{I}{E_x A}$, where A is the cross-section area of the nanopore based on the accessible diameter of nanopore. To compute

the conductivity of bulk RTILs, a uniform electric field was applied to bulk RTILs and the above procedure was used except that A was taken as the cross-section area of the bulk RTILs.

We verified that the phenomena reported here can be reproduced in other nanopores (e.g., those obtained by drilling through a FCC lattice). Two types of nanotubes were studied: neutral nanotubes and charged nanotubes. For charged nanotubes, partial charges of small magnitude were decorated on the pore surface to give a net charge density of -0.05 C/m^2. The uniform surface charge is similar to that induced by applying a gate voltage to dielectric materials[98]. We also studied charged nanotubes in which discrete charge groups were decorated on their surface, and qualitatively similar results were obtained. Two vertical walls, each consisting of carbon atoms arranged in a square lattice (atom spacing is nm) were used as boundaries of RTIL to block the RTIL, allowing it to transport only through the nanopore from one reservoir to the other. To drive ionic transport, we imposed a voltage drop ϕ across the system by applying a uniform electric field along the pore axis (x-direction) following $E_x = \phi/L_x$, where L_x is the length of simulation box in x-direction. This method has been validated in the studies of ionic transport through various nanopores[49,99]. Note that, although the applied electric field is uniform, electrical potential inside the system conforms to the electrostatic law due to a generation of reaction electric fields[99,100]. The net electrical potential of the ions in the system is the sum of the potential associated with the uniform applied field and the potential due to the reaction electric field. As shown in Figure 3.8, for a given voltage applied across the system, most of the electrical potential drop occurs within the nanopore, and consequently, the net electric forces are much larger for ions inside the nanopores than for ions in the reservoir. Note that, at zero applied voltage drop, the nanopores are wetted by RTILs and this is consistent with the fact that the RTILs studied here can wet nanopores with even smaller diameter (~0.9 nm) [101,102,103].

47

3.1.2 MD system and method for dual-nanopore and dual-reservoir system

Additional simulations based on the dual-nanopore and dual-reservoir method, in which electrostatic potentials in the entire system follow Poisson's equation in a straightforward manner, were performed to ascertain that the ionic transport phenomena observed in the above simulations are independent of the way the voltage drop is applied.
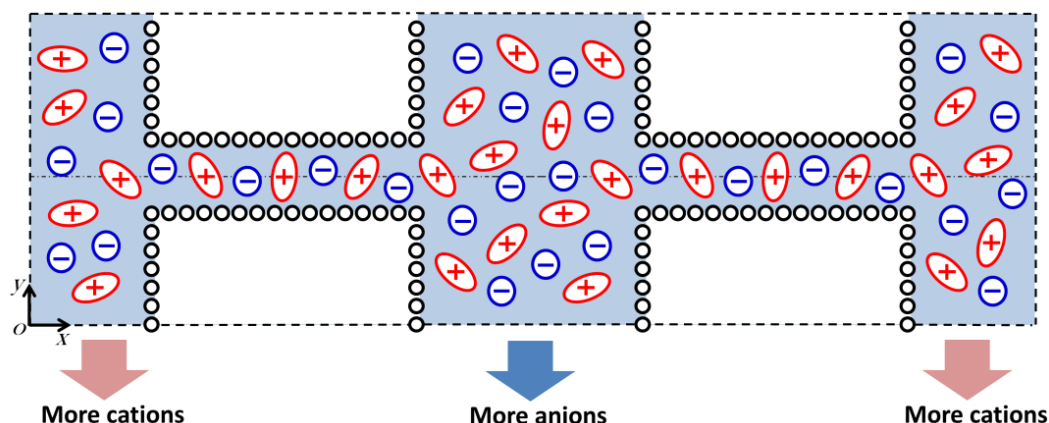
Figure 3.2. A schematic of the dual-pore-dual-reservoir method for imposing a potential difference across a nanopore connected with electrolyte reservoirs. At $t = 0$, a charge imbalance in the two reservoirs is created to generate the desired voltage drop across the nanopores.

To study electrically-driven ionic transport through nanopores connected with an electrolyte reservoir, a voltage drop must be applied across the system. In this work, we used the most straightforward method, i.e., applying a uniform electric field along the pore axis, which has been shown to create an electric field that is consistent with electrostatic laws. Two other methods can also be implemented. In the first method, an electrical potential is imposed on virtual electrodes immersed in the electrolyte reservoirs[104]. Such a method is computationally very intensive since 1) it requires solving an auxiliary Laplace equation over the entire domain during each MD step and 2) ions must be continuously inserted into or removed from electrolyte

48

reservoirs, which is difficult for dense liquids and non-monatomic ions. The second method is the dual-pore and dual-reservoir method[54]. In this method, two identical nanopores and electrolyte reservoirs (see Figure 3.2) are used. An electrical potential difference is created by introducing a charge imbalance in each reservoir, i.e., a net positive charge (an excess of cations) in one reservoir and a net negative charge (an excess of anions) in another reservoir. This method requires modest computational cost. Its key limitation is that, as ionic transport through nanopore progresses, the charge imbalance in each reservoir diminishes and the voltage drop across each nanopore reduces. This limitation makes studying steady ionic transport through nanopore difficult. However, here we use this method to verify that the most essential feature of ionic transport through nanopore filled with RTILs revealed in section 3.2, i.e., partial dewetting of nanopore under large voltage drop across nanopore.

Figure 3.2 shows a schematic of the MD system setup. The length of both nanopores was 10 nm and the length of both RTIL reservoirs was 8 nm. Periodic boundary conditions were applied in all three directions. The choices of RTILs, nanopore and vertical wall atoms are the same as those used in section 3.2. The nanopore walls are charged (σ_s = -0.05 C/m^2). To generate a desired voltage drop across nanopore, we removed N cations in one reservoir and the same amount of anions in another reservoir at $t = 0$. While the entire system is electrically neutral, such a charge imbalance creates a voltage drop through nanopore connecting the two reservoirs. The voltage drop across each nanopore at $t = 0$ is given by

$$V_{t=0} = \frac{NqL_{pore}}{2L_yL_z\epsilon_0} \tag{3.2}$$

where L_{pore} is the length of each nanopore in the x direction, L_y and L_z are the lateral sizes of simulation box in y and z directions, respectively, q is the magnitude of the electric charge of each cation and anion, and ε_0 is the vacuum permittivity.

We present the simulation protocol as the following. We first built the dual-pore-dual-reservoir system sketched in Figure 3.2 without creating a charge imbalance in any of the reservoirs. We next perform an equilibrium run of 2 ns. At the end of this simulation, the number of ions inside each nanopore and reservoir was found to reach their equilibrium values. Following this, we randomly removed N cations from one RTIL reservoir and removed the same number of anions from the other RTIL reservoir to obtain the desired voltage drop according to Equation 3.2. We then performed simulations for another 2 ns to study the ionic transport through nanopore. The beginning of this simulation corresponds to $t = 0$ mentioned above. These simulations were performed for three times with different initial configurations and the results were very close to each other.

3.2 Results and discussions

3.2.1 Single-pore and single-reservoir system

3.2.1.1 Neutral pore

Figure 3.3a shows the I-V curve in the neutral nanopore. For applied voltages $\phi < 2$ V, the ionic current increases nearly linearly with increasing applied voltage and the effective nanopore conductance is small. At higher voltages, the I-V curve becomes highly nonlinear, and the effective nanopore conductance increases sharply. This latter observation is unusual, since nonlinear I-V curves and greater effective conductance at higher applied voltages have been

observed in nanopores, but typically only in charged conical nanopores[105,49] rather than in the neutral and cylindrical nanopore studied here. Another interesting aspect of the ionic transport is that, as the applied voltage increases, the density of RTILs inside the nanopore reduces. As shown in Figure 3.3b, for applied voltages $\phi < 6$ V, the ion density in the central portion of the nanopore (defined here as within 1.0 nm from the middle plane of the nanopore, i.e. $x = 9\text{-}11$ nm in Figure 3.6) initially changes little, but reduces notably as ϕ increases. At $\phi = 10$ V, the ion density inside the pore is ~75% of that at $\phi = 0$ V.
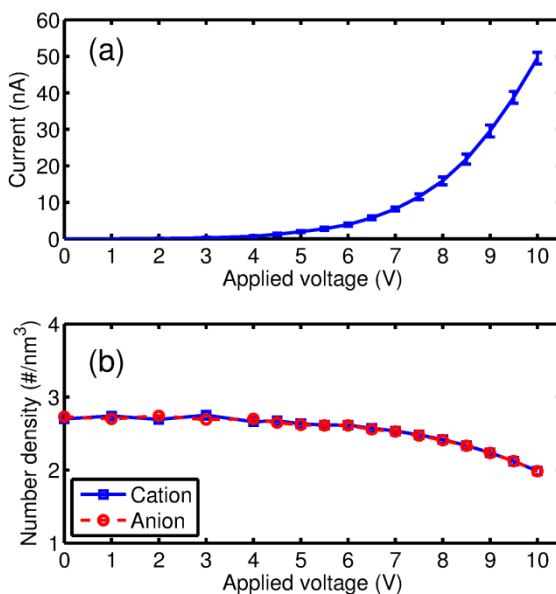
Figure 3.3. Variation of the ionic current (a) and average ion number density in the central portion of the nanopore (b) as a function of the voltage drop across the entire system. The nanopore surface is electrically neutral.

These unusual phenomena originate from the fact that, for RTILs confined in nanopores, under strong electric fields, the ionic conductivity is larger than that of bulk RTILs and it increases with decreasing ion density. To validate this point, we first performed a series of simulations to compute the ionic conductivity of RTILs confined in nanopores with the same size as considered above but periodic along the pore axis. In these simulations, different numbers of

RTIL molecules were placed inside the nanopore so that the average ion density varies from 100% to 80% of that found in Figure 3.3b at zero voltage ($\rho_{ion,\phi=0}$) i.e., from 2.68 #/nm^3 to 2.14 #/nm^3. The method for computing the conductivity of RTILs in a periodic nanopore, together with that for bulk RTILs, in described in Section 3.1 of this chapter. Figure 3.4 shows that, with
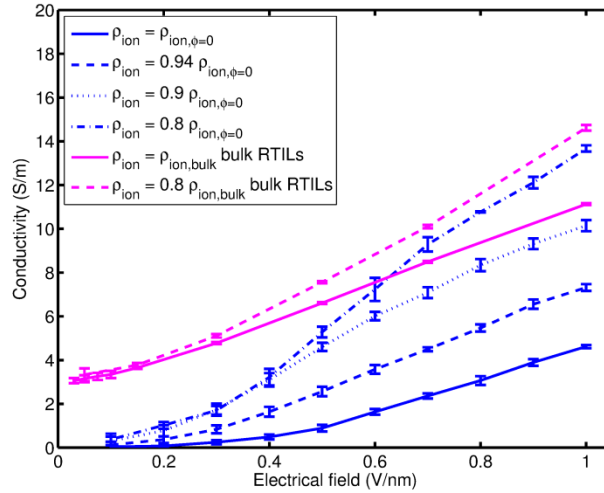
Figure 3.4. Conductivity of bulk RTILs and RTILs confined in neutral periodic nanopores as a function of ion density and strength of the applied electric fields.

the same average ion density, the conductivity of RTILs increases as the electric field E becomes stronger. In fact, when the ion density inside nanopore is the same as $\rho_{ion,\phi=0}$, the conductivity of RTILs confined in the nanopore is smaller than that of bulk RTILs at E=0.1 V/nm but it exceeds the latter when E>0.8V/nm. Note that the comparison is made between the conductivity of the ions in nanopore at 0.8 V/nm and that of ions in the bulk at 0.1 V/nm due to the small voltage drop in the bulk (see Figure 3.8). These behaviors are consistent with the results on the ionic transport of RTILs reported previously. In particular, the weaker conductivity of RTILs in the nanopore at low electric fields compared to that in the bulk is in line with the slower self-diffusion of RTILs in nanopore reported earlier by the Hung group[56,58]; the increase of conductivity as E increases is similar to that has been observed for bulk RTILs.[106] Figure 3.4 also

shows that the conductivity of RTILs increases sharply when the ion density decreases slightly, indicating that the mobility of ions increases greatly with decreasing ion density. This behavior is in marked contrast to that of aqueous electrolytes, in which the mobility of ions increases only slightly as the density decreases. This difference is caused by the solvent-free nature of RTILs. RTILs are dense liquids in which electrical migration of ions is retarded primarily by ion-ion friction originating from the close ion-ion contacts and is facilitated by a transient atomistic cavity within the liquids. As such, the ion mobility increases greatly as the ion density decreases, and diverges as the ion density approaches zero. However, in aqueous electrolytes, the migration of ions is retarded by the surrounding solvent molecules and the ionic cloud around each ion plays a secondary role.

To understand how the dependence of RTIL's electrical conductivity on the strength of electric fields and ion density revealed in Figure 3.4 leads to a decrease of ion occupancy in nanopore as electric field strength increases and the nonlinear I-V curve shown in Figure 3.3., we examined the response of a nanopore/RTIL system (*cf*. Figure 3.1) as a voltage drop is impulsively applied across the system (see Figure 3.5). Once a voltage drop is applied, an electric field is established inside the nanopore. Since the diameter of the nanopore is much smaller than the lateral size of RTIL reservoir and the system is electrically neutral everywhere, most of the potential drop occurs within the nanopore. When a sufficiently large voltage drop is imposed, the electric field inside the nanopore can be strong enough that the ionic conductivity of the RTILs in the nanopore exceeds that of bulk RTILs. For example, immediately after a potential difference of 8 V is imposed across the system, an electric field of ~0.8 V/nm is established inside the nanopore, and the ionic conductivity of RTILs confined inside the

nanopore exceeds that of bulk RTILs (*cf.* Figure 3.4). Because of the different ionic conductivities in the nanopore and in the bulk RTILs, the ionic flux inside the nanopore (in
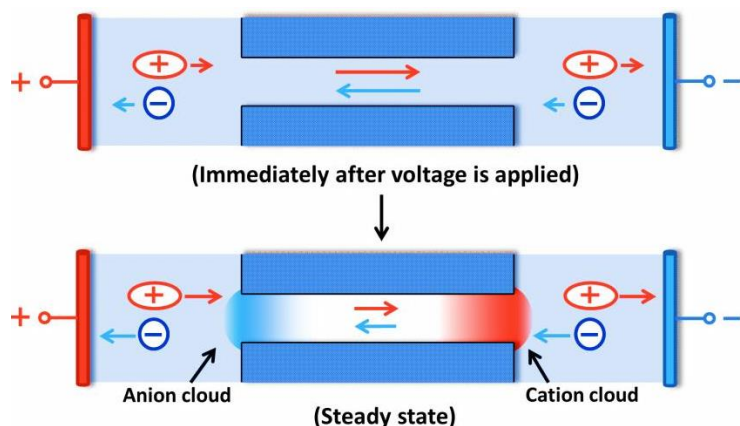
Figure 3.5. A schematic illustrating the mechanism of ion density reduction in a nanopore filled with a RTIL under large applied voltages. The length of arrows indicates the magnitude of ion flux. The formation of charged ionic clouds near pore entrances (red/blue color denotes ionic cloud with positive/negative charges) and the significant increase of RTIL conductivity as ion density decreases are the main reasons for the reduction of ion density in nanopores under strong applied electric fields.

Figure 3.5a, toward the negative electrode for cations and the opposite direction for anions) will be larger than that inside the bulk RTILs. Consequently, cations (anions) start to accumulate near the pore entrance closer to the negative (positive) electrode to form a cation (anion)-rich zone and meanwhile the number of ions inside the nanopore decreases (*cf.* Figure 3.5b). The cation (anion)-rich zone will be termed cationic (anionic) cloud hereafter. Since the number of ions inside the nanopore decreases during this process, the ionic conductivity inside the pore increases (*cf.* Figure 3.4), which further enhances the ionic flux through the nanopore, prompting further growth of ionic clouds near the pore entrances. On the other hand, the formation of ionic clouds near the pore entrances creates an electric field within the nanopore that counteracts the electric field initially established due to the imposed voltage drop. As a result, the strength of the net electric field in the nanopore decreases, which tends to reduce the ionic flux through the

nanopore and to impede the growth of ionic clouds near the pore entrances. These two effects compete with each other until a steady state of ionic transport through the nanopore is established. At steady state, the ion density inside the nanopore will be smaller than its initial value and stationary ionic clouds are established near the pore entrances. To quantify the charge accumulation in the ionic clouds near the pore entrances, we computed the ionic charge density in the shaded region shown in Figure 3.1 at the steady state for an applied potential drop of 10 V. Figure 3.6 shows that, within the nanopore, ionic charge density becomes more positive (negative) as we move toward the pore entrance facing the negative (positive) electrode, thus supporting the accumulation of ionic clouds near the pore entrances suggested above. Within the RTIL reservoir, ionic charge density shows strong oscillations near the pore entrances, consistent with the alternating layering of cation/anions observed ubiquitously for interfacial RTILs[58,59]. The degree of ion depletion inside the pore and the buildup of ionic clouds near the pore entrances at steady state increase rapidly as the applied voltage drop increases. This is because, at higher applied voltages, immediately after the voltage is applied, the ionic conductivity inside the nanopore is higher, making the ionic current through the nanopore stronger and consequently the ion depletion and the buildup of ionic clouds more significant. This explains how the dependence of RTIL's electrical conductivity on the strength of electric fields and ion density presented in Figure 3.4 leads to the decrease of ion occupancy in the nanopore as the applied voltage increases (Figure 3.3b).

To understand the sharp increase of ionic current as applied voltage ϕ increases (*cf.* Figure 3.3a), one can directly analyze the potential drop and ionic conductivity inside nanopore as ϕ increases. However this is not straightforward because the potential drop inside nanopore may not increase monotonically as ϕ increases. This is because, as ϕ increases, more ions
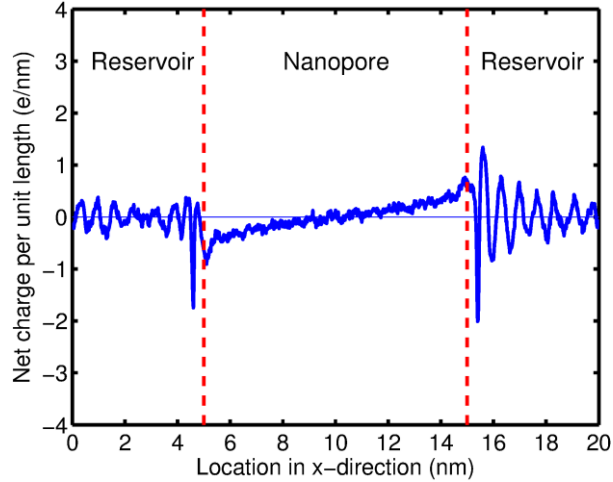
Figure 3.6. Distribution of ionic space charge density along the nanopore axis in the shaded region shown in Figure 3.1. The charge density of nanopore surface is zero. The applied voltage across the nanopore/RTIL reservoir system is 10 V. Distributions of cation and anion density along nanopore axis are shown in Figure 3.9 in Section 3.4.

accumulate inside the ionic clouds near pore entrances and they screen electric fields inside nanopore more significantly, thus lowering the potential drop inside nanopore. Here we adopt a different method, i.e., we analyze how the ionic current from RTIL reservoir to nanopore changes as the applied voltage increases. This method is based on the fact that the steady-state ionic current through nanopore is equal to that from RTIL reservoir to nanopore, which is governed by the potential drop in RTIL reservoir and the ionic conductivity of bulk RTILs. The potential drop in RTIL reservoir is affected by two factors: the applied voltage across the entire nanopore/RTIL reservoir system and, more importantly, the formation of ionic clouds near the pore entrances. Specifically, charges accumulated in the ionic clouds near pore entrances help increase the potential drop inside the RTIL reservoirs. As pointed out above, when the voltage imposed across the entire nanopore/RTIL reservoir system increases, charge accumulation within each ionic cloud near the pore entrance increases sharply. Therefore, as the applied voltage across the system increases, the increase of potential drop inside RTIL reservoir is faster than the

56

increase of potential drop across the entire system, and this in turn leads to the sharp increase of ionic current through the RTIL reservoir. Equivalently, the ionic current in the entire system increases sharply with the applied voltage, as shown in Figure 3.3a.

3.2.1.2 Charged pore

The above discussions suggest that ion depletion in the nanopore and the concomitant sharp increase of ionic current at large voltages are triggered by the high conductivity of RTILs in nanopore at large voltages and sustained by the increase of ionic conductivity as the ions density decreases. Based on these results, we expect that, if the conductivity of the RTILs inside nanopore can be increased and the sharp increase of ionic conductivity as ion density reduces can be achieved, large ionic current through nanopores can be induced and ion depletion can be amplified at lower voltages. Such a situation can in principle be achieved by tailoring the surface and geometrical properties of nanopores and the size/shape of RTIL molecules. In particular, such a situation may be achieved in charged nanopores. In charged nanopores, the density of counter-ions exceeds that of co-ions. Under the action of applied electric fields, the net ionic current is a sum of the migration current due to electrical migration of individual ions and the convective current due to the collective movement of all ions (termed the electroosmotic flow). In narrow nanopores with moderate/high surface charge densities or a smooth surface, the convection current can be much greater than the migration current[107,108]. For the charged nanopore considered here (σ = -0.05 C/m², D=2.17 nm), the ionic conductivity of RTILs inside an isolated nanopore (i.e., the nanopore is periodic along its axis and is not connected with an external RTIL reservoir) is 733 S/m at an applied electric field strength of only 0.001 V/nm and the convection current contributes to ~99.9% of the total ionic conductivity. Figure 3.7a shows
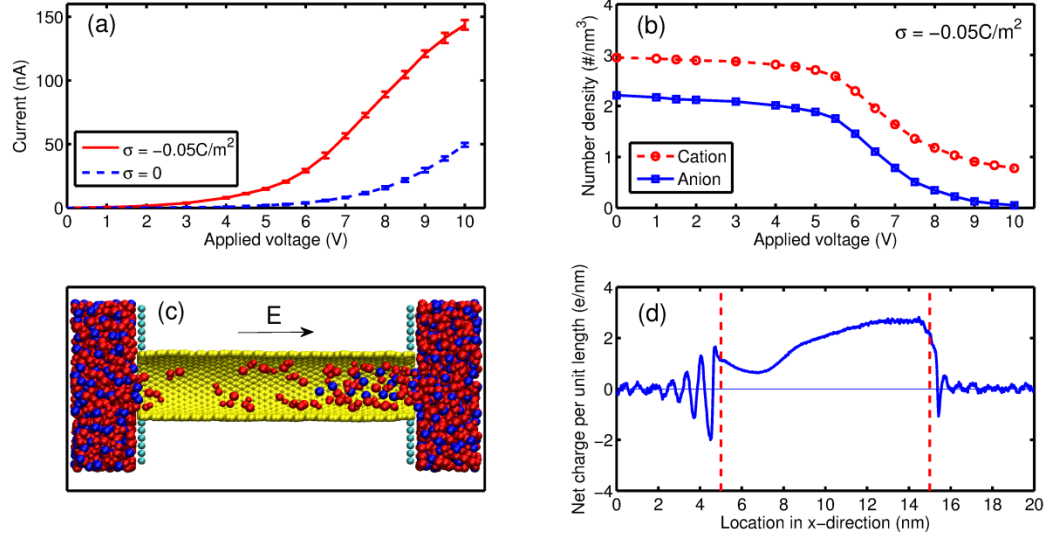
Figure 3.7. (a) I-V relations in charged nanopores (σ=-0.05C/m^2) connected with RTIL reservoirs. (b) Variation of ion density in the central portion of charged nanopore (9 nm < x < 11 nm) as a function of the applied voltage across the nanopore/RTIL reservoir system. (c) A snapshot of the MD system at an applied voltage of 10V. Yellow (cyan) balls denote nanopore (vertical wall) atoms. Red (blue) balls denote cations (anions). (d) Distribution of ionic space charge density along nanopore axis in the shaded region shown in Figure 3.1. Distributions of cation and anion density along nanopore axis are shown in Figure 3.10 in Section 3.4.

the I-V relation for the RTIL going through this charged nanopore when it is connected to a RTIL reservoir. The I-V curve shows essentially the same feature as that in neutral nanopores, i.e., ionic current increases nonlinearly as applied voltage increases, although the magnitude of ionic current is much larger than that in neutral nanopores at any given voltage. Figure 3.7b shows that, at a zero applied voltage, more cations (counter-ions) reside inside the negatively charged nanopore than anions (co-ions). The net charge of ions inside the nanopore is found to balance the charge on the nanopore surface. As the applied voltage increases, the density of both cations and anions in the central portion of the nanopore decreases, but their difference remains nearly the same, which still balances the surface charge on the pore wall. An interesting observation is that at an applied voltage of $\phi = 10$ V, anion's density in the central portion of the

nanopore drops to nearly zero and the cation's density is reduced to ~30% of that at ϕ=0 V, which represents a much stronger ion depletion compared to that in neutral nanopores. The decrease in ion density signifies a gradual dewetting transition inside nanopore as the applied voltage increases. Figure 3.7c shows a snapshot of the MD system at $\phi = 10$ V, and it can be clearly seen that a significant portion of nanopore becomes dewetted. The larger ionic current and stronger ion depletion of ions in charged nanopores compared to neutral nanopores are consistent with our expectations. These phenomena have the same physical origins with similar, albeit less pronounced behavior as observed in neutral nanopores (*cf.* Figure 3.3). For example, as shown in Figure 3.7d, while the ionic space charge density is non-zero everywhere along the pore axis (due to the presence of net surface charge), the space charge density near the pore entrance adjacent to the negative electrode is more positive than that near the pore entrance adjacent to the positive electrode. This confirms the formation of ionic clouds near the pore entrances, which was also observed in neutral nanopores. It is worth noting that the onset voltage drop for observing strongly non-linear I-V curves in both neutral and charged nanopores is smaller than 6 V. Since such onset voltage is comparable to the electrochemical window of RTILs, it helps the experimental realization of the non-linear phenomena observed here.

3.2.1.3 Distribution of electrical potential in nanopore+reservoir system

In the simulations reported here, a uniform electric field was applied to impose a voltage drop across the nanopore+RTIL reservoir system. Specifically, a constant electric force $f_i=q_iE_{\text{ext}}$ is applied on each charge i inside system regardless of its position. However, once charges inside system are subjected to these forces, they redistribute to generate a reaction electric field. The sum of the constant electric force and the force due to reaction electric field produces the final
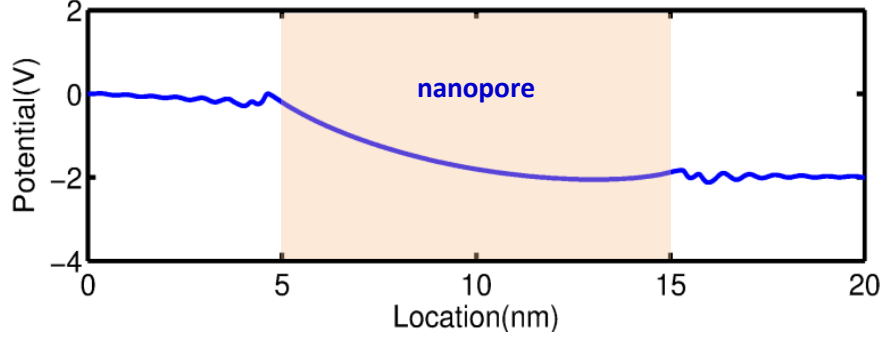
Figure 3.8. Distribution of the average electrical potential inside charged nanopore+RTIL reservoir system as a function of *x*-position. The imposed voltage drop across the entire system is V_{app} = 2 V. The distribution of potential is computed as the sum of the applied potential ϕ_{app} = -*x*/L V_{app} and the reaction potential field ϕ_{re}. The latter is computed by solving Poisson's equation $\nabla^2 \phi_{re} = -\rho_e/\epsilon_0$ (ρ_e: space charge density obtained from MD trajectory, ϵ_0: vacuum permittivity).

electric force exerted on ions and electrical potential distribution inside system. Figure 3.8 shows the average electrical potential profile along the pore axis in the charged nanopore considered here. In this case, the applied voltage drop is 2 V across the nanopore+RTIL reservoir system. We observe that most of the electrical potential drop occurs within the nanopore, due to the fact that nanopore diameter is much smaller than the lateral dimension of the RTIL reservoir. It can be thus expected that the electric force experienced by ions inside the nanopore is much larger than that in the RTIL reservoir, despite that a uniform electric field is applied on all ions inside the system.

3.2.1.4 Ion density distribution inside nanopore+reservoir system

Figure 3.6 in section 3.2 shows distribution of space charge density along the nanopore axis in the shaded region shown in Figure 3.1 (nanopore is neutral and applied voltage is 10V). Figure 3.9 further shows the distribution of cation and anion density along the nanopore axis in the same region. The density of ion in nanopore is lower than that in bulk due to 1) the ion
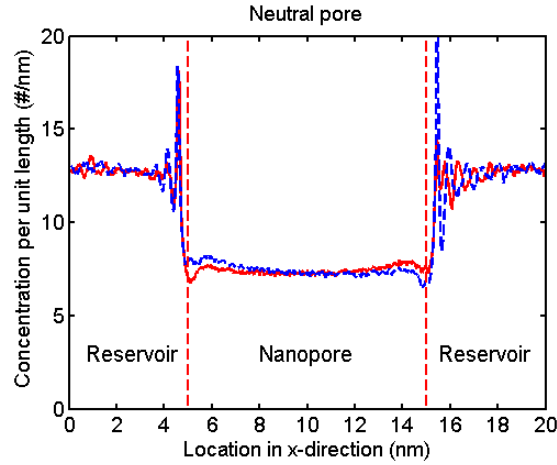
Figure 3.9. Distribution of cation and anion density along the nanopore axis in the shaded region shown in Figure 3.1. The ionic transport conditions are the same as those in Figure 3.6 in section 3.2, where the charge density of nanopore surface is zero. Red line is for cation and blue line is for anion.
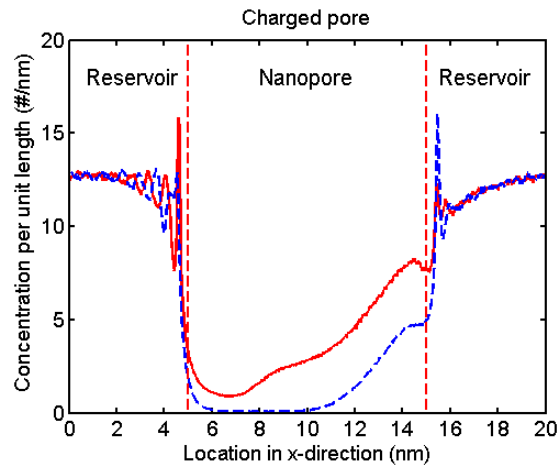
Figure 3.10. Distribution of cation and anion density along the nanopore axis in the shaded region shown in Figure 3.1. The ionic transport conditions are the same as those in Figure 3.7d in section 3.6, where the charge density of nanopore surface is $\sigma = -0.05 C/m^2$. Red line is for cation and blue line is for anion.

depletion phenomena discussed in section 3.2, and 2) the shaded region goes from $r=0$ (pore axis) to R_c (the center of carbon atoms on nanopore surface). Since ions can be found anywhere between $r=0$ and R_c in RTIL reservoirs but not very close to $r=R_c$ in nanopores, the ion density inside pore appears to be smaller. Figure 3.10 shows the cation and anion density profiles along

the nanopore axis in the shaded region shown in Figure 3.1 under ionic transport conditions same as those in Figure 3.7b.

3.2.1.5 Different sensitivity of ionic conductivity on ion density
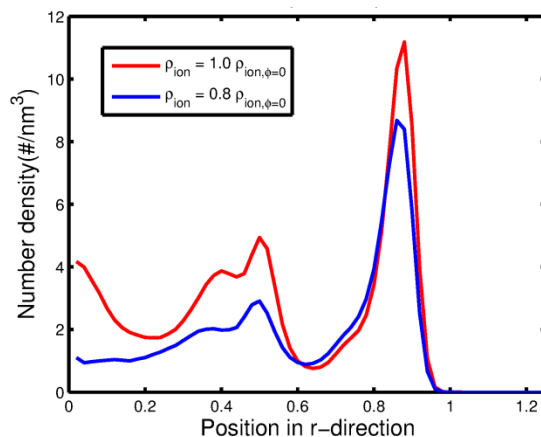
Figure 3.11. Distribution of cations inside the neutral periodic nanopore in radial direction considered in Section 3.2 (access diameter: 2.17nm). Red line indicates the ion density profile when total number of ions inside nanopore is equal to that at zero applied voltage. Blue line indicates the ion density profile when the number of ions inside nanopore was reduced by 20% from its value at zero applied voltage ($\rho_{ion,\phi=0}$).

In Figure 3.4 in Section 3.2, we showed that, as the ion density in nanopore decreases from its equilibrium value at zero applied voltage, the ionic conductivity increases significantly (e.g., at E = 1 V/nm, the ionic conductivity increases by ~ 200% as ion density decreases by 20%). For bulk RTILs, the increase of their ionic conductivity as ion density reduces is weak (e.g., at E = 1 V/nm, the ionic conductivity increases by only ~30%). The different sensitivity of ionic conductivity of bulk RTILs and RTILs in nanopores to ion density can be traced to different response of molecular structure of RTILs to reduction of ion density. For RTILs in bulk, as their density decreases, cavities form within RTILs, and for ions away from the cavities, their local environment (e.g., how each ion is surrounded by other ions) does not change

noticeably because of the strong electrostatic interactions between ions. As such, electro-friction between ions remains high and ionic conductivity does not increase greatly as ion density reduces. For RTILs confined in nanopores, their density is strongly inhomogeneous due to ion-wall interactions. Upon reducing the ion density inside nanopore, the variation of RTIL structure inside nanopore is achieved to a much less extent by forming cavities. Instead, the organization of RTILs across nanopore changes greatly. For example, as shown in Figure 3.11, as the number of cations inside the neutral nanopore considered in section 3.2 reduces by 20%, the number of cations in the core portion of nanopore ($r<0.5$nm) reduces greatly and the first cation density peak also moves away from the pore wall. The former will reduce the electro-friction between ions in the core of nanopore and ions near pore wall, and help increase the conductivity of RTILs in nanopore.

3.2.1.6 Possibility of nonlinear ionic transport phenomena exist in very wide pores

We expect the nonlinear ionic transport phenomena reported in the section 3.2 to occur only in narrow pores. Although in principle higher conductivity of RTILs in nanopore than in reservoir can be achieved in wide pores as long as their diameter is much smaller than reservoir size, the sharp increase of ionic conductivity as ion density reduces, which is necessary to sustain the nonlinear ionic transport phenomena is difficult to achieve in wide nanopores. In wide nanopores, RTILs are bulk like and our calculations (cf. Figure 3.4) indicate that, when the density of bulk RTILs reduces by 20%, their ionic conductivity only increases slightly (the mechanism of this observation is discussed Section 3.5). As such, once the higher ionic conductivity in wide nanopore triggers the formation of ionic clouds near pore ends and the depletion of ions in nanopore, the electric field inside nanopore decreases due to screening of

electric field by the ionic clouds. Since the ionic conductivity only increase slightly as the ion density decreases, the decrease of electric field in nanopore reduces the ionic current through nanopores and halts the growth of ionic clouds and ion depletion in nanopore. Consequently, the nonlinear ionic transport phenomena will be difficult to observe. It is desirable to determine, through direct simulations, the threshold nanopore diameter at which the nonlinear ionic transport disappears. Future studies along this line may be pursued.

3.2.2 Dual-nanopore and dual-reservoir system
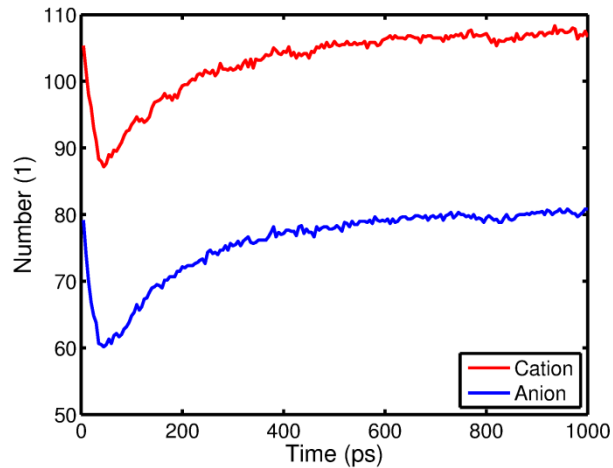
Figure 3.12. Evolution of the number of cations and anions inside each nanopore after an initial voltage drop of 12.6 V was created across the nanopores. The number of cations inside the nanopore is always larger than that of anions because the nanopore is negatively charged.

Figure 3.12 shows the evolution of numbers of cations and anions inside each nanopore as a function of time. The voltage drop across each pore is 12.6 V at $t = 0$ ($t = 0$ is the moment that charge imbalance is created). We observe that, within 50 ps, the number of ions inside each nanopore decreases by ~20-25% compared that at $t = 0$. The decrease of ion occupancy inside nanopore under large voltage drop is qualitatively similar to that observed in the single-nanopore

simulations reported in Section 3.2 and thus confirms the partial dewetting of nanopore under larger voltage drop across nanopore. The key differences are that, the magnitude of decrease is not as significant as those observed in single-nanopore simulations, and at $t > 50$ ps, the number of ions inside the nanopore begins to increase and gradually returns to the equilibrium value. These differences are expected. Immediately after the charge imbalanced was created, the strength of electric field inside nanopore was ~1.2 V/nm. The number of ions inside the nanopore starts to decrease following the mechanism pointed out in Section 3.2 (see Figure 3.5) and ionic clouds build up near pore mouths. However, as ions transport through nanopores, the net charge in each reservoir decreases, which leads to a decrease of the voltage drop across each pair of nanopore+reservoir. As discussed in section 3.2, the magnitude of ionic clouds near nanopore mouths decreases as the voltage drop across nanopore+reservoir system decreases. Consequently, ionic clouds near pore mouths diminish as ion transport progresses and ions from these clouds refill the nanopores.

3.3 System and results by solving PNP equations

In the previous sections, we hypothesized that the sharp increase of ion mobility as the ion density decreases is the essential reason for the electrical field-induced dewetting phenomena. To further validate this hypothesis, we perform continuum simulations using the PNP model to study the electrokinetic transport of RTILs through nanopores. In these simulations, the ion mobility is assumed to increase as the ion density decreases. Generally, the PNP model is rigorously valid only for the transport of dilute electrolytes thus cannot predict the electrokinetic transport of RTILs accurately. However, PNP model can also be considered as a minimal model for ionic transport since it incorporates all modes of ion transport (diffusion,

electrical migration and convection) using the simplest form. If the dewetting and current avalanche phenomena can be predicted by incorporating the ion density-dependent mobility outlined above into such a minimal model, we can be confident that our hypothesis captures the most essential physics underlying these phenomena.

3.3.1. Simulation model
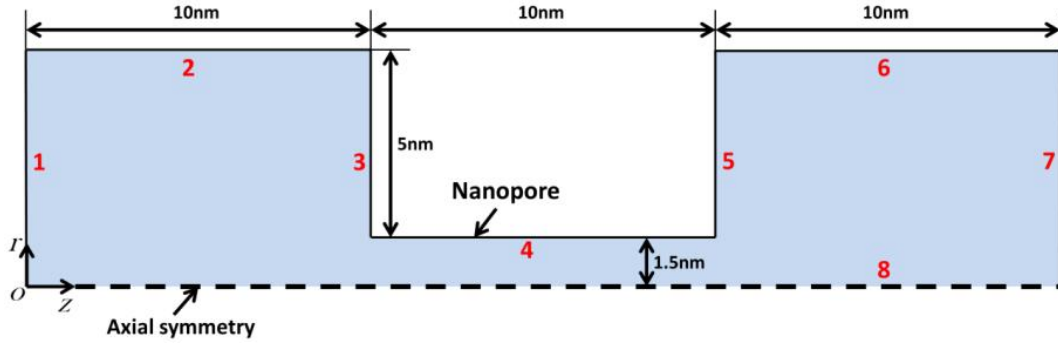
Figure 3.13. The computational domain of the PNP model. The domain is axisymmetric about the dashed line. Each part of the boundary is labeled by a number to facilitate the description in section 3.2.

We adopted the PNP equations given by equations 1.5 and 1.6. We further neglect the convection effects. Therefore, the PNP equations are reduced to the following form:

$$\frac{\partial c_i}{\partial t} + \nabla \cdot \left(-D_i \nabla c_i - z_i u_{m,i} F c_i \nabla v\right) = 0 \tag{3.3}$$

$$-\nabla \cdot (\epsilon_0 \epsilon_r \nabla v) = \rho_q \tag{3.4}$$

where $i = +$ (cation) or $-$ (anion), D is the diffusion coefficient, $z_+ = 1$ and $z_- = -1$, $u_{m,i}$ is the mobility of ion i. F is the Faraday constant; v is the electrical potential; ϵ_0 is the vacuum permittivity; ϵ_r is the relative permittivity and it's 78 in our model; space charge density $\rho_q = (c_+ - c_-)F$. Within the electrolyte reservoir, the diffusion coefficient of both cations and anions are taken as $0.26 \times 10^{-9} \text{m}^2/\text{s}$, and the mobilitiy of both cations and anions are taken as $u_{m,+} =$

$u_{m,-} = 7.8177 \times 10^{-14}\text{s} \cdot \text{mol/kg}$. The diffusion coefficients and ion mobilities of ions inside the nanopore are detailed below.

The 3D cylindrical nanopore-reservoir system is simplified to the 2D-axisymmetric domain shown in Figure 3.13. Zero ionic flux is imposed on boundaries *2, 3, 4, 5 and 6* to model the non-permeating wall; concentration of ions is fixed at $1000\,mol/m^3$ on boundaries *1 and 7*. The initial concentration of both cations and anions is $1000\,mol/m^3$ throughout the domain. Insulation boundary condition is applied on boundaries 2, 3, 4, 5, 6, and 8 for the electrical potential. The electrical potential on boundary *7* is kept at $0V$ and different electrical potentials (V_{app}) are applied on boundary *1* from 0 to $0.6V$ to study the I-V relation.
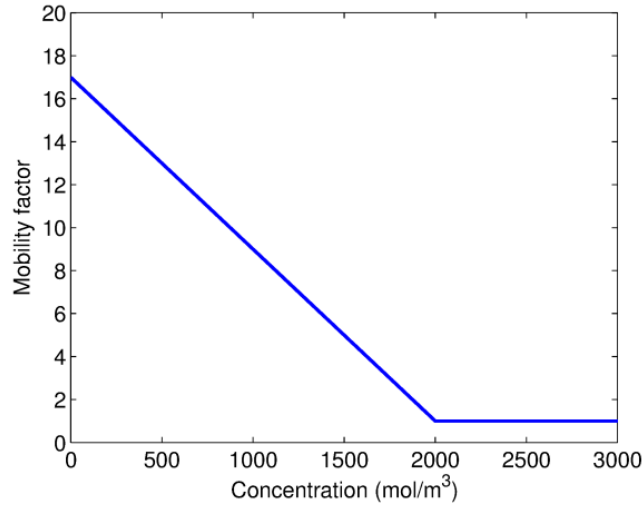
Figure 3.14. The mobility factor $f(c_t)$ used in the PNP model.

The mobilities and diffusion coefficients of ions are modeled as a function of ion concentration only in the pore region. Without loss of generality, we assume that the diffusion coefficient and mobility of ion decrease linearly once the local total ion concentration ($c_t = c_+ + c_-$) becomes lower than $2000\,mol/m^3$. Specifically, we define a mobility factor $f(c_t)$ as below:

$$f(c_t) = k \cdot (c_t - 2c_{bulk}), \ \ if \ c_t \leq 2c_{bulk} \tag{3.5}$$

$$f(c_t) = 1, \ \ if \ c_t > 2c_{bulk} \tag{3.6}$$

where $c_{bulk} = 1000 mol/m^3$ and $k = -0.008$. The mobilities and diffusion coefficients of ions are multiplied by $f(c_t)$ to account for their dependency on the total local ion concentration. Figure 3.14 shows the concentration dependent mobility factor $f(c_t)$. Clearly, other more sophisticated forms of $f(c_t)$ can also be adopted. However, even with the simple form shown in Fig. 3.14, the dewetting and current avalanche phenomena can already be predicted using the PNP model (see below).

3.3.2. Results and discussions
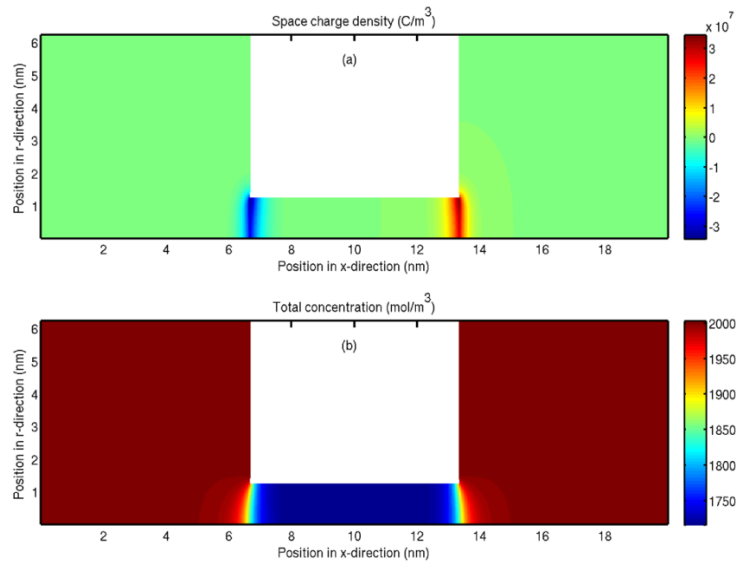
Figure 3.15. The space charge density (a) and total ion concentration distribution (b) in the system. A voltage drop of 0.4V was applied between the two electrolyte reservoirs.

We solved the PNP model with the ion mobilities given by Equations 3.5 and 3.6 using a finite element package Comsol[114,115]. For simplicity, the pore wall is assumed to carry a zero surface charge density. Figure 3.15a shows the ionic space charge density inside the system

68

when a voltage difference of 0.4V was applied between the two electrolyte reservoirs (the direction of electrical field is in the positive direction of z-axis, i.e. it's from left to right). We observe that ionic clouds formed near the two entrances of the nanopore: an anion cloud forms inside the left reservoir and a cation cloud forms inside the right reservoir. The formation of these ionic clouds and their polarity in the two reservoirs are consistent with the MD results shown in previous sections. Figure 3.15(b) further shows that the total ion concentration inside the nanopore is less than the total ion concentration in the reservoir, thus indicating that the partial ion depletion phenomenon can be recovered using the simplistic PNP model adopted here.
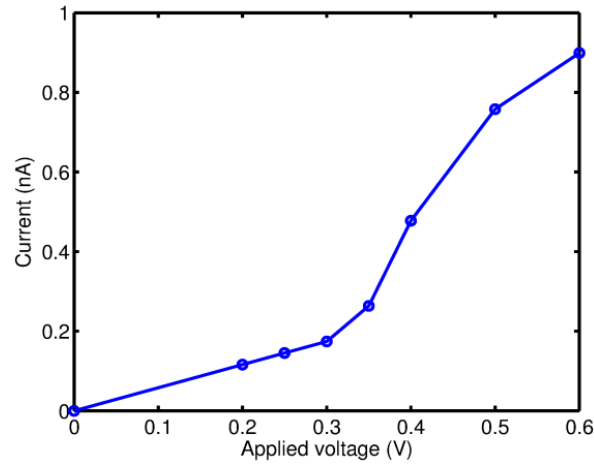
Figure 3.16. I-V relationship calculated from the PNP model and concentration dependent mobilities and diffusion coefficients given by Equations 3.5 and 3.6. The onset of the nonlinear current-voltage relation at ~0.3V roughly corresponds to the onset of the partial ion depletion phenomenon shown in Figure 3.15.

Figure 3.16 shows the current-voltage relation predicted by the PNP model. We observed that while the current increases rather linearly with increasing voltage for $V_{app}<0.3V$, the current increases sharply as the applied voltage increases further. The sharp increase of ionic current at high voltage observed here closely resembles that obtained in our MD simulations, hence lending

support to our hypothesis that the increase of ion mobility due to decrease of ion density causes the dewetting and current avalanche phenomena.

3.4 Conclusions

In summary, electric field driven ionic transport of RTILs through nanopores was studied using atomistic and continuum simulations. As the applied voltage increases, the ionic current through the nanopore increases sharply while the ion density inside the nanopore decreases. These unusual phenomena are synergistic results of the unique property of RTILs (ionic conductivity increases as ion density decreases, which originates from the solvent-free nature of RTILs and the fundamental role of ion-ion friction in controlling electrical ion migration in RTILs) and the far-from equilibrium operation of ionic transport explored here (e.g., formation of stable ionic clouds near the pore entrances under large applied voltages). As a proof-of-concept, we only explored the manipulation of these phenomena by tailoring the surface charge of the nanopores. However, manipulating these phenomena by tailoring other properties of nanopores and RTIL molecules can also be a good strategy. In particular, it should be possible to amplify these phenomena through careful selection of nanopores or RTIL molecules with size/shape optimized for a given nanopore. These strategies will benefit from the recent progresses in fabricating nanopores with different sizes and surface functionalization and from the vast diversity of RTILs that potentially can be synthesized. Examining these strategies will help guide rational selection of nanopores and RTILs to harness these phenomena in practical applications.

The highly nonlinear ionic transport of RTILs through nanopores shown here and its variants (e.g., ionic transport through nanopores with discontinuous surface charge densities[109])

can be implemented in solid-state nanopores for applications such as naonfluidic circuitry[109] and nanopore analytics[49]. In particular, it could provide new ways of improving sensing and detection of molecules using nanopores. Specifically, in nanopore-based sensing, the passage of molecules through a nanopore causes changes in ionic current or other measurable electrical quantities, and such a change is used for molecular sensing. Present nanopore analytics based on aqueous electrolytes works best for charged and hydrophilic molecules or nanoparticles but face considerable challenges when hydrophobic molecules, which have limited stability in aqueous electrolytes, must be analyzed. Recent experiments demonstrated that molecules with different levels of hydrophobicity can be solvated using RTILs[110]. Such solvation capability of RTILs, along with the other unique advantages of RTILs such as non-volatility, helps expand the applicability of nanopore analytics to broader classes of molecules and to enhance the performance.

CHAPTER 4

Dynamics of electrical double layer formation in RTILs

In this chapter, we present detailed MD simulation results on the formation dynamics of an EDL inside an electrochemical cell featuring RTILs enclosed between two planar electrodes. Under relatively small charging currents, the evolution of cell potential during charging can be suitably predicted by the Landau-Ginzburg-type continuum model proposed recently (M. Z. Bazant, B. D. Storey, and A. A. Kornyshev, *Phys. Rev. Lett.*, **106**, 046102, 2011). Under very large charging currents, the cell potential shows pronounced oscillation during the initial stage of charging, a feature not captured by the continuum model. Such oscillation originates from the sequential growth of the ionic space charge layers near the electrode surface, allowing the evolution of EDLs in RTILs with time, an atomistic process difficult to visualize experimentally, to be studied by analyzing the cell potential under constant current charging conditions. While the continuum model cannot predict the potential oscillation under such far-from-equilibrium charging conditions, it can nevertheless qualitatively capture the growth of cell potential during the later stage of charging. Improving the continuum model by introducing frequency-dependent dielectric constant and density-dependent ion diffusion coefficients may help to further extend the applicability of the model. The evolution of ion density profiles is also compared between the MD and the continuum model, showing good agreement.

4.1 Simulation systems and methods

The MD model for the electrochemical cell consists of two parallel walls and the RTIL electrolyte enclosed in between (Figure 4.1). The separation between the two walls is 30 nm, which is wide enough to ensure a bulk-like RTIL behavior in the middle of the system. The force
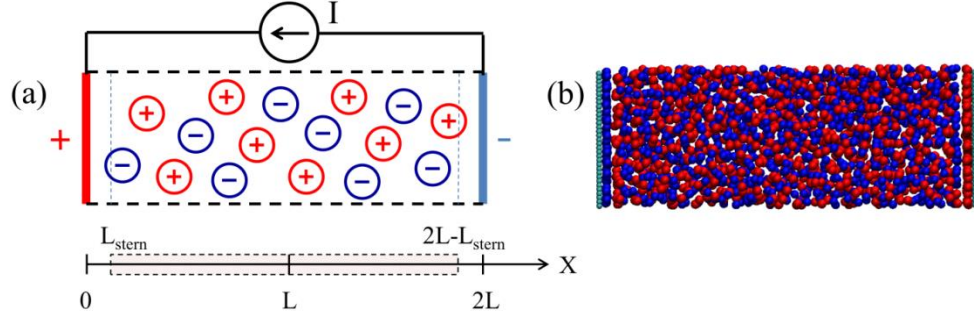
Figure 4.1. (a) Schematic of MD (top) and continuum model (bottom) used for studying the formation of EDLs at the interface of planar electrodes and RTILs. The electrical potential at $x = 0$ is taken as zero. The horizontal dashed lines in the top panel denote periodic boundaries of the MD system. (b) A snapshot of the MD system, where the blue and red spheres represent anions and cations, respectively.

fields for the wall atoms and RTILs are the same as those adopted in Ref. 29. Briefly, each wall

is made of Lennard-Jones (LJ) spheres arranged in a square lattice with a lattice spacing of 0.33

nm. The ions are modeled as a generic RTIL without molecular details. Cations and anions of the

RTIL electrolyte are symmetrical LJ spheres of 0.5 nm in radius with unit charge. The setup and

the identical cation/anion radii lead to a symmetrical capacitor. The non-electrostatic interactions

within the system are described by $u_{LJ}(r) = \frac{C_{12}}{r^{12}}$ [29],where r is the distance between two atoms. At

a temperature of T = 450 K, the LJ parameters are C_{12} = 3.742 kJ/mol·nm for ion-ion interactions

and 9.931×10^{-3} kJ/mol·nm for ion-wall interactions[29]. A background dielectric constant of 2.0 is

used in the calculations of electrostatic interactions to account for the electronic polarizability of

ions not explicitly modeled in the force fields. We adopt this minimal model for RTILs because

it has been shown to successfully capture the key features of EDLs revealed by simulations

based on more sophisticated RTIL models[29]. The number of cation-anion pairs for the RTIL

electrolyte is tuned so that the cation/anion concentration in the cell center is 0.5 M at zero wall

charge conditions.

Simulations are performed in the NVT (T = 450 K) ensemble using the Gromacs package.[71] A time step of 5 fs is used. Further details of the MD technique, such as the calculations of electrostatic interactions and thermostating, can be found in our prior work on electrokinetic transport in RTILs[30]. Using the setup and force fields given above, we were able to accurately reproduce the capacitance-voltage (C-V) relation of EDLs under the equilibrium conditions reported in Ref. 29. To simulate the formation of EDLs at the electrode/electrolyte interface under constant-current charging conditions, we first equilibrate the system with zero wall charge for 100 ns. At $t > 0$, we continuously add (remove) a small partial charge on each atom of the positive (negative) electrode wall until the absolute value of the surface charge density of both walls reaches 0.09 C/m^2. The rate at which the partial charge was added to (removed from) the positive (negative) wall atoms was varied to obtain five charging current densities: I = 25, 50, 100, 200 and 400 kA/cm^2. We note that these current densities are several orders of magnitude larger than that found in typical experimental systems[111,112] because the spacing between the two charged walls is small and the diffusion coefficient of the model RTILs used here is large (see below). During simulations, the number densities of cations and anions across the cell are recorded every 1, 0.5, 0.25, 0.125 and 0.075 ps for the five different charging rates, respectively. To obtain reliable statistics, each charging case is repeated 100 times with independent initial configurations. The potential distribution across the entire cell is then calculated using the following equation derived from Poisson's equation[113]

$$\phi(x) = \frac{s}{\epsilon_0 \epsilon_r} x - \frac{1}{\epsilon_0 \epsilon_r} \int_0^x (x - y) \rho_e(y) dy \tag{4.1}$$

where ϕ is the electrical potential, s is the wall charge density, x is the distance from the geometrical plane of the left wall ($x = 0$), ϵ_0 is the vacuum permittivity, ϵ_r is the background dielectric constant used in the RTIL model, and ρ_e is the ionic space charge density. As indicated

74

in Figure 4.1, the left wall is the positive electrode of the electrochemical cell, with its potential taken as zero.

Continuum simulations. Based on the BSK model developed in Ref. 37, the dynamics of EDL formation in the above system can be described by the following equations:

$$\frac{\partial C_{\pm}}{\partial t} = D_{\pm} \frac{\partial}{\partial x}\left(\frac{\partial C_{\pm}}{\partial x} \pm \frac{F}{RT}C_{\pm}\frac{\partial \phi}{\partial x} + \frac{\gamma C_{\pm}}{1-\gamma(C_+ + C_-)}\frac{\partial(C_+ + C_-)}{\partial x}\right) \tag{4.2}$$

$$\epsilon_0 \epsilon_{bulk}\left(l_c^2 \frac{\partial^2}{\partial x^2} - 1\right)\frac{\partial^2 \phi}{\partial x^2} = F(C_+ - C_-) \tag{4.3}$$

where $C_{\pm}$ are the cation/anion concentrations, R is the ideal gas constant, F is the Faraday constant, T is temperature, γ is the minimum volume available in space for ions, $D_{\pm}$ is the ion diffusion coefficient, ϵ_{bulk} is the permittivity of bulk RTILs, and l_c is the electrostatic correlation length. An ion-free Stern layer with a thickness of L_{stern} and a dielectric constant of ϵ_{stern} are also included near both walls (see Figure 4.1). To facilitate the comparison of the predictions by the BSK model with those by the MD simulations, the BSK model is parameterized using the properties of the model RTILs described above. Part of such a parameterization has been performed in Ref. 39, and the results are as follows: $L_{stern} = 0.5$ nm, $\gamma = 0.83$ nm^3, $l_c = 1.33$ nm, $\epsilon_{bulk} = \epsilon_{stern} = 5$. To determine the diffusion coefficient of cation and anion, we perform independent simulations to compute the electrical mobility of ions by applying uniform electric fields to bulk RTILs. Next, the diffusion coefficient of ions is obtained by using the Einstein relation between diffusion coefficient and electrical mobility. This method is consistent with the fact that the Einstein relation is assumed in Equation 4.2. Using this method, $D_+ = D_- = 1.68 \times 10^{-8}$ m^2/s was obtained. Such a diffusion coefficient is three to four orders of magnitude larger than that of typical bulk RTILs due to the spherical geometry of the RTIL model and the high temperature adopted here. Because of this large ion diffusion

coefficient, the formation and relaxation of EDLs is fast. As such, it enables nearly quasi-equilibrium formation of EDLs to be simulated at a charging rate much larger than that in practical systems (e.g., I = 400 kA/cm^2, cf. Figure 4.6b), which facilitates the comparison with EDL formation under non-equilibrium charging conditions.

Equation 4.2 is complemented by a zero-ion flux boundary condition for the ions at $x = 0$ and 2L. For Equation 4.3, the third derivative of the electrical potential is set to zero at $x = 0$ and 2L; the first derivative of the electrical potential at $x = 0$ and 2L is treated as a time dependent function which represents the steady increase of the wall charge density due to constant-current charging:

$$\left.\frac{\partial \phi}{\partial x}\right|_{x=0} = \frac{-I \cdot t}{\epsilon_0 \epsilon_{bulk}} \; ; \left.\frac{\partial \phi}{\partial x}\right|_{x=2L} = \frac{I \cdot t}{\epsilon_0 \epsilon_{bulk}} \tag{4.4}$$

where I is the current density (kA/m^2). At $t = 0$, $C_+ = C_- = 0.5$ M and $\phi = 0\,V$ throughout the domain. These equations were solved using a commercial finite element package Comsol[114,115]. Nonuniform elements are implemented in order to better resolve EDLs near walls while minimizing the computational cost. Mesh sizes are reduced several times to ensure the results are mesh-independent. As in the MD simulations, five different constant charging current densities are used to study the dynamics of EDL formation.

4.2 MD results and discussions

We first examine the dynamics of EDL formations in the RTIL electrolyte using the MD method described in Section 4.1. Figure 4.2 shows the evolutions of the potential drop across the entire cell as a function of the wall charge density under constant-current charging at different rates. At the highest charging rate (I = 400 kA/cm^2), the potential drop increases sharply as the
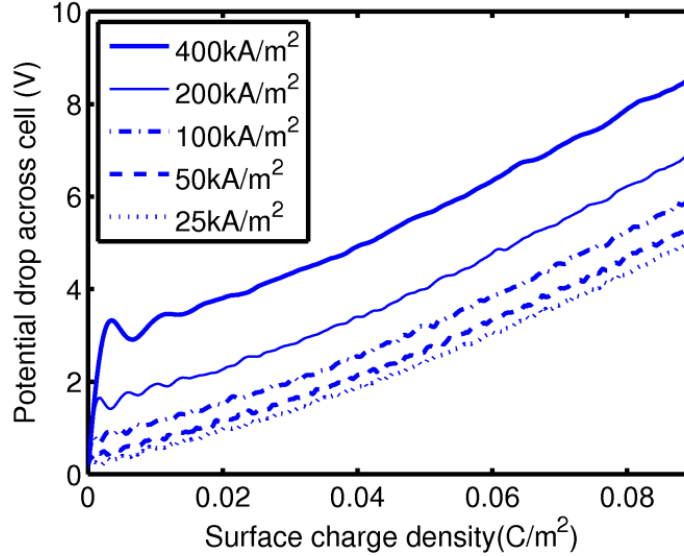
Figure 4.2. Evolution of the potential drop across the entire electrochemical cell (*cf*. Figure 4.1) as a function of the wall charge density during constant-current charging at different charging rates.

wall charge density increases and oscillates significantly until the wall charge density reaches ~0.02 C/m^2. Afterward, the potential drop increases rather linearly with the wall charge density, and the weak curvature of the voltage-charge curve is closely related to the fact that the differential capacitance of double layers in RTILs depends on the surface charge density of the electrodes. At lower charging rates, the oscillation of potential drop across the cell initiates at lower wall charge densities and the amplitude is reduced with respect to that of 400 kA/cm^2. For any given wall charge density, the potential drop across the cell increases with increasing charging current, which is expected because higher charging current leads to larger ionic current and IR drop across the RTILs (Ohmic loss), and thus larger voltage drop across the entire cell. These theoretical evolutions of potential drop bear a close resemblance to the charging branch of the galvanostatic charge/discharge profiles of supercapacitors utilizing RTILs as electrolytes, where the voltage plotted versus time shows linear slopes indicating a capacitive behavior[111,116].

We also note that the system has negative dynamic differential capacitance due to potential oscillations.

To understand the physical origins of the potential oscillation shown in Figure 4.2, we examine the potential drop across half of the cell ϕ_{hc}, i.e., that from the left wall to the cell center. Note that ϕ_{hc} is 1/2 of the total potential drop across the entire cell due to the symmetries of the cell geometry and ion models used here. Using Equation 4.1, the rate at which the half-cell potential drop ϕ_{hc} changes under a constant-current charging condition is given by

$$\frac{\partial \phi_{hc}}{\partial t} = \frac{\partial \phi_{wc}}{\partial t} + \frac{\partial \phi_{ic}}{\partial t} \tag{4.5a}$$

$$\frac{\partial \phi_{wc}}{\partial t} = \frac{I \cdot L}{\varepsilon_0 \epsilon_r} \tag{4.5b}$$

$$\frac{\partial \phi_{ic}}{\partial t} = -\frac{1}{\varepsilon_0 \epsilon_r} \frac{\partial \int_0^L (L-s)\rho_e(s)ds}{\partial t} \tag{4.5c}$$

in Equation 4.5a, $\partial \phi_{wc}/\partial t$ and $\partial \phi_{ic}/\partial t$ represent the contributions from the accumulation of surface charge on the wall and from the formation of ionic space charge layers (i.e., EDLs) inside the RTILs, respectively. Note that $\partial \phi_{wc}/\partial t$ is a constant determined by the charging rate in the constant-current charging. Figure 4.3a shows the temporal evolution of ϕ_{hc} while Figure 4.3b shows the contributions to ϕ_{hc} from the two components of $\partial \phi_{wc}/\partial t$ and $\partial \phi_{ic}/\partial t$. Figure 4.3b indicates that the oscillation of the half-cell potential drop is driven by the dynamic formation of ionic space charge layers inside RTILs: ϕ_{hc} increases (decreases) $\partial \phi_{ic}/\partial t$ is smaller (larger) than $\partial \phi_{wc}/\partial t$, and ϕ_{hc} reaches a peak (or valley) whenever $\partial \phi_{ic}/\partial t$ becomes equal to $\partial \phi_{wc}/\partial t$. More specifically, for $t < 1.24$ ps, $\partial \phi_{ic}/\partial t$ increases rapidly and exceeds $\partial \phi_{wc}/\partial t$ at $t = 0.91$ ps and this leads to the first peak of ϕ_{hc}. Between $t = 1.24$ ps and 2.21 ps, $\partial \phi_{ic}/\partial t$ decreases and crosses over $\partial \phi_{wc}/\partial t$ at $t = 1.63$ ps, leading to the first valley of ϕ_{hc}. At

later times, $\partial\phi_{ic}/\partial t$ still oscillates but with a reduced amplitude. As such, the oscillation of ϕ_{hc} becomes weaker with time and practically disappears at $t > 6$ ps.
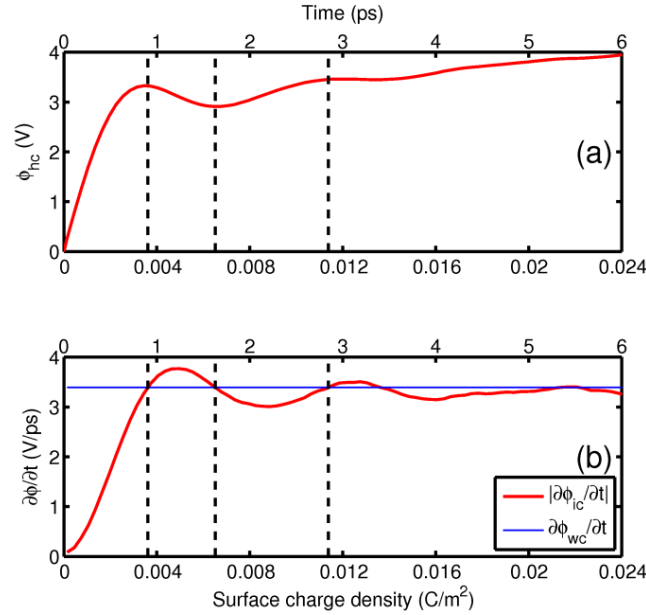
Figure 4.3. Evolution of the potential drop across a half-cell under the largest charging current studied (I = 400 kA/cm²). (a) Temporal evolution of the half-cell potential drop (ϕ_{hc}); (b) Contributions from the wall charge ($\partial\phi_{wc}/\partial t$, horizontal blue line) and the ionic space charge ($\partial\phi_{ic}/\partial t$, red curve) to the half-cell potential drop. Since $\partial\phi_{ic}/\partial t$ is always negative, its absolute value is shown here to facilitate comparison with $\partial\phi_{wc}/\partial t$. The vertical dashed lines denote the time when ϕ_{hc} reaches a peak (or valley) or equivalently when $\partial\phi_{wc}/\partial t$ is equal to $\partial\phi_{ic}/\partial t$.

The above results indicate that the formation of ionic space charge layers (or equivalently, EDLs) inside the cell during charging is responsible for the oscillation of the potential drop across the cell observed in Figure 4.2. To further rationalize how the formation of EDLs leads to the potential oscillation, we divide the space between the left wall and the middle plane of the cell into several layers: the first and the second layers (0 nm $< x <$ 0.93 nm and 0.93 nm $< x <$ 1.67 nm) correspond to the space occupied by the first counter-ion (anion) and co-ion (cation) layers adjacent to the left wall, respectively. The third layer (1.67 nm $< x <$ 2.31 nm)

79

corresponds to the space occupied by the second layer of counter-ions near the wall. Since the alternating layering of counter-ions and co-ions is no longer strong beyond the second counter-ion peak, the space between $x = 2.31$ and 15 nm is taken as the fourth layer. It is worth noting that the locations of the counter-ion and co-ion layers adjacent to the wall will change during the charging process. However, such a change is relatively small during the time when potential oscillations are observed, and therefore we adopt a static partition of the ionic layers inside the cell. Figure 4.4a shows the evolution of the net charge in each of these layers and Figures. 4.4b-d show the detailed evolution of the cation density, anion density, space charge density, and total ion density profiles during the first 6 ps of charging. We observe that the net charge grows noticeably only in the first layer at short times ($t < {\sim}0.9$ ps). The growth of the first layer is followed by the second, the third, and the fourth layers at successively later times.

Using the data on the growth of charge inside each layer shown in Figures 4.4a-c and Equation 5c, we compute how the sequential growth of all these layers contributes to the evolution of $\partial\phi_{ic}/\partial t$ with time. Figure 4.5a shows that, for $t < {\sim}1$ ps, if we include only the charge in the first space charge layer in ρ_e when evaluating Equation 5c, the computed $\partial\phi_{ic}/\partial t$ is close to the result in which all space charge layers are included in ρ_e when evaluating Equation 5c. This indicates that, for $t < {\sim}1$ ps, the growth of ϕ_{ic} is governed mostly by the growth of the first space charge layer (blue solid curve in Figure 4.5a) and its competition with the growth of ϕ_{wc} due to the steady increase of wall charge density (solid black line in Figure 4.5a) leads to the first potential peak observed at $t \approx 0.9$ ps. Such an observation is expected because, by $t \sim 1$ ps, only the first space charge layer grows notably (i.e., has significant charge accumulation). Figure 4.5a also shows that at $t > {\sim}1$ ps, the growth of the first space charge layer
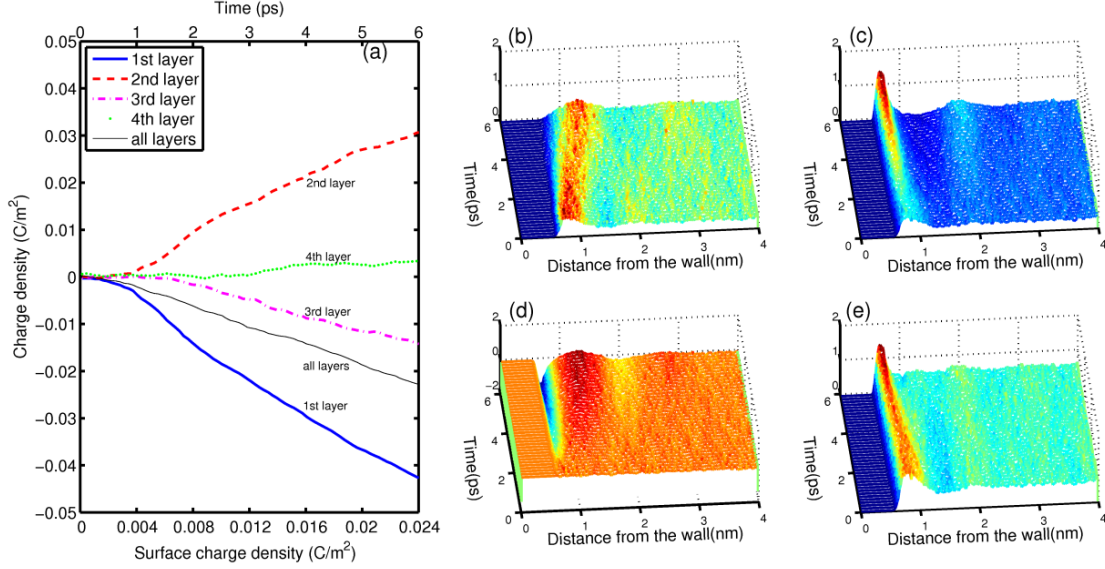
Figure 4.4. (a) Evolution of the net ionic space charge in the four layers defined in text during the initial stage of charging. (b), (c), (d), and (e) Evolution of the cation number density, anion number density, space charge density, and total number density, respectively, during the constant-current charging. I = 400 kA/cm² in all cases.

contributes much more greatly to the variation of ϕ_{hc} than the growth of the wall charge. However, as can be seen from Figure 4.5b, while the growth of the first space charge layer tends to slow down the increase of ϕ_{hc}, its impact is strongly reduced by the growth of the second space charge layer. In fact, when the net charge in both layers are considered, $\partial\phi_{ic}/\partial t$ (thus $\partial\phi_{hc}/\partial t$) is small and even becomes smaller than $\partial\phi_{wc}/\partial t$ at $t \approx 1.46$ ps, which in turn leads to the first valley of the ϕ_{hc} at $t \approx 1.63$ ps. Such a result is consistent with the fact that, at $t > 0.9$ ps, the second space charge layer near the wall starts to grow rapidly (see Figure 4.4a). Because the net charge in this layer is opposite to that in the first space charge layer, the growth of this layer counteracts the suppression effect on the growth of ϕ_{hc} due to the growth of the first space charge layer. Figure 4.5b shows that at $t > 1.63$ ps, the simultaneous growth of the first and the second charge layers tend to greatly enhance the growth of ϕ_{hc} (see blue line in Figure 4.5b).

81
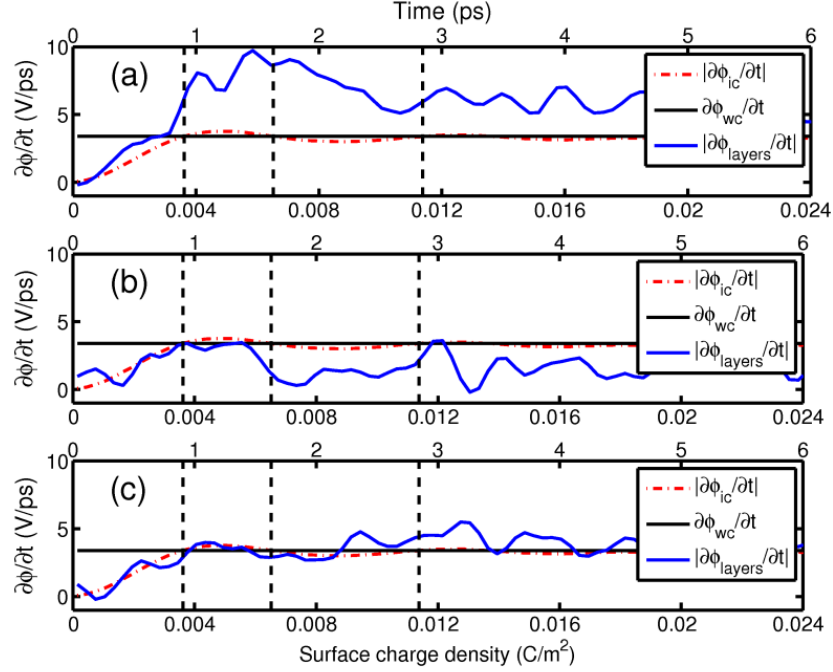
Figure 4.5. The evolution of $|\partial\phi_{ic}/\partial t|$ and how the growth of various space charge layers adjacent to wall contributes to it. Both $\partial\phi_{ic}/\partial t$ and $\partial\phi_{layers}/\partial t$ are negative, their absolute values are shown here to facilitate comparison with $\partial\phi_{wc}/\partial t$ (black solid line). The red dotted dashed curve denotes the contribution due to the space charge in all layers and blue solid curve represents potential due to the net charge in several layers (a: the first layer only; b: the first two layers; c: the first three layers). The vertical black dashed line represents the time at which ϕ_{hc} reaches peak or valley. The charging current is I = 400 kA/cm².

However, as shown in Figure 4.5c, their effects are counteracted by the growth of the third space charge layer near wall, which has a net charge opposite to that in the second space charge layer. While the large statistical noise in Figure 4.5c prevents a conclusive determination of the origin of the second peak of ϕ_{hc} at $t \approx 2.84$ ps, it should be closely related to the significant growth of the third charge layer by this time. From Figure 4.2, we also observe that there are more potential oscillations in smaller charging current cases, such as I = 200 kA/cm². This can be explained by the sequential formation of EDLs. During constant-current charging, the total charges on the wall

at any given time is smaller for smaller current than that for higher current, then the formation of layers further away from the wall, such as 4th and 5th layers, becomes more important in affecting the total potential drop in smaller charging current cases since the charges in those layers are more comparable to total charges on the wall.

The above analysis shows that the sequential formation of the space charge layers with net charge of alternating signs causes the oscillation of the half-cell potential shown in Figure 4.2. The origins of the sequential formation of the space charge layers near the wall can be understood as follows. Immediately after a constant current is imposed on the wall, the surface charge density on the walls starts to increase, creating an electric field across the cell to drive counter-ions (co-ions) toward (away from) each wall. Since the wall prevents penetration of counter-ions into them, counter-ions accumulate near the wall and thus the first space charge layer grows first. With the lapse of time, the number of counter-ions inside the first layer increases more rapidly as the wall charge becomes larger (due to the constant-current charging). At $t \sim 0.8$ ps in the fastest charging case (I = 400kA/cm^2), the rate at which the net charge inside the first layer increases becomes faster than that on electrode walls. This phenomenon is analogous to the charge over-screening phenomenon in equilibrium EDLs and can be termed "dynamic" over-screening. Because of this effect, co-ions are now attracted strongly toward the wall and the growth of the second space charge layer becomes prominent. Since the electrode walls are still being charged constantly, both the first and the second space charge layers continue to grow. In a similar manner, the third space charge layer starts to grow significantly when the second space charge layer "dynamically" over-screens the charge on the wall and inside the first space charge layer. Such a process is repeated in subsequent layers but becomes weaker as each additional layer is located farther away from the electrode wall.

4.3. Comparison between MD and continuum simulation results

In order to test the accuracy of BSK model for non-equilibrium dynamics of RTILs, we also investigated the formation of EDLs under constant-current charging conditions using the continuum simulation approach described in Section 4.1. Figure 4.6a shows that, at a current density of $I = 25$ kA/cm^2, the potential evolution predicted by the MD and BSK models are in good agreement up to a relatively high wall charge density of ~0.07 C/m^2, suggesting that the BSK model can be used to quantitatively predict the formation of EDLs. This is quite encouraging as it opens the possibility of studying the charging dynamics in large systems using continuum simulations, which can be orders of magnitude faster than MD simulations. We also observe that the potential-surface charge relation obtained under such a current density already approaches that at equilibrium conditions, which, as explained in Section 4.1, is caused by the fast diffusion of the model RTILs in our MD simulations.

Figure 4.6b compares the predictions of the potential drop across the entire cell by the MD and BSK models at the largest current density studied, i.e., $I = 400$ kA/cm^2. The BSK model cannot predict the fast rise of potential drop across the cell at the initial stage of charging as well as the potential oscillation until the surface charge density of electrode wall reaches ~0.02 C/m^2. These difficulties most likely originate from the fact that the BSK model is parameterized to reproduce the structure and capacitance of the EDLs under equilibrium conditions and thus may not perform very well when the EDLs near the electrode wall are driven far from equilibrium, as is the present case under a very large charging current. For example, a dielectric constant of 5 was used in the parameterized BSK model. As clarified earlier, ionic polarization, i.e., the polarization due to relative displacements of oppositely charged ion pairs, contributes

significantly to the overall dielectric screening both in bulk RTILs[117] and in EDLs[33]. When EDL

formation is driven by a very large charging current, significant accumulation of net charge in

space charge layers near the wall occurs at a time scale comparable to the time scale that an ion
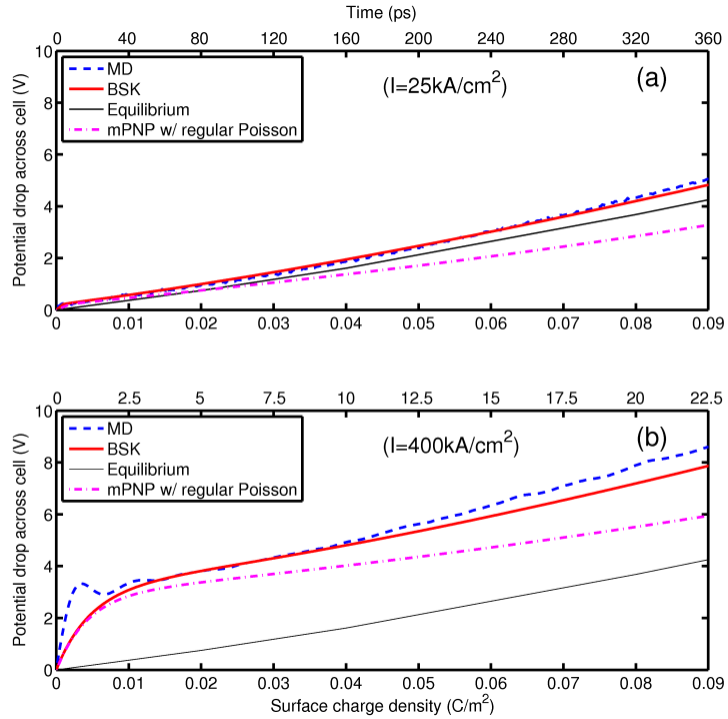
Figure 4.6. Evolution of potential drop across entire cell predicted by MD, the BSK model, and a modified PNP model with zero electrostatic correlation length (panel a: I = 25 kA/cm^2, panel b: I = 400 kA/cm^2). The equilibrium potential drop corresponding to various surface charge densities is computed in separate equilibrium MD simulations.

pair is polarized by external electric fields. Therefore, the effective dielectric constant

experienced by the ions can be smaller than that at equilibrium conditions, akin to the scenario

when bulk dielectric fluids (e.g., water) or electrolyte confined between two walls is subject to a

strong external electric field imposed abruptly.[118] This helps explain the faster rise of cell

potential during the initial stage of charging in MD simulations. Such effects may be

incorporated into the BSK model by introducing a frequency-dependent dielectric constant, but

this study is out of the scope of the present work. Figure 4.6b also shows that, at the later stage of charging (wall charge > 0.045 C/m^2), the cell potential predicted by the BSK model increases at a slower rate compared to that observed in MD simulations. This is caused in part by the fact that a constant ion diffusion coefficient was used in the BSK model. When the wall charge density increases beyond ~0.04 C/m^2, further growth of the ionic space charge layers is mainly due to the growth of the first ionic layer (MD results not shown). Since the counter-ion density inside the first ionic layer is already large at a wall charge density of 0.04 C/m^2, further insertion of counter-ions in this layer tends to reduce their diffusion coefficient in the direction normal to the electrode wall.[119] Such a decrease of ion diffusion coefficient effectively increases the electrical resistance in the electrochemical cell, and consequently the potential drop across the cell from the MD simulations increases faster than that predicted by the BSK model, in which the ion diffusion coefficient is assumed to be uniform in the entire system and for the complete charging process.

Unlike previous modified PNP models, the BSK model effectively accounts for additional ion-ion correlations by introducing an electrostatic correlation length l_c into the Poisson equation (see. Equation 4.3). To evaluate the importance the ion-ion correlations effects, we also solved the BSK model by setting $l_c = 0$. In this case, the BSK model is reduced to the modified PNP model in Ref. 64, which only entertains steric effects. As shown in Figure 4.6, such a modified PNP model performs considerably worse than the BSK model, and cannot even predict the charging kinetics at the lowest charging rate. This highlights the significance of parameterizing ion-ion correlations in the BSK model.
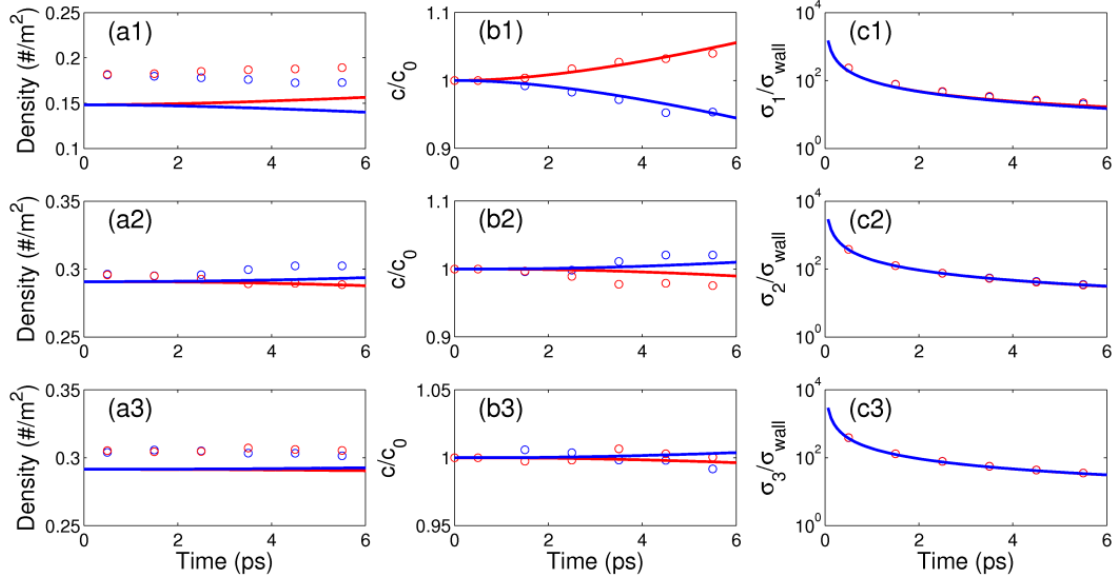
Figure 4.7. Temporal evolution of cation (red) and anion (blue) area densities in the first (a1, b1 and c1), second (a2, b2 and c2) and third (a3, b3 and c3) layers in the MD simulation at I = 25 kA/cm^2 (dotted) and BSK model (solid line). (a1-3) are unscaled ion densities, (b1-3) are ion densities scaled by their initial value at $t = 0$ and (c1-3) are ion charge densities scaled by charge density on the wall, which increases with time. The method for partition of layers is the same as that in Figure 4.3 of Ref. 12 and the width of each layer is 1 nm.

In addition to comparing the evolution of the electrical potential drop across the cell during charging, we performed a detailed comparison of the evolution of ion density profiles obtained by MD and the BSK model to further assess the accuracy of the BSK model in predicting the dynamics of double layer formation. To facilitate comparison, we divided the space between the right wall and middle plane into several layers following the partition method in Ref. 12. The width of each layer is 1 nm, and the first layer is the defined as the layer closest to the right wall.

We next calculated the evolution of average cation/anion area densities in the first, second and third layers using MD and BSK models, and the results are shown in Figure 4.7. We observe that the unscaled ion densities in these layers (Figure 4.7 (a1-3)) in the MD simulation

and BSK model differ even at $t = 0$, which makes the comparison of the evolution of unscaled ion densities at $t > 0$ difficult. The disagreement at $t = 0$ (when charge density on the wall is zero) is expected because ion densities are non-uniform in MD system but is uniform in the BSK model (see Figure 4.8).
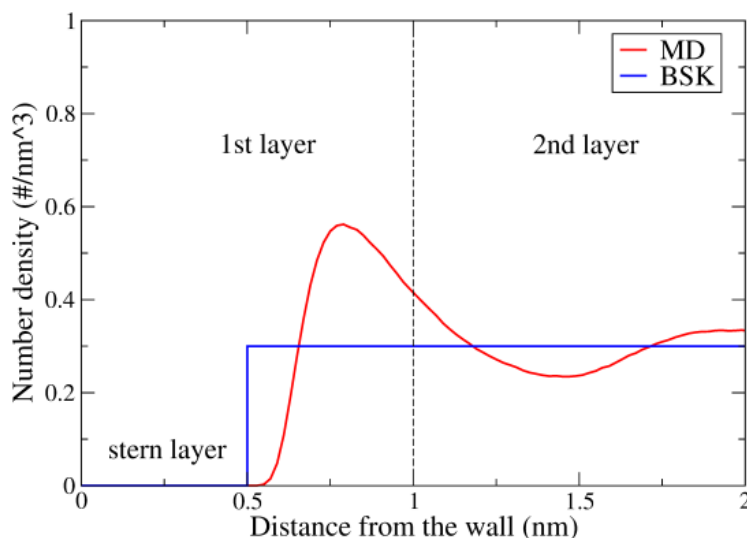
Figure 4.8. Ion densities near the wall when the wall is not charged in MD model and BSK model. Density profiles of cation and anion overlap with each other because the wall is electrically neutral.

To circumvent the above issue, we scaled the ion densities in each layer by their values at $t = 0$. Figure 4.7 (b1-3) show that in the first layer, the results from MD and BSK agree well with each other; in the second layer, ion densities predicted by MD model are slightly larger than that by BSK and their agreement is fair; in the third layer, the noise in MD results prevents a conclusive comparison. Alternatively, we also scaled the cation and anion area charge densities (σ_{cation} and σ_{anion}) in each layer by the charge density on the wall, which increases with time during constant current charging. Figures 4.7 (c1-3) show that, in all layers, the order of magnitude of $\sigma_{cation}/\sigma_{wall}$ and $\sigma_{anion}/\sigma_{wall}$ predicted by MD and BSK models agrees well. Such an agreement is not trivial because, at short time, the magnitude of wall charge density σ_{wall} is very

small. Note that the profiles of $\sigma_{cation}/\sigma_{wall}$ and $\sigma_{anion}/\sigma_{wall}$ nearly overlap with each other in all layers because the difference between cation and anion densities is quite small.

4.4 Conclusions

In summary, we have studied the dynamics of EDL formation at the interface of planar electrodes and RTILs under constant-current charging conditions. At relatively low charging rates, the evolution of the cell potential drop predicted by the MD simulations and the BSK model agree with each other quite well. At very high charging rates, MD simulations predict a very fast rise of the cell potential at very short times and an oscillation of the cell potential until the wall charge density reaches a moderate value (~0.02 C/m^2 in our model). Such oscillation is caused by the sequential growth of the space charge layers with net charges of alternating signs near the electrode wall, and cannot be predicted by the present BSK model. In addition, the BSK model predicts a slower rise of cell potential during both the initial and later stage of charging compared to that obtained from MD simulations. Such a difference is most likely caused by the fact that the BSK model is parameterized under equilibrium conditions. This can in principle be resolved by introducing frequency-dependent dielectric constant, ion density-dependent diffusion coefficients and even local concentration/field dependent l_c into the BSK model.[41,120] Together, these results suggest that, unless EDL formation occurs under far-from-equilibrium conditions, its macroscopic behavior can be predicted quite well by the BSK model. The evolution of ion density profiles, another aspect of the EDL formation dynamics, is also compared to further assess the accuracy of the BSK model in predicting the dynamics of double layer formation, showing good agreement between the MD and BSK model.

The present study suggests that one can gain insights into the formation of separate EDL layers, an atomistic process difficult to quantify directly, by analyzing the oscillation of the electrical potential as a function of time during a constant-current charging process. Such a procedure can also potentially provide critical information about the ion transport behavior within the EDL and in the direction normal to the electrode wall. However, the experimental studies of galvanostatic charge/discharge of supercapacitors utilizing RTILs as electrolytes do not display such potential oscillations, probably because of the limited temporal resolution on a time scale of seconds. In the model RTIL we employed, the potential oscillation is observed at very large charging current ($>O(100 \text{ kA/cm}^2)$) and very short time scale ($<O(5 \text{ ps})$). As pointed out above, this is mainly caused by the large diffusion coefficient of the model RTILs, which enables very fast formation/relaxation of the EDL structure and potential. Consequently, a far-from-equilibrium EDL formation can only be probed using large charging currents and observed at short time scales. For practical RTILs, whose diffusion coefficient is usually three to four orders of magnitude smaller than the model RTIL considered here, the formation/relaxation of EDL is much slower and thus we can expect the potential oscillation to be observed at charging currents that are more accessible experimentally and at much longer time scales up to 1 ns. Nevertheless, the temporal resolution of present galvanostatic charge/discharge experiments must be enhanced to the nanosecond scale in order to observe the potential oscillations predicted in this work.

CHAPTER 5

Conclusions

Room-temperature ionic liquids (RTILs) are an emerging class of electrolytes that holds promise of greatly improving the performance of many electrochemical devices. The transport behavior of RTILs in nanopores plays a crucial role in determining the performance of these devices. Most prior research on the transport behavior of RTILs focused on the equilibrium self-diffusion in nanopores, and relatively little is known about their non-equilibrium transport. In this dissertation, we use molecular dynamics (MD) and continuum simulations to investigate the non-equilibrium transport of RTILs in nanopores. We consider three qualitatively different scenarios: the hydrodynamic transport of RTILs, in which the electrical double layers (EDLs) are not perturbed; the ionic transport through nanopores connected with RTIL reservoirs, in which EDLs are perturbed along the pore length direction; the charging dynamics in electrochemical cells, in which the EDLs form in response to the imposed currents.

For the hydrodynamic transport of RTILs, we simulated the electroosmotic flows (EOFs) through slit nanochannels filled with RTILs. Our key findings are as follows:

1. The EOF velocity profile shows significant oscillations near charged walls. This is due to strong ion-ion correlations in RTILs, which lead to alternating layering of counter/co-ions near charged channel walls. The alternating layering of ions in turn leads to oscillations of space charge and EOF driving force, and finally an oscillation of the EOF velocity.

2. The strength of the EOF greatly exceeds that predicted by classical electrokinetic theory if correct ion distribution and electro-friction between ions and walls are taken

91

into account. We demonstrated that the amplified velocity is caused by the short-wavelength of the EOF. EOF velocity profile of RTILs features short-wavelength components due to its significant oscillations near charge walls. For such flows, the shear stress at one position no longer depends only on the local strain rate, but must be described by the nonlocal strain rate-shear stress constitutive law. The EOF in RTILs is thus a rare example in which short-wavelength hydrodynamics profoundly affects flow measurables in macroscopic systems and thus is a good test bed for developing improved theories for generalized hydrodynamics.

For ionic transport through nanopores connected with RTIL reservoirs, we computed the ionic current through neutral and charged nanopores with diameter comparable to the size of ions. We investigated how the ionic current and structure of the RTILs in nanopore evolve as the voltage changes. Our key findings are as follows:

1. Inside the neutral pore, as applied voltage increases, the ionic current increases nonlinearly but the ion density decreases. Inside the charged pore with the same diameter, similar trends are observed but the ionic current increases much shaper compared to that in neutral pores. At sufficiently high voltages, a significant portion of the charged nanopore becomes empty (termed dewetting here) while the ionic current is very high. The latter observation differs qualitatively from the transport of aqueous electrolytes through nanopores.

2. The sharp increase of the ionic current as voltage increases and the concomitant nanopore dewetting is caused by the sharp increase of ion mobility as the ion density in RTILs decreases, which is unique to solvent-free electrolytes confined in

nanopores with diameter compared to the ion size. Specifically, inside nanopores, the electrical field is stronger than that in bulk electrolyte and this leads to a decrease of ion density inside nanopore as the voltage is applied. This in turn leads to ion depletion inside the pore and the formation of ionic clouds near pore entrances. While the ion depletion tends to further increase ion mobility inside pore, the formation of ionic clouds near pore entrances reduces the electrical field inside pore. These two processes compete with each other until the system reaches steady state. The net result is that the ionic current is enhanced as pore becomes dewetted. The essential role of the unique ion mobility-ion density relation in RTILs in the nonlinear I-V curve and ion depletion in nanopore is also supported by our continuum simulations based on a minimal ionic transport model in which we implemented an ion density-dependent ion mobility similar to that in RTILs.

Finally, for charging dynamics of electrochemical cells filled with RTILs, we used MD simulations and BSK model to study dynamics of EDL formation under constant-current charging condition. We investigated the spatial and temporal evolutions of the ion densities and electrical potential across the cell during charging. The key findings are as follows:

1. The MD results show that, at the same surface charge density on the electrode, the total potential drop across the cell under larger charging current is higher than that under smaller charging current. This is consistent with RC circuit theory, in that the potential drop across the resistor increases if the current running through it increases.

2. The potential drop across the cell oscillates at the beginning stage of charging and the magnitude of oscillation increases as charging current increases. We show that the

potential oscillation is related to the sequential formation of EDLs near charged walls. The formation of the first layer that mainly consists of counter-ions will decrease the total potential drop across the cell, while the formation of second layer that mainly consists of co-ions will increase total potential drop. The formation of further layers will continue increase or decrease the potential, but their influence on the potential becomes smaller as the layers form further away from the wall. Together, these phenomena cause potential oscillation to decay as charging proceeds. The origin of sequential formation of EDLs is related to the dynamic over-screening when net charge in each layer grows during the charging process.

3. The BSK model can predict the overall charging dynamics and the underlying EDL structure evolution quite well under small charging currents. For large charging currents, such as I = 400 kA/cm^2, the BSK model cannot capture the potential oscillations at the beginning of charging. The BSK model also predicts a relatively slower rise of the potential in initial and later stage of charging. Such a difference is most likely caused by the fact that the BSK model is parameterized under equilibrium conditions. This can in principle be resolved by introducing frequency-dependent dielectric constant, ion density-dependent diffusion coefficients and even local concentration/field dependent l_c into the BSK model. These results suggest that, unless EDL formation occurs under far-from-equilibrium conditions, its macroscopic behavior can be predicted quite well by the BSK model.

In summary, we discovered that the non-equilibrium transport of RTILs in electrified nanosystems exhibit features not found in the transport of conventional electrolytes. These unique features arise, at the most fundamental level, from the strong ion-ion correlations in

RTILs. More systematic study of these phenomena will help develop better theories for the non-equilibrium transport of RTILs and help exploit their potential for application in electrochemical systems to the fullest extent.

REFERENCES

[1] Crabtree, George W., and Nathan S. Lewis. "Solar energy conversion." *Physics today* (2008): 309-321.

[2] Borowy, Bogdan S., and Ziyad M. Salameh. "Dynamic response of a stand-alone wind energy conversion system with battery energy storage to a wind gust." *Energy Conversion, IEEE Transactions* on 12, no. 1 (1997): 73-78.

[3] Muetze, Annette, and J. G. Vining. "Ocean wave energy conversion-a survey." *In Industry Applications Conference, 2006. 41st IAS Annual Meeting. Conference Record of the 2006 IEEE*, vol. 3, pp. 1410-1417. IEEE, 2006.

[4] Khaligh, Alireza, and Omer C. Onar. *Energy harvesting: solar, wind, and ocean energy conversion systems*. CRC Press Inc., 2010.

[5] Carrette, L., K. A. Friedrich, and U1 Stimming. "Fuel cells–fundamentals and applications." *Fuel cells* 1, no. 1 (2001): 5-39.

[6] Yoshio, Masaki, Ralph J. Brodd, and Akiya Kozawa. *Lithium-Ion Batteries*. Springer, 2009.

[7] Girishkumar, G., B. McCloskey, A. C. Luntz, S. Swanson, and W. Wilcke. "Lithium− air battery: promise and challenges." *The Journal of Physical Chemistry Letters* 1, no. 14 (2010): 2193-2203.

[8] Conway, B. E., V. Birss, and J. Wojtowicz. "The role and utilization of pseudocapacitance for energy storage by supercapacitors." *Journal of Power Sources* 66, no. 1 (1997): 1-14.

[9] Winter, Martin, and Ralph J. Brodd. "What are batteries, fuel cells, and supercapacitors?." *Chemical reviews* 104, no. 10 (2004): 4245-4270.

[10] Ren, Liqing, Weilin Qu, and Dongqing Li. "Interfacial electrokinetic effects on liquid flow in microchannels." *International Journal of Heat and Mass Transfer* 44, no. 16 (2001): 3125-3134.

[11] Lorenz, Christian D., Paul S. Crozier, Joshua A. Anderson, and Alex Travesset. "Molecular dynamics of ionic transport and electrokinetic effects in realistic silica channels." *The Journal of Physical Chemistry C* 112, no. 27 (2008): 10222-10232.

[12] Ohno, Hiroyuki, ed. *Electrochemical aspects of ionic liquids*. John Wiley & Sons, 2011.

[13] Freemantle, Michael. *An introduction to ionic liquids*. Royal Society of chemistry, 2010.

[14] http://www.odec.ca/projects/2010/hegdxa2/ultracapacitor-image.jpg

[15] http://images.sciencedaily.com/2005/04/050421211102.jpg

[16] http://www.basf.com/group/corporate/de/function/photodb:/print-image/jpeg/Photostore/Press ephotos%20WCMS/1332_erlenmayer__27_03d.jpg

[17] Serrano, Elena, Guillermo Rus, and Javier Garcia-Martinez. "Nanotechnology for sustainable energy." *Renewable and Sustainable Energy Reviews* 13, no. 9 (2009): 2373-2384.

[18] Lee, Hee Y., and John B. Goodenough. "Supercapacitor behavior with KCl electrolyte." *Journal of Solid State Chemistry* 144, no. 1 (1999): 220-223.

[19] Lu, Max. Modern theories of carbon based electrochemical capacitors in *Supercapacitors: Materials, Systems and Applications*. Edited by Francois Beguin, and Elzbieta Frackowiak. John Wiley & Sons, 2013.

[20] Feng, Guang, Rui Qiao, Jingsong Huang, Sheng Dai, Bobby G. Sumpter, and Vincent Meunier. "The importance of ion size and electrode curvature on electrical double layers in ionic liquids." *Physical Chemistry Chemical Physics* 13, no. 3 (2011): 1152-1161.

[21] Kornyshev, Alexei A. "Double-layer in ionic liquids: paradigm change?." *The Journal of Physical Chemistry B* 111, no. 20 (2007): 5545-5557.

[22] Baldelli, Steven. "Interfacial structure of room-temperature ionic liquids at the solid–liquid interface as probed by sum frequency generation spectroscopy." *The Journal of Physical Chemistry Letters* 4, no. 2 (2012): 244-252.

[23] Peñalber, Chariz Y., Gary A. Baker, and Steven Baldelli. "Sum Frequency Generation Spectroscopy of Imidazolium-Based Ionic Liquids with Cyano-Functionalized Anions at the Solid Salt–Liquid Interface." *The Journal of Physical Chemistry B* 117, no. 19 (2013): 5939-5949.

[24] Tamura, Kazuhisa, Shin-ichiro Miyaguchi, Kiyoshi Sakaue, Yasuo Nishihata, and Jun'ichiro Mizuki. "Direct observation of Au (111) electrode surface structure in bis (trifluoromethylsulfonyl) amide-based ionic liquids using surface X-ray scattering." *Electrochemistry Communications* 13, no. 5 (2011): 411-413.

[25] Yoshimoto, Soichiro, Ryo Taguchi, Ryuichi Tsuji, Hiroyuki Ueda, and Katsuhiko Nishiyama. "Dependence on the crystallographic orientation of Au for the potential window of the electrical double-layer region in imidazolium-based ionic liquids." *Electrochemistry Communications* 20 (2012): 26-28.

[26] Perkin, Susan. "Ionic liquids in confined geometries." *Physical Chemistry Chemical Physics* 14, no. 15 (2012): 5052-5062.

[27] Perkin, Susan, Lorna Crowhurst, Heiko Niedermeyer, Tom Welton, Alexander M. Smith, and Nitya Nand Gosvami. "Self-assembly in the electrical double layer of ionic liquids." *Chemical Communications* 47, no. 23 (2011): 6572-6574.

[28] Zhang, Xiao, Yun-Xin Zhong, Jia-Wei Yan, Yu-Zhuan Su, Meng Zhang, and Bing-Wei Mao. "Probing double layer structures of Au (111)–BMIPF6 ionic liquid interfaces from potential-dependent AFM force curves." *Chem. Commun.* 48, no. 4 (2011): 582-584.

[29] Fedorov, Maxim V., and Alexei A. Kornyshev. "Towards understanding the structure and capacitance of electrical double layer in ionic liquids." *Electrochimica Acta* 53, no. 23 (2008): 6835-6840.

[30] Jiang, Xikai, and Rui Qiao. "Electrokinetic transport in room-temperature ionic liquids: Amplification by short-wavelength hydrodynamics." *The Journal of Physical Chemistry C* 116, no. 1 (2011): 1133-1138.

[31] Wang, Shu, Zhen Cao, Shu Li, and TianYing Yan. "A molecular dynamics simulation of the structure of ionic liquid (BMIM+/PF 6−)/rutile (110) interface." *Science in China Series B: Chemistry* 52, no. 9 (2009): 1434-1437.

[32] Kislenko, Sergey A., Igor S. Samoylov, and Ravil H. Amirov. "Molecular dynamics simulation of the electrochemical interface between a graphite surface and the ionic liquid [BMIM][PF 6]." *Physical Chemistry Chemical Physics* 11, no. 27 (2009): 5584-5590.

[33] Feng, Guang, Jingsong Huang, Bobby G. Sumpter, Vincent Meunier, and Rui Qiao. "A "counter-charge layer in generalized solvents" framework for electrical double layers in neat and hybrid ionic liquid electrolytes." *Physical Chemistry Chemical Physics* 13, no. 32 (2011): 14723-14734.

[34] Feng, Guang, De-en Jiang, and Peter T. Cummings. "Curvature effect on the capacitance of electric double layers at ionic liquid/onion-like carbon interfaces." *Journal of Chemical Theory and Computation* 8, no. 3 (2012): 1058-1063.

[35] Shim, Youngseon, and Hyung J. Kim. "Dielectric Relaxation and Solvation Dynamics in a Room-Temperature Ionic Liquid: Temperature Dependence." *The Journal of Physical Chemistry B* 117, no. 39 (2013): 11743-11752.

[36] Hooper, Justin B., Oleg N. Starovoytov, Oleg Borodin, Dmitry Bedrov, and Grant D. Smith. "Molecular dynamics simulation studies of the influence of imidazolium structure on the properties of imidazolium/azide ionic liquids." *The Journal of chemical physics* 136, no. 19 (2012): 194506.

[37] Bazant, Martin Z., Brian D. Storey, and Alexei A. Kornyshev. "Double layer in ionic liquids: Overscreening versus crowding." *Physical Review Letters* 106, no. 4 (2011): 046102.

[38] Fedorov, Maxim V., and Alexei A. Kornyshev. "Towards understanding the structure and capacitance of electrical double layer in ionic liquids." *Electrochimica Acta* 53, no. 23 (2008): 6835-6840.

[39] Bazant, Martin Z., Brian D. Storey, and Alexei A. Kornyshev. "Erratum: Double layer in ionic liquids: Overscreening versus crowding." *Physical Review Letters* 109, no. 14 (2012): 149903.

[40] Lyklema, Johannes. *Fundamentals of interface and colloid science: soft colloids*. Vol. 5. Academic press, 2005.

[41] Bazant, Martin Z., Mustafa Sabri Kilic, Brian D. Storey, and Armand Ajdari. "Towards an understanding of induced-charge electrokinetics at large applied voltages in concentrated solutions." *Advances in colloid and interface science* 152, no. 1 (2009): 48-88.

[42] Erickson, David, and Dongqing Li. "Three-dimensional structure of electroosmotic flow over heterogeneous surfaces." *The Journal of Physical Chemistry B* 107, no. 44 (2003): 12212-12220.

[43] Yuan, Zhen, Anthony L. Garcia, Gabriel P. Lopez, and Dimiter N. Petsev. "Electrokinetic transport and separations in fluidic nanochannels." *Electrophoresis* 28, no. 4 (2007): 595-610.

[44] Freund, Jonathan B. "Electro-osmosis in a nanometer-scale channel studied by atomistic simulation." *The Journal of Chemical Physics* 116, no. 5 (2002): 2194-2200.

[45] Wu, Peng, and Rui Qiao. "Physical origins of apparently enhanced viscosity of interfacial fluids in electrokinetic transport." *Physics of Fluids (1994-present)* 23, no. 7 (2011): 072005.

[46] Qiao, R., and N. R. Aluru. "Charge inversion and flow reversal in a nanochannel electro-osmotic flow." *Physical review letters* 92, no. 19 (2004): 198301.

[47] Qiao, R., *Continuum and atomistic simulation of electrically-mediated flow through nanometer channels*, 2004, University of Illinois at Urbana-Champaign

[48] http://www.upenn.edu/pennnews/sites/default/files/news/images/JR.jpg

[49] Siwy, Zuzanna S. "Ion-Current Rectification in Nanopores and Nanotubes with Broken Symmetry." *Advanced Functional Materials* 16, no. 6 (2006): 735-746.

[50] Cruz-Chu, Eduardo R., Aleksei Aksimentiev, and Klaus Schulten. "Ionic current rectification through silica nanopores." *The Journal of Physical Chemistry C* 113, no. 5 (2009): 1850-1862.

[51] Kovarik, Michelle L., Kaimeng Zhou, and Stephen C. Jacobson. "Effect of conical nanopore diameter on ion current rectification." *The Journal of Physical Chemistry B* 113, no. 49 (2009): 15960-15966.

[52] Cervera, J., B. Schiedt, and P. Ramirez. "A Poisson/Nernst-Planck model for ionic transport through synthetic conical nanopores." *EPL (Europhysics Letters)* 71, no. 1 (2005): 35.

[53] Dzubiella, J., and J-P. Hansen. "Electric-field-controlled water and ion permeation of a hydrophobic nanopore." *The Journal of chemical physics* 122, no. 23 (2005): 234706.

[54] Dzubiella, J., R. J. Allen, and J-P. Hansen. "Electric field-controlled water permeation coupled to ion transport through a nanopore." *The Journal of chemical physics* 120, no. 11 (2004): 5001-5004.

[55] Singh, Ramesh, Joshua Monk, and Francisco R. Hung. "A computational study of the behavior of the ionic liquid [BMIM+][PF6−] confined inside multiwalled carbon nanotubes." *The Journal of Physical Chemistry C* 114, no. 36 (2010): 15478-15485.

[56] Rajput, Nav Nidhi, Joshua Monk, and Francisco R. Hung. "Structure and dynamics of an ionic liquid confined inside a charged slit graphitic nanopore." *The Journal of Physical Chemistry C* 116, no. 27 (2012): 14504-14513.

[57] Iacob, C., J. R. Sangoro, W. K. Kipnusu, R. Valiullin, J. Kärger, and F. Kremer. "Enhanced charge transport in nano-confined ionic liquids." *Soft Matter* 8, no. 2 (2012): 289-293.

[58] Rajput, Nav Nidhi, Joshua Monk, Ramesh Singh, and Francisco R. Hung. "On the influence of pore size and pore loading on structural and dynamical heterogeneities of an ionic liquid confined in a slit nanopore." *The Journal of Physical Chemistry C* 116, no. 8 (2012): 5169-5181.

[59] Singh, Ramesh, Joshua Monk, and Francisco R. Hung. "Heterogeneity in the Dynamics of the Ionic Liquid [BMIM+][PF6–] Confined in a Slit Nanopore." *The Journal of Physical Chemistry C* 115, no. 33 (2011): 16544-16554.

[60] Davenport, Matthew, Andrew Rodriguez, Kenneth J. Shea, and Zuzanna S. Siwy. "Squeezing ionic liquids through nanopores." *Nano letters* 9, no. 5 (2009): 2125-2128.

[61] Lanning, Oliver J., and Paul A. Madden. "Screening at a charged surface by a molten salt." *The Journal of Physical Chemistry B* 108, no. 30 (2004): 11069-11072.

[62] Pinilla, Carlos, M. G. Del Pópolo, Jorge Kohanoff, and R. M. Lynden-Bell. "Polarization relaxation in an ionic liquid confined between electrified walls." *The Journal of Physical Chemistry B* 111, no. 18 (2007): 4877-4884.

[63] Vatamanu, Jenel, Oleg Borodin, and Grant D. Smith. "Molecular simulations of the electric double layer structure, differential capacitance, and charging kinetics for N-methyl-N-propylpyrrolidinium bis (fluorosulfonyl) imide at graphite electrodes." *The Journal of Physical Chemistry B* 115, no. 12 (2011): 3073-3084.

[64] Kilic, Mustafa Sabri, Martin Z. Bazant, and Armand Ajdari. "Steric effects in the dynamics of electrolytes at large applied voltages. II. Modified Poisson-Nernst-Planck equations." *Physical Review E* 75, no. 2 (2007): 021503.

[65] Zhao, Hui. "Diffuse-charge dynamics of ionic liquids in electrochemical systems." *Physical Review E* 84, no. 5 (2011): 051504.

[66] Bazant, Martin Z., Katsuyo Thornton, and Armand Ajdari. "Diffuse-charge dynamics in electrochemical systems." *Physical review E* 70, no. 2 (2004): 021506.

[67] Fedorov, Maxim V., Nikolaj Georgi, and Alexei A. Kornyshev. "Double layer in ionic liquids: The nature of the camel shape of capacitance." *Electrochemistry Communications* 12, no. 2 (2010): 296-299.

[68] Joly, Laurent, Christophe Ybert, Emmanuel Trizac, and Lydéric Bocquet. "Liquid friction on charged surfaces: From hydrodynamic slippage to electrokinetics." *The Journal of chemical physics* 125, no. 20 (2006): 204716.

[69] Wu, Peng, and Rui Qiao. "Physical origins of apparently enhanced viscosity of interfacial fluids in electrokinetic transport." *Physics of Fluids (1994-present)* 23, no. 7 (2011): 072005.

[70] Humphrey, W., Dalke, A. and Schulten, K., "VMD - Visual Molecular Dynamics", *J. Molec. Graphics*, 1996, vol. 14, pp. 33-38.

[71] Pronk, Sander, Szilárd Páll, Roland Schulz, Per Larsson, Pär Bjelkmar, Rossen Apostolov, Michael R. Shirts et al. "GROMACS 4.5: a high-throughput and highly parallel open source molecular simulation toolkit." *Bioinformatics* (2013): btt055.

[72] Yeh, In-Chul, and Max L. Berkowitz. "Ewald summation for systems with slab geometry." *The Journal of Chemical Physics* 111, no. 7 (1999): 3155-3162.

[73] Bird, R. Byron, Warren E. Stewart, and Edwin N. Lightfoot. *Transport phenomena*. John Wiley & Sons, 2007.

[74] Chen, Yunfei, Zhonghua Ni, Guiming Wang, Dongyan Xu, and Deyu Li. "Electroosmotic flow in nanotubes with high surface charge densities." *Nano letters* 8, no. 1 (2008): 42-48.

[75] Freund, Jonathan B. "Electro-osmosis in a nanometer-scale channel studied by atomistic simulation." *The Journal of Chemical Physics* 116, no. 5 (2002): 2194-2200.

[76] Netz, R. R. "Electrofriction and dynamic stern layers at planar charged surfaces." *Physical review letters* 91, no. 13 (2003): 138101.

[77] Qiao, R., and N. R. Aluru. "Ion concentrations and velocity profiles in nanochannel electroosmotic flows." *The Journal of chemical physics* 118, no. 10 (2003): 4692-4701.

[78] This is also supported by the fact that, by using the position of the shear plane (or no-slip plane, which is typically thought to be located within 1 nm from the charged surface) as a

fitting parameter, the classical electrokinetic theory can explain a majority of the published experimental data unless the surface charge is dynamically modulated.[40]

[79] Gosling, Eveline M., I. R. McDonald, and K. Singer. "On the calculation by molecular dynamics of the shear viscosity of a simple fluid." *Molecular Physics* 26, no. 6 (1973): 1475-1484.

[80] Hess, Berk. "Determining the shear viscosity of model liquids from molecular dynamics simulations." *The Journal of chemical physics* 116, no. 1 (2002): 209-217.

[81] Boon, Jean Pierre, and Sidney Yip, *Molecular Hydrodynamics*, Courier Dover Publications, 1991.

[82] Ailawadi, Narinder K., Aneesur Rahman, and Robert Zwanzig. "Generalized hydrodynamics and analysis of current correlation functions." *Physical Review A* 4, no. 4 (1971): 1616.

[83] Evans, Denis J. "Equilibrium fluctuation expressions for the wave-vector-and frequency-dependent shear viscosity." *Physical Review A* 23, no. 5 (1981): 2622.

[84] Alley, W. Edward, and Berni J. Alder. "Generalized transport coefficients for hard spheres." *Physical Review A* 27, no. 6 (1983): 3158.

[85] Yan, Tianying, Christian J. Burnham, Mario G. Del Pópolo, and Gregory A. Voth. "Molecular dynamics simulation of ionic liquids: The effect of electronic polarizability." *The Journal of Physical Chemistry B* 108, no. 32 (2004): 11877-11881.

[86] Hansen, J. S., Peter J. Daivis, Karl P. Travis, and B. D. Todd. "Parameterization of the nonlocal viscosity kernel for an atomic fluid." *Physical Review E* 76, no. 4 (2007): 041121.

[87] Todd, B. D., and J. S. Hansen. "Nonlocal viscous transport and the effect on fluid stress." *Physical Review E* 78, no. 5 (2008): 051202.

[88] Cadusch, Peter J., B. D. Todd, Junfang Zhang, and Peter J. Daivis. "A non-local hydrodynamic model for the shear viscosity of confined fluids: analysis of a homogeneous kernel." *Journal of Physics A: Mathematical and Theoretical* 41, no. 3 (2008): 035501.

[89] Todd, B. D., J. S. Hansen, and Peter J. Daivis. "Nonlocal shear stress for homogeneous fluids." *Physical review letters* 100, no. 19 (2008): 195901.

[90] Roy, Durba, and Mark Maroncelli. "An improved four-site ionic liquid model." *The Journal of Physical Chemistry B* 114, no. 39 (2010): 12629-12631.

[91] Karniadakis, George, Ali Beskok, and Narayan Aluru. *Microflows and nanoflows: fundamentals and simulation*. Vol. 29. Springer, 2006.

[92] Travis, Karl P., B. D. Todd, and Denis J. Evans. "Departure from Navier-Stokes hydrodynamics in confined liquids." *Physical Review E* 55, no. 4 (1997): 4288.

[93] This empirical observation may be explained by a recent finding,[87] which shows that, at least for homogeneous liquids, the classical hydrodynamics is sufficient if the strain rate varies little over the width of the viscosity kernel (typically 2-3 molecular diameters[86]). Since the most widely studied nanoflows are Couette and Poiseuille flows in which the strain rate is zero or constant, it follows that the classical hydrodynamic theory is exact regardless of the width of the viscosity kernel.

[94] Mezger, Markus, Sebastian Schramm, Heiko Schröder, Harald Reichert, Moshe Deutsch, Emerson J. De Souza, John S. Okasinski, Benjamin M. Ocko, Veijo Honkimäki, and Helmut Dosch. "Layering of [BMIM]+-based ionic liquids at a charged sapphire interface." *The Journal of chemical physics* 131, no. 9 (2009): 094701.

[95] Vatamanu, Jenel, Oleg Borodin, and Grant D. Smith. "Molecular insights into the potential and temperature dependences of the differential capacitance of a room-temperature ionic liquid at graphite electrodes." *Journal of the American Chemical Society* 132, no. 42 (2010): 14825-14833.

[96] Alexiadis, Alessio, and Stavros Kassinos. "Molecular simulation of water in carbon nanotubes." *Chemical Reviews* 108, no. 12 (2008): 5014-5034.

[97] Hess, Berk, Henk Bekker, Herman JC Berendsen, and Johannes GEM Fraaije. "LINCS: a linear constraint solver for molecular simulations." *Journal of computational chemistry* 18, no. 12 (1997): 1463-1472.

[98] Karnik, Rohit, Rong Fan, Min Yue, Deyu Li, Peidong Yang, and Arun Majumdar. "Electrostatic control of ions and molecules in nanofluidic transistors." *Nano letters* 5, no. 5 (2005): 943-948.

[99] Aksimentiev, Aleksij, and Klaus Schulten. "Imaging< i> α</i>-Hemolysin with Molecular Dynamics: Ionic Conductance, Osmotic Permeability, and the Electrostatic Potential Map." *Biophysical journal* 88, no. 6 (2005): 3745-3761.

[100] Roux, Benoît. "The membrane potential and its representation by a constant electric field in computer simulations." *Biophysical journal* 95, no. 9 (2008): 4205-4216.

[101] Merlet, Céline, Benjamin Rotenberg, Paul A. Madden, Pierre-Louis Taberna, Patrice Simon, Yury Gogotsi, and Mathieu Salanne. "On the molecular origin of supercapacitance in nanoporous carbon electrodes." *Nature materials* 11, no. 4 (2012): 306-310.

[102] Shim, Youngseon, and Hyung J. Kim. "Nanoporous carbon supercapacitors in an ionic liquid: a computer simulation study." *ACS nano* 4, no. 4 (2010): 2345-2355.

[103] Merlet, Céline, Clarisse Péan, Benjamin Rotenberg, Paul A. Madden, Patrice Simon, and Mathieu Salanne. "Simulating supercapacitors: can we model electrodes as constant charge surfaces?." *The Journal of Physical Chemistry Letters* 4, no. 2 (2012): 264-268.

[104] Raghunathan, A. V., and N. R. Aluru. "Self-consistent molecular dynamics formulation for electric-field-mediated electrolyte transport through nanochannels." *Physical Review E* 76, no. 1 (2007): 011202.

[105] Daiguji, Hirofumi. "Ion transport in nanofluidic channels." *Chemical Society Reviews* 39, no. 3 (2010): 901-911.

[106] Daily, John W., and Michael M. Micci. "Ionic velocities in an ionic liquid under high electric fields using all-atom and coarse-grained force field molecular dynamics." *The Journal of chemical physics* 131, no. 9 (2009): 094501.

[107] Qiao, R., and N. R. Aluru. "Atypical dependence of electroosmotic transport on surface charge in a single-wall carbon nanotube." *Nano letters* 3, no. 8 (2003): 1013-1017.

[108] Qiao, R., and N. R. Aluru. "Surface-charge-induced asymmetric electrokinetic transport in confined silicon nanochannels." *Applied Physics Letters* 86, no. 14 (2005): 143105.

[109] Karnik, Rohit, Chuanhua Duan, Kenneth Castelino, Hirofumi Daiguji, and Arun Majumdar. "Rectification of ionic current in a nanofluidic diode." *Nano letters* 7, no. 3 (2007): 547-551.

[110] Keskin, Seda, Defne Kayrak-Talay, Uğur Akman, and Öner Hortaçsu. "A review of ionic liquids towards supercritical fluid applications." *The Journal of Supercritical Fluids* 43, no. 1 (2007): 150-180.

[111] Largeot, Celine, Cristelle Portet, John Chmiola, Pierre-Louis Taberna, Yury Gogotsi, and Patrice Simon. "Relation between the ion size and pore size for an electric double-layer capacitor." *Journal of the American Chemical Society* 130, no. 9 (2008): 2730-2731.

[112] Pushparaj, Victor L., Manikoth M. Shaijumon, Ashavani Kumar, Saravanababu Murugesan, Lijie Ci, Robert Vajtai, Robert J. Linhardt, Omkaram Nalamasu, and Pulickel M. Ajayan. "Flexible energy storage devices based on nanocomposite paper." *Proceedings of the National Academy of Sciences* 104, no. 34 (2007): 13574-13577.

[113] Feng, G., J. S. Zhang, and R. Qiao. "Microstructure and capacitance of the electrical double layers at the interface of ionic liquids and planar electrodes." *The Journal of Physical Chemistry C* 113, no. 11 (2009): 4549-4559.

[114] *Comsol Multiphysics 4.2 User Guide*, Burlington, United States, 2011

[115] *Comsol Multiphysics 4.2 Reference Guide*, Burlington, United States, 2011

[116] Frackowiak, Elzbieta. "Carbon materials for supercapacitor application." *Physical Chemistry Chemical Physics* 9, no. 15 (2007): 1774-1785.

[117] Izgorodina, Ekaterina I., Maria Forsyth, and Douglas R. MacFarlane. "On the components of the dielectric constants of ionic liquids: ionic polarization?." *Physical chemistry chemical physics* 11, no. 14 (2009): 2452-2458.

[118] Cagle, Clint, Guang Feng, Rui Qiao, Jingsong Huang, Bobby G. Sumpter, and Vincent Meunier. "Structure and charging kinetics of electrical double layers at large electrode voltages." *Microfluidics and Nanofluidics* 8, no. 5 (2010): 703-708.

[119] Sendner, Christian, Dominik Horinek, Lyderic Bocquet, and Roland R. Netz. "Interfacial water at hydrophobic and hydrophilic surfaces: Slip, viscosity, and diffusion." *Langmuir* 25, no. 18 (2009): 10768-10781.

[120] Bazant, Martin Z. "Theory of chemical kinetics and charge transfer based on nonequilibrium thermodynamics." *Accounts of chemical research* 46, no. 5 (2013): 1144-1160.